工學博士學位論文

High-Performance Planar Perovskite Solar Cells *via* Process and Structure Simplification

공정 및 구조 단순화를 통한 고성능의 평면형 페로브스카이트 태양전지 제조

2019年 8月

서울大學校 大學院

化學生物工學部

柳 亥 俊

High-Performance Planar Perovskite Solar Cells *via* Process and Structure Simplification

공정 및 구조 단순화를 통한 고성능의 평면형 페로브스카이트 태양전지 제조

指導敎授 張 正 植

이 論文을 工學博士 學位論文으로 提出함

2019 年 5 月

서울大學校 大學院
化學生物工學部
柳 亥 俊

柳亥俊의 工學博士 學位論文을 認准함

2019 年 5 月

委 員 長 趙 在 英 (印)

副委員長 張 正 植 (印)

委 員 金 榮 奎 (印)

委 員 李 鍾 贊 (印)

委 員 林 淳 皓 (印)

High-Performance Planar Perovskite Solar Cells *via* Process and Structure Simplification

by

Haejun Yu

Submitted to the Graduate School of Seoul National University in Partial Fulfillment of the Requirements for the Degree of Doctor of Philosophy

August, 2019

Thesis Adviser: Jyongsik Jang

Abstract

Perovskite solar cells (PSCs) is of tremendous interest in a photovoltaic field due to the extraordinary photophysical properties of the organic-inorgainc hybrid perovskite. Currently, to accomplish their commercialization, a trend of research is shifting to practical issues related to actual operation of the PSCs in daily life, such as modularisation, encapsulation for long-term stability, and toxicity test. However, there are relatively few studies related to improving process and structure that directly affect unit price, mass production, and reproducibility. Therefore, there is a great need to discover strategies that can simplify the structure and process without sacrificing device performance.

Planar PSCs have included an n-type metal oxide-based hole-blocking layer (HBL) as an essential component, and their optical and electrical qualities vary greatly depending on the oxidation methods. Conventionally, high-temperature of 500 °C and long annealing time of *ca.* 1 - 3 h are required to prepare the HBL, which is skeptical for unit-cost and mass production. Therefore, there is a demand for devising an economical annealing process that can substitute this time- and energy-consuming TA. In addition to the plan of process replacement,

eliminating the HBL is a persuasive way for the LT and fast fabrication processes. This approach is a good strategy to improve productivity and to reduce unit-cost, because both all preparatory steps for manufacturing the HBL and the required energy for oxidation can be omitted. However, due to the lack of HBL, electron transport rate decreases and the chance of contact between hole transport material (HTM) and transparent conductive oxide (TCO) rises, resulting in unfavourable performance and severe hysteresis in the PSCs.

This dissertation describes the effective strategies to mitigate significantly laborious tasks in fabricating the planar PSCs through simplifying the process and structure. Detailedly, the TA conventionally used for the preparation of HBL is replaced with atmospheric Ar/O_2 plasma-annealing (PA), or the HBL is absolutely removed from the structure of planar PSC. Firstly, the SnO_2 thin film (TF) is formulated at superfast rate, within 5 min, under an almost room-temperature condition (< 50 ºC), using atmospheric Ar/O_2 PA and applied it as the HBL of PSCs. The plasma-annealed SnO_2 HBL has not only more even surface but also outstanding electrical conductivity with higher electron mobility (μ) and a lower number of defect sites, consequently improving the performance of PSCs. Secondly, the HBL of PSC is entirely excluded to further

simplify the fabrication process and structure, and the perovskite grain size and thickness are modulated to maximize the performance of HBL-free PSCs. In this structure, perovskite serves as the HBL for blocking the penetration of the HTM, and it is observed that the hole blocking ability and performance are improved as the perovskite grain size and film thickness increased. Thirdly, the hierarchically porous fluorine-doped tin oxide (FTO) substrate is prepared through an electrochemical etching process on the surface of commercial FTO, which is used as TCO of the HBL-free PSC. This surface modification not only fosters charge extraction rate at the FTO/perovskite interface but also facilitates a substantial increase in the photocurrent density and mitigation of the hysteretic behavior. In addition, the HBL-free PSCs exhibits excellent photostability because it is free from the HBL-induced perovskite degradation. Accordingly, this study provides several strategies about the process and structural simplification of the HBL-free PSCs to not only improve convenience in fabrication, productivity, and economical issue, but also achieve high efficiency and stability.

Keywords: Perovskite solar cell, Process and structure simplification, Atmospheric Ar/O_2 plasma oxidation, Large grain of perovskite,

Porous transparent electrode.

Student Number: 2014-22595

List of Abbreviations

A: active area

AFM: atomic force microscopy

Al_2O_3: aluminium oxide

Au: gold

CBM: conduction band minimum

CL: compact layer

CsI: cesium iodide

d: thickness

DI: deionized

DMF: *N,N*-dimethylformamide

DMSO: dimethyl sulfoxide

DSSC: dye-sensitized solar cells

ECEP: electrochemical etching process

ECP: electrochemical process

EDS: energy dispersive spectroscopy

E-FTO: etched FTO

E_g: band gap

EIS: electrochemical impedance spectroscopy

EQE: external quantum efficiency

ETL: electron transport layer

FAI: formamidinium iodide

FE-SEM: field emission-scanning electron microscopy

FF: fill factor

FS-TA: femtosecond transient absorption

FTO: fluorine-doped tin oxide

GB: grain boundary

h: hour

HBL: hole-blocking layer

HBL-free PSC: hole-blocking layer-free perovskite solar cell

HCl: hydrochloric acid

HOMO: highest occupied molecular orbital

HT: high-temperature

HTL: hole-transport layer

HTM: hole-transport material

IPCE: incident photon-to-current efficiency

ITO: indium tin oxide

I–V: current–voltage

J_{SC}: short-circuit current density

J–V: current density–voltage

Li-TFSI: lithium bis(trifluoromethylsulphonyl)imide

LT: low-temperature

LUMO: lowest unoccupied molecular orbital

MABr: methylammonium bromide

MAI: methylammonium iodide

$MAPbI_3$: methylammonium lead iodide ($CH_3NH_3PbI_3$)

$MAPbI_{3-x}Cl_x$: chlorine-doped methylammonium lead iodide.

min: minute

mL: milliliter

M-O-M: metal-oxygen-metal

MP: maximized performance

MPL: mesoporous layer

MPPA: millisecond-pulsed photonic annealing

MS-PSC: mesoscopic perovskite solar cell

nm: nanometer

ns: nanosecond

N_t: electron trap density

OCVD: open-circuit voltage decay

PA: plasma-annealing

$PbBr_2$: lead (II) bromide

PbI_2: lead (II) iodide

PCE: power conversion efficiency

P-FTO: pristine FTO

PMMA: poly(methyl methacrylate)

P-PSC: plasma-annealed SnO_2-based perovskite solar cell

ps: picosecond

PSC: perovskite solar cell

P-SnO_2: plasma-annealed-SnO_2

PTFE: polytetrafluoroethylene

PV: photovoltaic

R_{ct}: charge transfer resistance

R_{rec}: charge recombination resistance

RF: roughness factor

RH: relative humidity

RMS: root-mean-square

s: second

SCLC: space-charge-limited current

SE: solvent-engineering

$SnCl_2$: tin (II) chloride

SnO_2: tin oxide

SnO_2:F: fluorine-doped SnO_2

spiro-OMeTAD: 2,2′,7,7′-tetrakis(N,N-di-p-methoxyphenylamine)-9,9′-spirobifluorene

SPO: stabilized power output

SSPL: steady-state photoluminescence

TA: thermal-annealing

TCO: transparent conductive oxide

TD: thermal-decomposition

TF: thin film

TiO_2: titanium dioxide

T-PSC: thermally-annealed SnO_2-based perovskite solar cell

TRPL: time-resolved photoluminescence

T-SnO_2: thermally-annealed-SnO_2 (T-SnO2)

TTIP: titanium isopropoxide

UPS: ultraviolet photoelectron spectroscopy

UV/O_3: ultraviolet/ozone

UV-VIS: ultraviolet–visible

V_{OC}: open-circuit voltage

V_{TFL}: trap-filled limit voltage

W: photoluminescence decay weight faction

WF: work function

XRD: x-ray diffraction

XPS: x-ray photoelectron spectroscopy

ZnO: zinc oxide

$Zn(O_2CCH_3)_2$: zinc acetate

4-*t*BP: 4-*tert*-butyl pyridine

μm: micrometer

ε: relative dielectric constant

ε_0: free space permittivity

η: efficiency

θ: theta

μ: electron mobility

σ_0: direct current conductivity

τ: photoluminescence decay time constant

List of Figures

with organic-inorganic halide perovskites. The HBL accepts photo-excited electrons stayed in perovskite, and blocks the contact between TCO and HTM.

Figure 11. (a) UV-induced degradation mechanism of TiO_2; the deeply trapped electrons are recombined with the holes on the HTM. (b) Degradation patterns of TiO_2 HBL-based PSC as a function of light exposure time under ambient conditions. (c) X-ray diffraction (XRD) patterns and photographs of perovskite film coated on the ZnO-based HBL.

Figure 12. Evolution of efficiency in the SnO_2 HBL-based PSCs, and its ordinary device structure.

Figure 13. An evolution of the PSC structure; (a) Regular mesoscopic type can be simplified to (b) regular or (c) inverted planar types. The planar structures can be further simplified to (d) HBL-free, (e) regular HTL-free and (f) inverted HTL-free types.

Figure 14. (a) Schematic structure of the HBL-free PSC and (b) its energy band diagram. (c) *J-V* curves of PSCs: ZnO HBL and P3HT HTL (black line), no HBL and P3HT HTL (blue line), and no HBL and spiro-OMeTAD (red line). (d) Stability test

distinguished by a rectangular red-line. At the right of this, the real image showing the extent of gas flow and unintentional plate heating by plasma were displayed.

Figure 25. Surface FE-SEM images of the of SnO_2 TFs activated by thermal and plasma energy.

Figure 26. XRD patterns of FTO glass/T- and P-SnO_2 TFs. The result reveals the amorphous phase of SnO_2.

Figure 27. EDS results of (a) T-SnO_2 and (b) P-SnO_2 TFs formed on the bare glass. (c) Summarizing the element composition in each SnO_2 TF by atomic percentage.

Figure 28. Transmittance spectra of FTO glass and two types of SnO_2 TFs deposited on FTO glass, and the E_g, computed by Tauc-plot (inset graph). The Tauc-plot was drawn by combining the reflectance and transmittance spectra of T-and P-SnO_2 TFs coated on quartz glass. The E_g of 4.02 eV was determined by extrapolating the linear portion of the plot.

Figure 29. UV-Vis (a) reflectance and (b) transmittance spectra of T- and P-SnO_2 TFs coated on quartz glass. Tauc-plot of (c) T- and (d) P-SnO_2 TF extracted from the glass based-reflectance and transmittance spectra.

Figure 30. Two-dimensional AFM images of the SnO_2 TFs on FTO glass prepared by (a) the TA at 180 ºC for 60 min and (b) PA with Ar/ O_2 flow of 0.008/0.06 L/h for 5 min. The roughness was analyzed by line profile measurement at three different regions.

Figure 31. (a) XPS survey spectra of SnO_2 TFs activated by thermal and plasma routes. (b) Sn 3d peaks of two SnO_2 TFs and O_2 1s peaks for (c) T-SnO_2 and (d) P-SnO_2 TFs.

Figure 32. (a) Tafel plot and corresponding *J–V* curves (inset) of the FTO/T-SnO_2 or P-SnO_2/Au devices measured under dark conditions to analyze the vertical conductivity (b). $J^{1/2}$–*V* curves, plotted *via* the Mott–Gurney law, to calculate the SCLC electron mobility (μ) based on the structure of FTO/T- of P-SnO_2/Au devices.

Figure 33. Dark *J-V* curves of FTO/(a) T- and (b) P-SnO_2/Au dummy cells for exploring the V_{TFL} kink point.

Figure 34. (a) Schematic diagram of the device architecture including the SnO_2 TF as an HBL and band energy diagram showing the behavior of photo-excited electrons at the interface between perovskite and the two types of SnO_2 TFs. The band

on film thickness. The grain size of solvent-annealed film prepared by 37 wt% precursor has similar with that of the normally annealed film prepared by 51 wt% precursor.

Figure 62. (a) Nyquist plots of the HBL-free PSCs as a function of precursor concentration under dark condition at 0.7 V bias. (b) An illustration depicting the penetration of the HTM into a perovskite film through a crevice. (Left) The penetration of HTM can be disturbed by large grains densely located along an orthogonal path in a high-thickness film. (Right) On the other hand, the HTM can easily reach the FTO surface through many penetration pathways (GBs).

Figure 63. *J-V* characteristics obtained from (a) the HBL free and (b) TiO_2 HBL-inserted PSCs according to annealing method. All PSCs were fabricated with the precursor of 51 wt%. After the DMSO annealing, the PCE of HBL-free PSCs increased by 21 %, while the PCE of TiO_2 HBL inserted-PSCs increased by 7 %.

Figure 64. (a) TRPL decay curves for $MAPbI_3$ TFs deposited using various precursor solution concentrations. The sample for time-resolved PL consists of FTO/$MAPbI_3$/spiro-OMeTAD

the P-FTO-based PSC case. The incident light was highly scattered mostly adjacent to the etched parts of E-FTO; additional light absorption by the perovskite would be possible in these regions.

Figure 75. UV-Vis incident light absorption spectra by the adsorbed dyes on P- and E-FTO. 0.25 mM dye solution was used to adsorb dye on the substrate. The desorption process was carried out using 0.01 M NaOH solution.

Figure 76. Cross-sectional FE-SEM image of the E-FTO-based PSC. The ECEP produced a mesoporous SnO_2 layer composed of SnO_2 nanoparticles at the top of the FTO. The perovskite penetrated into every feature of the mesoporous SnO_2 region.

Figure 77. (a) Cross-sectional FE-SEM images of the E-FTO-based PSC. (b) Illustration of the extraction behavior of photo-excited electrons from perovskite into the FTO. The charges quickly accumulated at the interface between the E-FTO and perovskite due to the larger charge contact area of the E-FTO compared with the P-FTO.

Figure 78. (a) *J–V* characteristics and (b) IPCE spectra of E-FTO- and P-FTO-based PSCs.

Figure 90. (a) Long-term stability in ambient air (25°C, 30 % RH). (b) Recyclablity testing of the E-FTO-based PSC. No samples were encapsulated, and the performance was measured without a UV-blocking filter. Photostability test results obtained from P- and E-FTO based PSCs, which was measured under constant AM 1.5G illumination and 35 % RH for 270 min.

Figure 91. Recyclability of E-FTO-based HBL-free PSCs. The initial cell was re-used through rinsing the cell using DMF, distilled water, acetone, and 2-propanol with sonication for 20 min.

List of Tables

Table of Contents

1. Introduction

1.1 Background

1.1.1. Organic-inorganic hybrid perovskite solar cells

Recently, the use and demand of fossil fuels, which are finite resources, have surged due to rapid economic growth and overpopulation, and mankind have been working to unearth alternatives in the face of energy exhaustion problems. Since solar energy is an infinite, clean and renewable alternative energy source, scientists have been researching various types of photovoltaics (PVs) for decades, such as Si [1], Cu-In-Ga-Se [2], polymer [3], and dye-sensitized solar cells (DSSCs) [4]. However, due to the expensive production cost by the scarcity of specific elements, or poor efficiency, there was a limit to a wide range of applications in daily life.

Perovskite solar cells (PSCs) first reported in 2009 by Kojima et al. [5], which is of great interest in current PV research due to their extraordinary performance. Over the past decade, a technical standard of PSC has progressed at a tremendous pace, and the state-of-the-art PSC has the highest certified power conversion efficiency (PCE) of 23.7 %. The perovskite has a constitutional formula of ABX_3 in which organic

and inorganic materials are mixed as a variety of combinations [A = $CH_3NH_3^+$ (methylammonium, MA), $NH{=}CHNH_3^+$ (formamidinium, FA), Rb^+, Cs^+; B = Pb^{2+} or Sn^{2+}; X = I^-, Br^-, Cl^-] **(Figure 1)** [6]. This photo-capturing material has the unique photoelectric characteristics, e.g. broad absorption spectrum [7], high extinction coefficient [8], long charge diffusion length [9], high mobility [10], and ambipolar charge transport ability [11], which can be further reinforced or modified through compositionally modulating the ratio of the cations and halides **(Figure 2)** [12, 13]. This PSC can be simply assembled by solution processes under the low-temperature (LT) and ambient conditions, which signifies a considerable economic advantage, and a low restriction on fabrication process. Owing to such cost-competitiveness and creditable performance over 20 %, the interest of study pays increasingly attention to commercialization of the PSCs as well as promoting performance. To assist in commercialization, a great deal of effort has focused on increasing the operational areas [14]; scalable coating processes [15]; and long-term tenability in ambient air [16], heat [13], and ultraviolet (UV) rays [17] **(Figure 3)**.

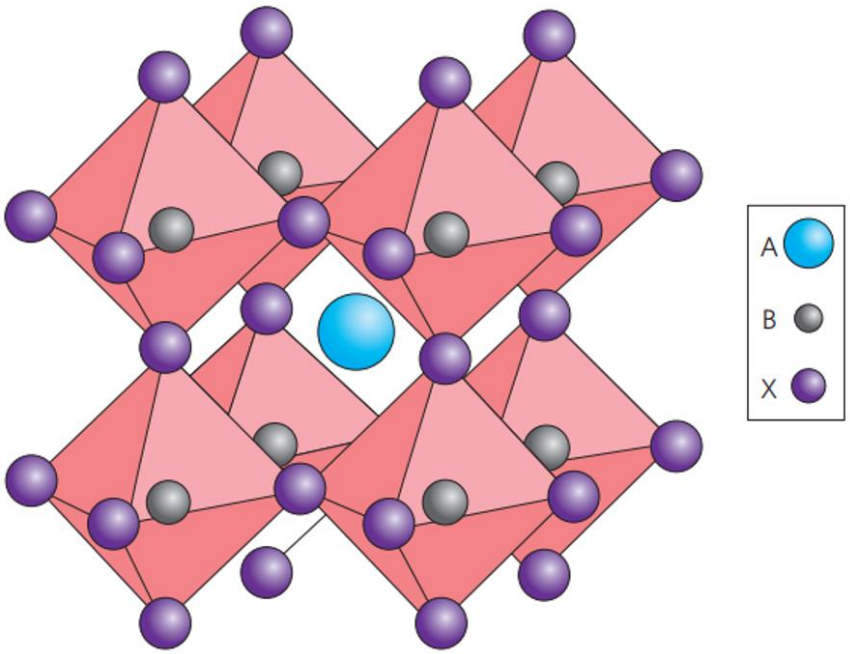

Figure 1. Cubic perovskite crystal structure; A: large cations, such as $CH_3NH_3^+$, $NH{=}CHNH_3^+$, Rb^+, Cs^+; B: small cations, such as Pb^{2+} or Sn^{2+}; X: halogen ions, such as I^-, Br^-, Cl^- [6].

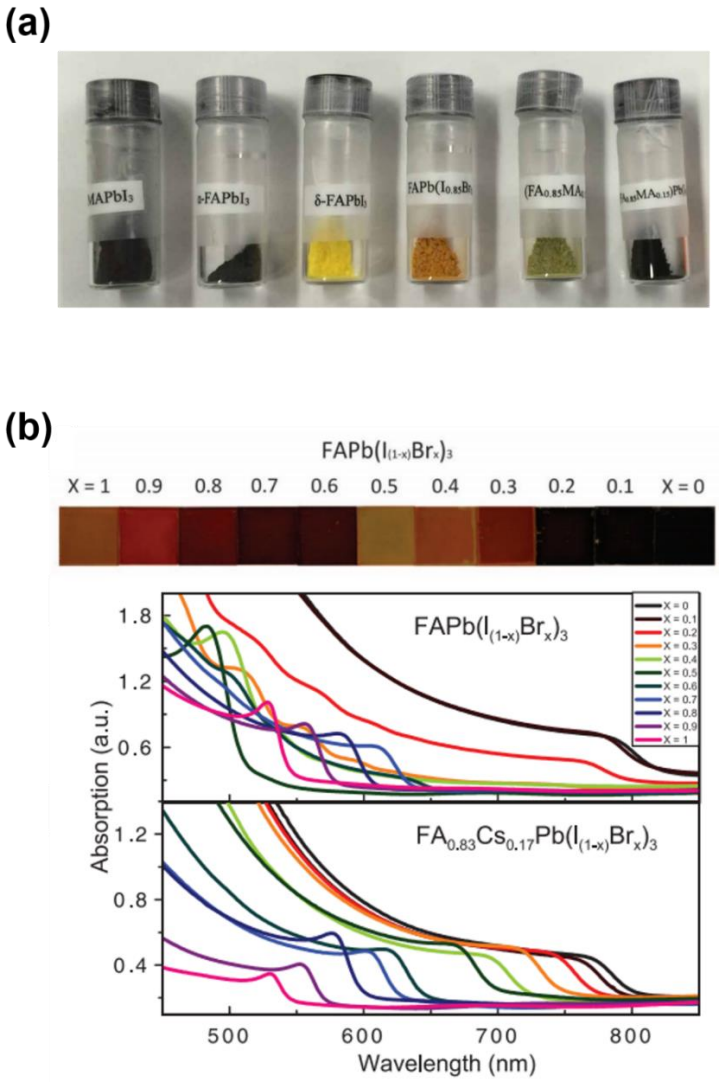

Figure 2. (a) Compositionally engineered lead halide perovskite powder, which was prepared by mixing the MABr, FAI, PbI_2 and $PbBr_2$ with a variety of molar ratio [12]. (b) Evolution of perovskite film appearance and light absorption ability according to perovskite composition control [13].

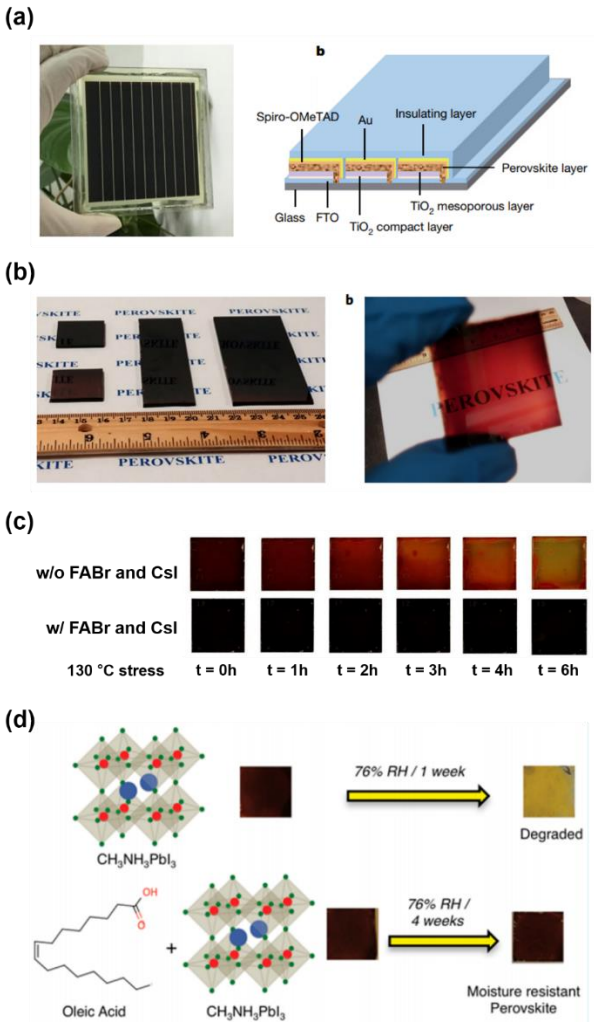

Figure 3. Researches to assist in commercialization of PSCs. (a) Fabrication of PSC module with large operational areas [14]; (b) scalable coating with doctor-blade [15]; (c) long-term stable perovskite film under thermal stress by incorporating cesium iodide (CsI) [13]; (d) moisture-resistant perovskite film by introducing oleic acid [16].

1.1.2. Device configurations of PSCs

General configurations of PSCs can be classified into two types depending on the direction of charge carrier movement: the “n-i-p” and “p-i-n” stack architecture called “regular” and “inverted” type, respectively as shown in **Figure 4** [18]. The regular-type is constituted by transparent conductive oxide (TCO)/hole-blocking layer (HBL)/perovskite/hole-transport layer (HTL)/metal structure. In case of the inverted type that is a diametrical structure to the regular type, the HTL is firstly introduced on the TCO. The regular form of PSCs can be further subdivided into two categories, mesoscopic- (MS-) and planar-type, depending on the presence or absence of mesoporous layer (MPL) above the HBL. The MPL, constructed by a set of metal oxide nanoparticles [19], or nanostructure [20], has a large surface area to accept effectively photoexcited electrons. However, lots of factors, e.g. size and purity of the nanostructure, and paste synthesis for the MPL, must be considered precisely to derive the high-quality MPL, which deteriorates performance reproducibility. Moreover, high-temperature (HT) calcination at 500 °C is required to remove the residual organic compounds in the paste and to solidify the inter-particle necking, which is an energy-consuming process, significantly.

To resolve the structural disadvantages, the planar PSC was firstly suggested by Ball et al. with the PCE of 5 % [21], verifying that the PSC is capable of operating without the MPL owing to ambipolar charge transfer [11], and long diffusion length characteristics of perovskite [9]. In the planar form, a well-made n-type HBL (or called as an electron transport layer, ETL) is one of the most pivotal factors to boost device efficiency. The HBL not only dominates selective collection of electrons at the TCO, but also prevents direct contact between the TCO and hole-transport material (HTM) deposited on top of perovskite. An appropriate selection of an n-type semiconductor as the HBL, is the first step to reach high-performance because this determines dominantly electron mobility and conductivity. These factors have a strong influence on electron transfer and the defect-induced recombination dynamics at the perovskite/HBL interface. In addition, designing optimal energy level alignment, between the HBL and perovskite, drives up the charge transfer efficiency from perovskite to the HBL [22]. Therefore, many approaches have been made an attempt to satisfy the requirement, e.g. investigation of favorable metal oxide [23], atomic doping [24], surface functionalization [25], and bilayer structure [26], etc., which successfully led to jumping the performance of planar PSC (**Figure 5**).

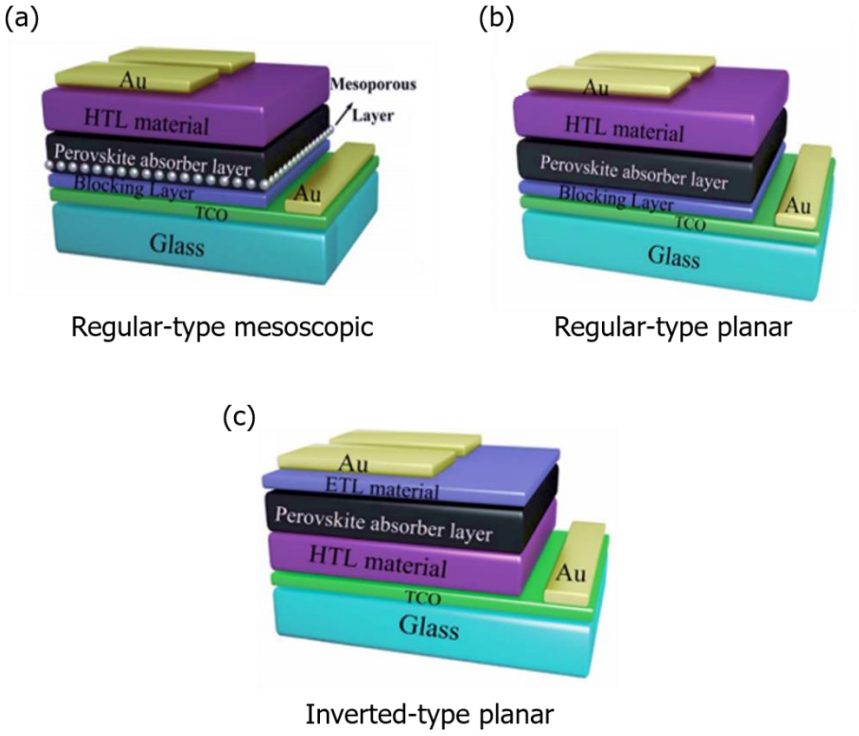

Figure 4. Various structural configurations of PSCs; (a) regular-type (n-i-p) mesoscopic, (b) regular-type planar, and (c) inverted-type (p-i-n) planar structure [27].

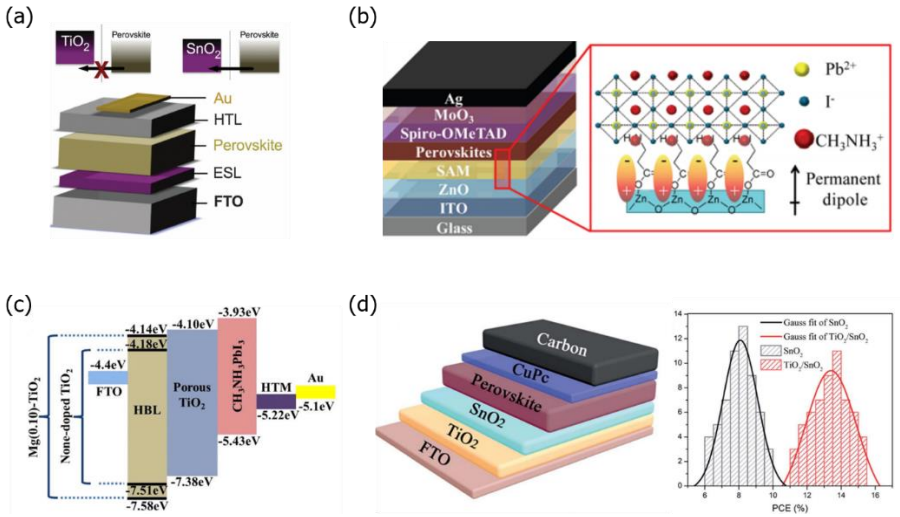

Figure 5. Numerous attempts to improve performance of the planar PSCs, such as (a) investigation of favorable metal oxide between TiO_2 and SnO_2 [23], (b) surface functionalization with self-assembling monolayers [25], (c) atomic doping on TiO_2 with magnesium ion [24], and (d) TiO_2/SnO_2 bilayer HBL structure [26].

1.1.3. Simplifying the process and structure of the planar PSCs

Among the lots of topics investigated for the purpose of accelerating commercialization of PSCs, simplifying production processes and structures is one of the key research directions to improve productivity and price competitive **(Figure 6)**. Process simplification means to fabricate components of the PSC using more productive and economical methods. Particularly, the process for fabricating metal oxide-based HBLs requires the longest annealing time and HT conditions among the whole components of PSCs. To achieve high throughput and make the fabrication of the PSCs industrially viable, the annealing temperature and duration times must be reduced. Therefore, many researches have applied novel energy sources in annealing process.

Structural simplification is to redesign the conventional structure of PSCs. The most frequent approach is to remove a specific layer adjacent to perovskite or to replace electrode with a material deposited in a convenient way. The elimination would be economically and productively helpful if there is no trouble to operate device. Also, ambient stability can be enhanced because the defects induced by the existing layer are ignored. However, low-performance and severe hysteresis are still big issues of the simplified PSCs.

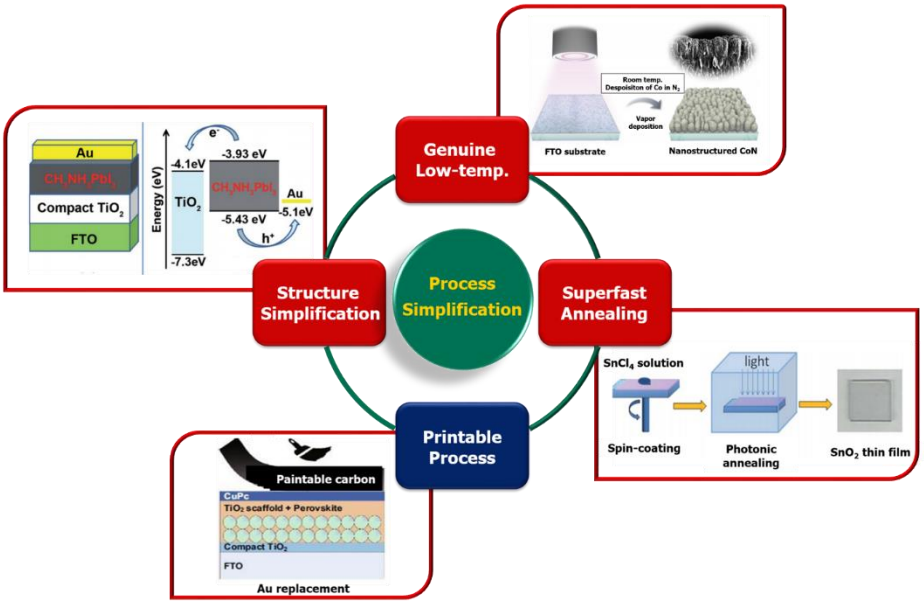

Figure 6. Numerous approaches for engineering process and structure of PSCs for simplifying the fabrication procedure.

1.1.3.1. Low-temperature and fast oxidation in the HBL preparation

The HT sintering (above 450 °C) frustrates a plan of the application into a flexible substrate. Furthermore, this harsh sintering created a large extent of defect states such as oxygen vacancies [28]. Therefore, mild sintering approaches were scrutinized for the sake of avoiding the side-effects and establishing the foundations for practicalization.

Rational approaches, e.g. thermal-decomposition (TD) by spin-coating [29], colloidal SnO_2 nanoparticle dispersion [30], and atomic layer deposition [31], were frequently picked, in that these can be processed under the LT condition **(Figure 7)**. The TD is one of solution method in which a specific metal precursor selected as starting material is spread on a TCO by spin-coating [32], spray-cast [33], and chemical bath deposition [34], etc., followed by subjecting to the thermal-annealing (TA) under ambient condition. This is convenient to modulate precursor composition by just mixing the prearranged chemicals, permitting to explore readily the multidirectional trials for optimizing the film quality. Therefore, the TD has excellent reproducibility and is not environmentally constrained. In addition, further development in the TD is expected because the TD is an economical and practical strategy capable of fast manufacturing the TFs.

Annealing process, apart from the film deposition, is a post-treatment for oxidizing as-coated TFs, accordingly peculiarizing semiconductive properties to the TFs. The LT-processed TD normally includes the TA after the film coating at a temperature of above 180 °C for 1 h [29], However, judging from more stringent standards, the temperature of 180 °C is still harsh enough to make the term "low-temperature" colorless, and it is obligatorily accompanied by a long duration time for absolute oxidation, which is very skeptical to unit-price. To circumvent these obstacles, distinctive annealing methods have been devised to form the TFs at the LT environment, e.g. micro-wave [35], ultraviolet/ozone (UV/O_3) [36], and laser annealing **(Figure 8)** [37]. Recently, a UV/O_3 sintering method was used to fabricate a SnO_2 HBL of the planar PSC; the UV/O_3-sinterd HBL (*ca.* 70 °C) exhibited better optical and electrical properties compared to the TA-based HBL (180 °C) [36]. Furthermore, a millisecond-pulsed photonic annealing (MPPA) method was employed to activate the HBL, demonstrating the unnecessariness of time- and energy-consuming annealing process [38]. Nevertheless, the planar PSCs, including HBLs developed by the above-mentioned LT and fast processes, still exhibits an unsatisfactory level of performance compared with the TA approach. Therefore, there is a desperate need for an

innovative oxidation strategy capable of producing not only the high-quality HBL with fast rate at the genuine LT but also outstanding performance that is comparable with the TA-based PSCs.

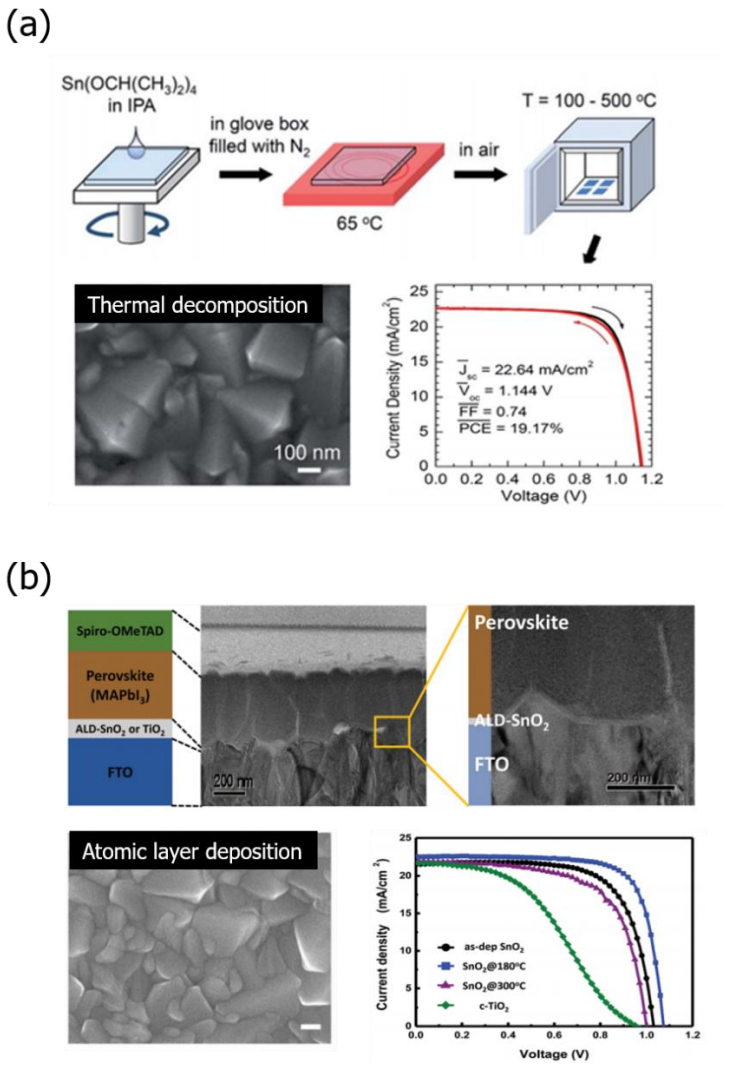

Figure 7. (a) Schematic experimental process for the fabrication of HBL *via* thermal decomposition method [32]. (b) Cross-sectional field emission-scanning electron microscopy (FE-SEM) view the PSC including ALD-derived HBL and surface morphology of the ALD-based SnO_2 HBL [31].

(a) UV/O_3 sintering

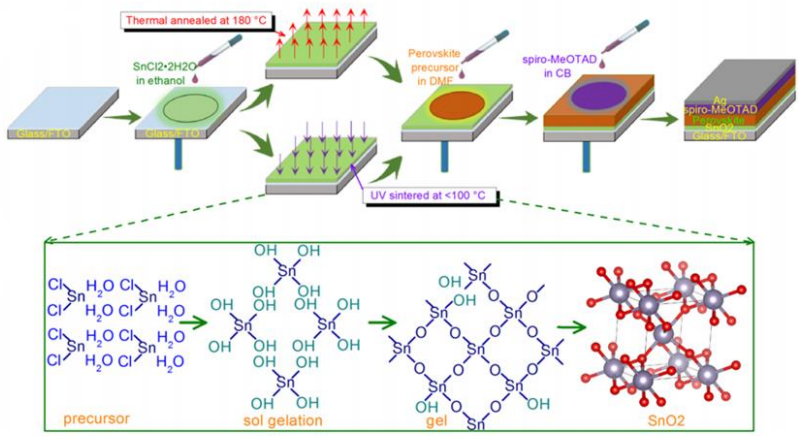

(b) MPPA annealing

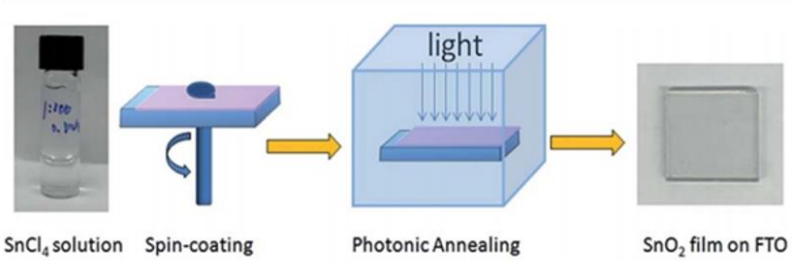

Figure 8. Schematic illustration of the SnO_2 TF fabrication process with (a) the UV-irradiation [36] and (b) MPPA method [38]. The UV-sintered SnO_2 TF is prepared with spin-coating of the hydrated $SnCl_2$ precursor and annealing by UV irradiation. In the (b), the SnO_2 TF was formulated with spin-coating of $SnCl_4$ precursor and annealing by photonic annealing.

1.1.3.1.1. Atmospheric Ar/O_2 plasma oxidation

Atmospheric-pressure Ar/O_2 plasma is a technique that has been mainly used for cleaning carbon or other contaminants on the surface of electrode substrate using energetic plasma generated through the radio-frequency discharge [39]. Since the continuously accumulated contaminants aggravates performance of electronic devices [40], the plasma treatment has been an essential pre-processing step before full-out fabrication [41, 42]. In addition, it can reduce the water contact angle and dramatically improve the wettability of the solution [43]. Furthermore, the Ar/O_2 plasma treatment increases the amount of surface oxygen content and saturates free surface bonds or oxygen vacancies [44], which controls surface chemical and electronic characteristics [45]. This alteration in the lattice structure can further modify the energy band structure of semiconductors, increase electron mobility, and manage a charge carrier transport ability [46].

The atmospheric Ar/O_2 plasma emits various types of reactive oxygen species, e.g. O^{2+}, O^{2-}, O_3, O, O^+, O^- [47], which have strong energy to break alkoxy and hydroxyl groups of sol-gel-derived TF **(Figure 9)**, or to and can construct the metal-oxygen-metal (M-O-M) bonds of metal oxide. The plasma oxidation was carried out to metal films such as Sn,

Si, and Al, activating the SnO_2 [48], SiO_2 [49], and Al_2O_3 [48,50] films, respectively. It was certified that the oxide derived by the active plasma had better electrical properties than those formulated by thermal oxidation with the stable bond structure [49]. Also, the plasma was treated on solution-processed metal precursors of $ZnCl_2$ and $SnCl_2$, to oxidize into Zn_2SnO_4, relaxing the surface defects [51].

As described above, the atmospheric Ar/O_2 plasma can be an effective annealing way to yield a high-quality oxide TFs at a LT condition with forming a dense M-O-M network [52]. In addition, surface defects derived by the HT annealing can be considerably reduced, thereby maximizing the charge transfer efficiency [46]. Despite these merits, the TA is mostly used for the oxidation of metal oxide in PVs. and this Ar/O_2 plasma was considered having only a function of surface activation for upgrading the wettability of the already oxidized HBL. Considering the fact that fabrication trend of PVs is the LT and fast process for commercialization, the plasma-annealing (PA) can be an adequate manner to fabricate the metal oxide-based HBL.

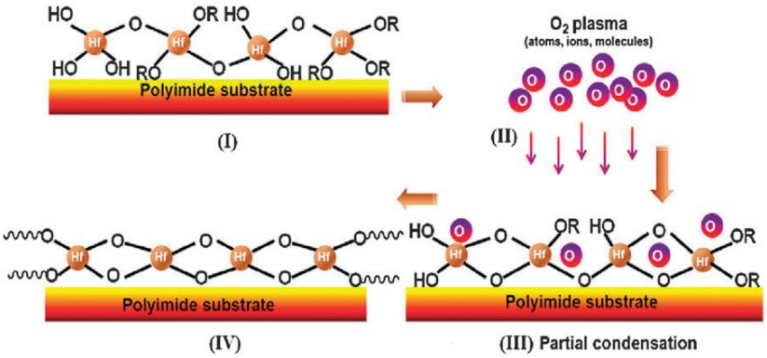

Figure 9. Schematic illustration of the growth of the sol-gel-derived HfO_2 TFs *via* O_2 plasma [44].

1.1.3.1.2. Tin oxide (SnO_2) HBL-based planar PSCs

Various n-type inorganic oxides (e.g. TiO_2 [53], ZnO [54], SnO_2 [29], WO_x [55], In_2O_3 [56], Nb_2O_5 [57], Zn_2SnO_4 [58], and $BaTiO_3$ [59].) are eligible for playing a role as HBL in the planar PSC **(Figure 10)**. Titanium dioxide (TiO_2) have long been recognized to the most suitable candidate for the HBL of PSC, however, several disadvantages of TiO_2, e.g. low electron mobility (10^{-4} $cm^2V^{-1}s^{-1}$), poor conductivity and a photocatalytic effect under UV irradiation, spoiled device performance and stability **(Figure 11a** and **b)** [60-62]. Zinc oxide (ZnO) has been also a good reputation for an ideal alternative as the HBL due to similar band structure with TiO_2 [63] and high electron mobility (200-300 $cm^2V{\cdot}s^{-1}$) [64]. However, the hydroxyl group and acetate ligand on the ZnO surface are likely to decompose seriously the neighboring perovskite [65] **(Figure 11c)**.

Tin oxide (SnO_2) is a rising star in the PSC field as the HBL material due to its analogous electrical features with the traditional TiO_2, and has been often adopted in polymer-based PV [66], DSSC [67], and Sb_2S_3 PV [68]. This not only has a great number of optical and electrical merits, e.g. wide band-gap (*ca*. 3.6 - 4.0 eV) to minimize optical energy loss, harmonized energy level [69], high electron mobility (250 $cm^2V^{-1}s^{-1}$)

[60], and photostability, but also ensures the LT processing [70, 71]. In 2015, the SnO_2 was initially introduced into the PSCs in which the crystalline SnO_2 nanoparticles played roles of both the MPL and HBL, yielding a quite acceptable PCE of 10.18 % [72]. Before long, Ke et al. firstly reported the TD-derived SnO_2 HBL-based PSCs with the PCE of 17.21 % [29], where the diluted tin (II) chloride ($SnCl_2$) solution was spin-coated on the substrate and thermally annealed at 180 °C for 1 h. Similarly, Jung et al. produced a great performance of 19.2 % using tin isopropoxide as the solution precursor for SnO_2 ETL [32], emphasizing the significance of starting materials of the TD-derived SnO_2 HBL.

Namely, the efficiency of planar PSC have increased gradually with employing the SnO_2 HBL **(Figure 12)**, and its application frequency is also increasing. In order to commercialize the PSC, more active researches have to be conducted on manufacturing high-quality SnO_2 HBL successfully.

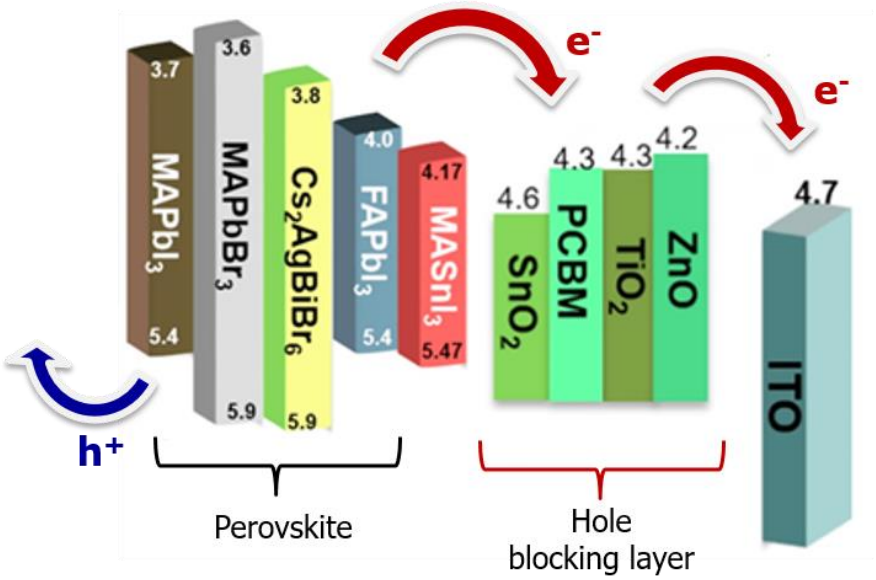

Figure 10. Energy level diagram for diverse common HBLs together with organic-inorganic halide perovskites. The HBL accepts photo-excited electrons stayed in perovskite, and blocks the contact between TCO and HTM [73].

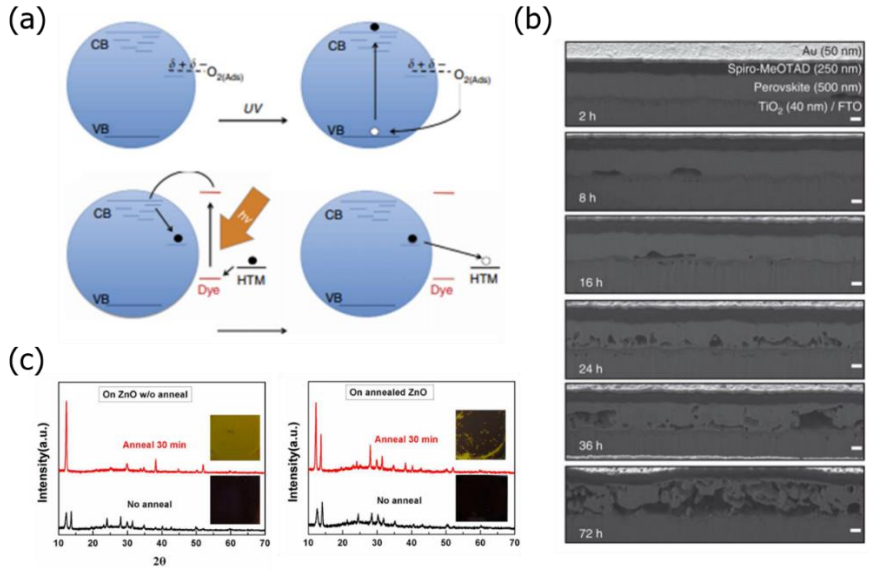

Figure 11. (a) UV-induced degradation mechanism of TiO_2; the deeply trapped electrons are recombined with the holes on the HTM [61]. (b) Degradation patterns of TiO_2 HBL-based PSC as a function of light exposure time under ambient conditions [62]. (c) X-ray diffraction (XRD) patterns and photographs of perovskite film coated on the ZnO-based HBL [65].

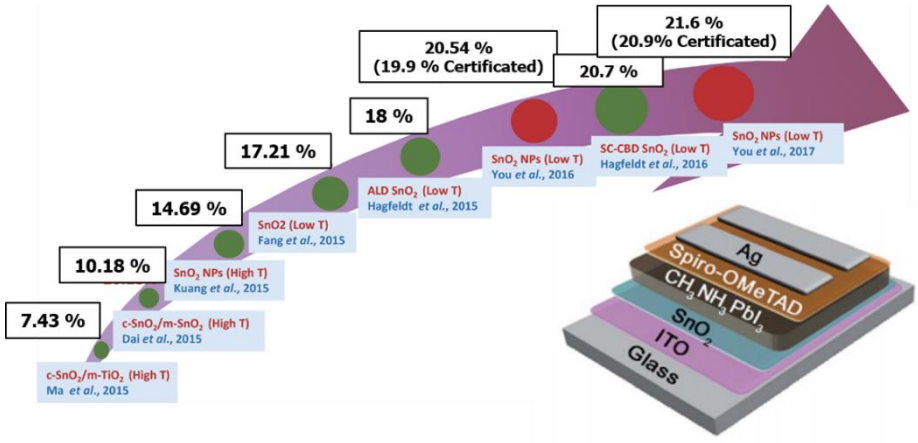

Figure 12. Evolution of efficiency in the SnO_2 HBL-based PSCs [70], and its ordinary device structure [74].

1.1.3.2. Device structure simplification in planar PSCs

As another approach to improve productivity of PSCs, the configuration of PSCs have been gradually simplified with eliminating a specific layer **(Figure 13)**. In 2012, Lee *et al.* adopted an insulating aluminium oxide (Al_2O_3) as a scaffold material of MS-PSC instead of the conventional TiO_2 accepting photo-excited electrons from perovskite, and confirmed unexpectedly improved performance in the Al_2O_3-based device [75]. This phenomenon implicated that the perovskite is capable of transporting charge carriers directly without any charge transport layer. Moreover, since most of photogenerated excitons will thermally dissociate under operating temperatures owing to low exciton binding energy of perovskite (~50 meV), the PSCs functions as a typical inorganic semiconductor thin-film PVs, and a high surface area of the MPL is not required [76]. Owing to the discovery, the MS-PSC was successfully simplified into the planar-type including only the HBL as an electron conductor.

By extension, more simplified PSCs were created by removing even the existing HBL in the planar PSC with the structure of FTO/perovskite/HTL/metal (named as a HBL-free PSC) [76], to further reduce unit-costs and operation instability caused by the HBL. Although

this minimized structure has convenience in process, the electron-hole recombination at the FTO/perovskite interface and slow electron extraction decreased device efficiency. Therefore, novel interface engineering and perovskite morphology control are required in the HBL-free PSCs to solve the critical issues of device operation.

Apart from subtracting the HBL, a removal of HTL from the planar PSCs was also carried out; the metal electrode was deposited immediately on the perovskite with a structure of FTO/TiO_2/perovskite/Au [77, 78]. However, this structure showed a poor PCE of *ca*. 10 %, and was vulnerable to chemical degradation of perovskite under ambient environment, due to a loss of the protective film. Therefore, removing an underlying layer of perovskite may be desirable in order to further simplify the conventional planar PSCs, which can ensure moderate performance and durability of the perovskite film.

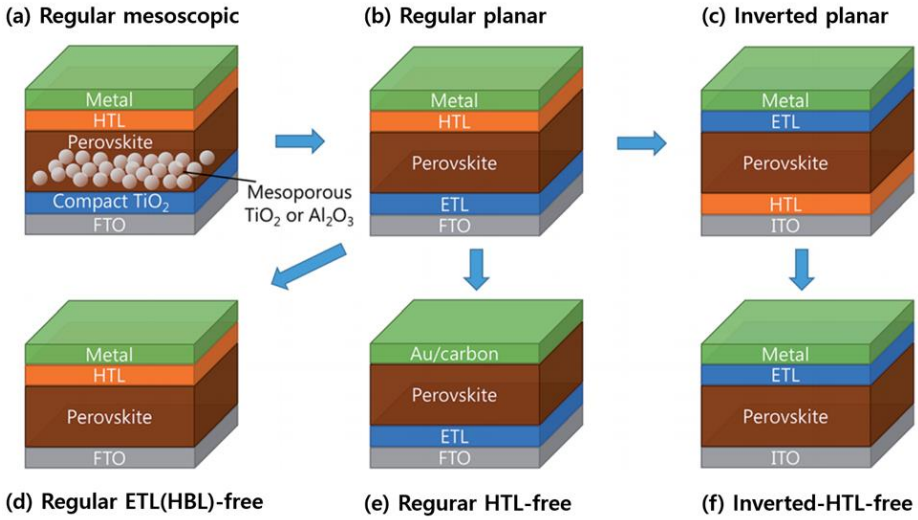

Figure 13. An evolution of the PSC structure; (a) Regular mesoscopic type can be simplified to (b) regular or (c) inverted planar types. The planar structures can be further simplified to (d) HBL-free, (e) regular HTL-free and (f) inverted HTL-free types [79].

1.1.3.2.1. Hole-blocking layer-free PSCs

The HBL-free PSCs denies to deposit an n-type HBL on TCO unlike the regular-type planar PSC. Even though the HBL has been recognized as an essential element for the smooth operation of PSCs, a first exceptional PCE of 13.5 % was reported in 2014 by the HBL-free PSCs [76]; which was indistinguishable efficiency compared to ZnO-HBL-inserted PSCs **(Figure 14)**. Since residual PbI_2 present at the interface between the TCO and perovskite can function as a built-in HBL, the chance of charge recombination was reduced despite the removal [76]. In addition, it is simulatively investigated that the HBL-free PSCs have a potential to yield the PCE over 19 % with a perovskite of $CH_3NH_3PbI_{3-x}Cl_x$ ($MAPbI_{3-x}Cl_x$) [80]. Furthermore, this elimination not only can solve the HBL-induced disadvantages, such as exciton recombination at surface-defects and photocatalytic effect, but also improves productivity and reproducibility of the PSCs because lots of steps for preparing the HBL can be ignored, e.g. starting material synthesis, deposition and annealing stages. However, the already reported PCEs were still lower than that of the conventional planar PSC, which was responsible for failure to prevent appropriately direct contact between the HTM and TCO surface, and poor electron migration attributed by the mismatched

energy level between the TCO and perovskite. Additionally, it is confronted with a severe hysteresis issue due to unbalanced charge transfer rate; alleviation of this hysteresis is essential to yield a highly stabilized power output (SPO) [81]. There is thus an enormous requirement to find an innovative way for surmounting the current drawbacks and improving performance of HBL-free PSCs.

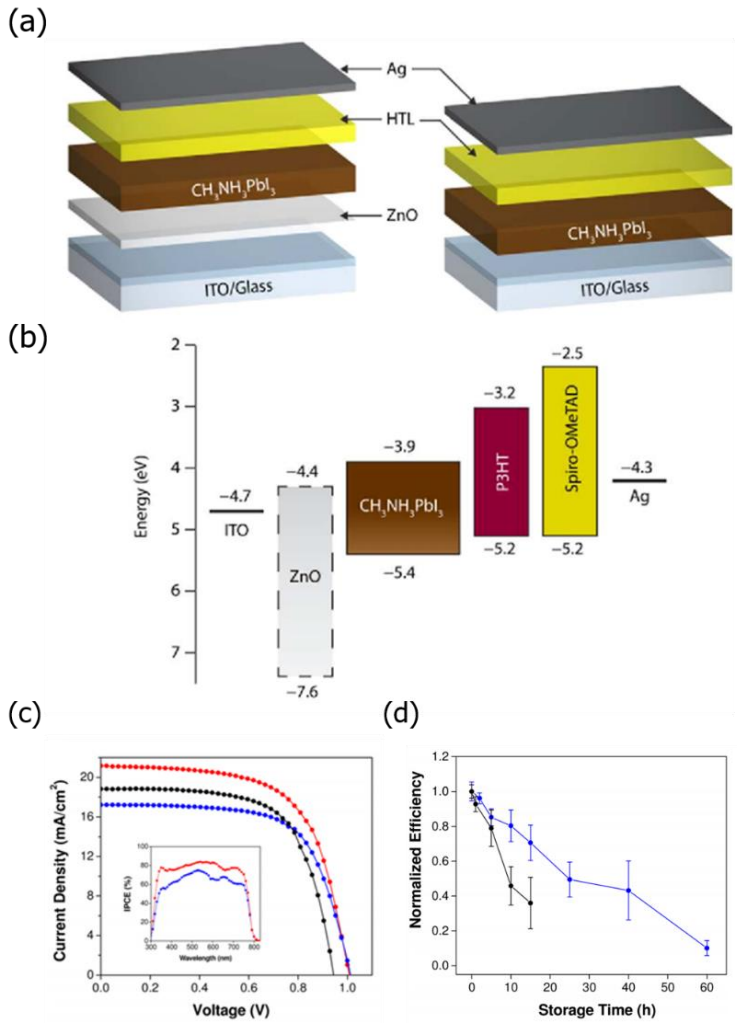

Figure 14. (a) Schematic structure of the HBL-free PSC and (b) its energy band diagram. (c) *J-V* curves of PSCs: ZnO HBL and P3HT HTL (black line), no HBL and P3HT HTL (blue line), and no HBL and spiro-OMeTAD (red line). (d) Stability test as a function of storage times for the of PSCs both with (black line) and without (blue line) ZnO HBL [76].

1.1.3.2.1.1. Deposition of perovskite film

Performance of the HBL-free PSCs is closely related to the properties of perovskite film, since perovskite functions both light-absorber and the HBL. For that reason, formulating perovskite films optimized for the HBL-free PSCs is a first key to performance enhancement. Surface morphology and crystallinity of perovskite are strongly influenced by processing methods, which ultimately has a direct impact on its optoelectronic properties, e.g. extinction coefficient, charge diffusion length, mobility, and trap density.

Generally, the formation of perovskite is categorized into "non-solution" and "solution" routes according to the state of precursors. The former mostly designates a physical vapor deposition conducted by a vacuum thermal evaporator using powder sources **(Figure 15a)** [82]. Although the vacuum deposition is suitable for large-scale or multi-layer perovskite production, it is awkward to not only regulate the substrate and evaporation temperatures for the smooth perovskite deposition, but also adjust amount of initial sources for the ideal stoichiometry and thickness. Inversely, the "solution" approach have utilized liquid precursor as a starting material; the organic and inorganic compounds are mixed with one or several kinds of solvents, for instance, *N,N*-

dimethylformamide (DMF), dimethyl sulfoxide (DMSO), gamma-butyrolactone or N-methyl-2-pyrrolidone. Traditionally, the spin-coating is the most representative method in the solution process due to its simplicity and straightforward control of film thickness. The drastic progress in the quality of perovskite through the spin-coating has been accomplished by "solvent-engineering (SE)" technology **(Figure 15b)** [83]. The SE signifies to induce the stabilized intermediate phase of PbI_2-DMSO-MAI before the crystallization of perovskite by dropping anti-solvent on the spinning wet-perovskite with selectively washing the remained solvent of DMF, leading to uniform and dense perovskite layer with the TA. It was the driving force to improve the average efficiency of the PSCs to *ca.* 19 %, and a Lewis base-adduct approach was then announced in a more complementary form of SE, raising the efficiency to *ca.* 20 % [84, 85]. However, the perovskite crystallized only by the conventional SE has limitations including the small grain size and high defect density, which debases light-capturing ability and intensifies non-radiative recombination induced from grain boundary (GB) defects. Therefore, it has been necessary to devise a strategy for acquiring the large grain-based perovskite film through modifying the precursor stoichiometry, adding an additive, or modifying the annealing process.

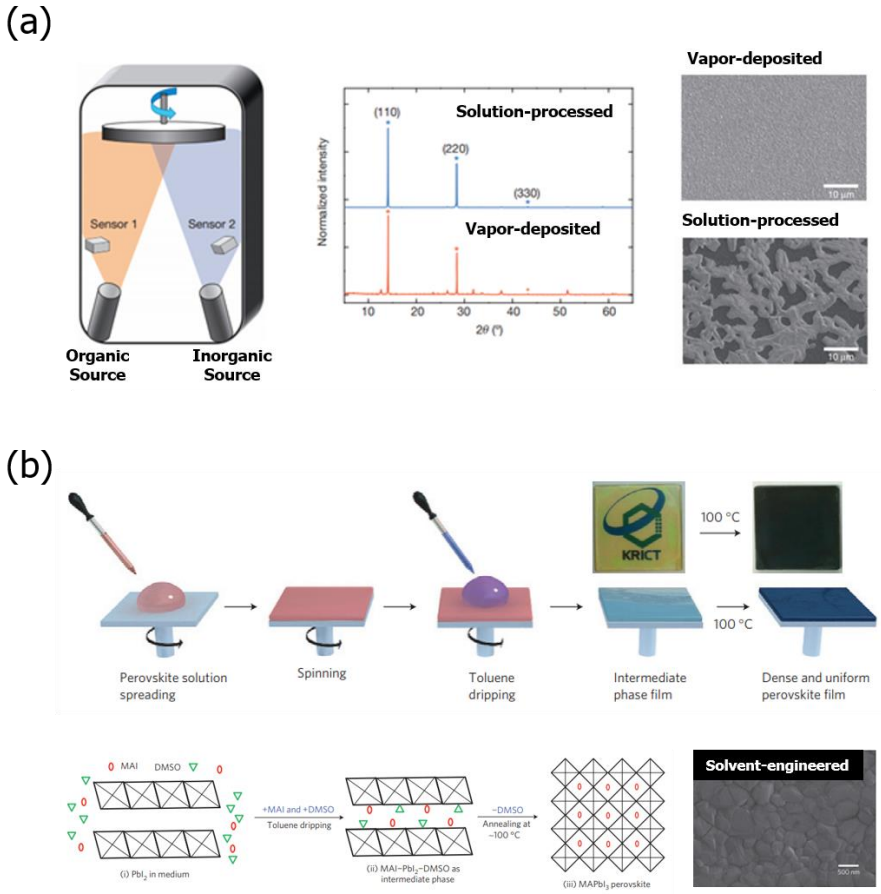

Figure 15. (a) A representative non-solution process for perovskite preparation: schematic diagram for dual-source thermal evaporation to deposit the perovskite film, XRD pattern and FE-SEM images of the result film [82]. (b) Schematic procedures to fabricate the solution processed-perovskite film: solvent-engineering was applied to induce highly crystalline perovskite *via* an intermediate phase formation [83].

1.1.3.2.1.2. Grain size engineering of perovskite film

Augmenting perovskite grain size can resolve the drawbacks of perovskite (low crystallinity and high defect density) and enhance the performance of PSCs with relieved hysteresis by suppressing the charge accumulation during the PSC operation [86]. Generally, in order to enlarge the crystals, it is central to elicit rapid homogeneous nucleation and impede crystallization reaction *via* chemical and physical handling [87, 88]. This grain engineering can be classified into two kinds of approaches: pre- and post-treatment on the basis of perovskite coating timing **(Figure 16)**. Firstly, the pre-treatment includes the deformation of coating system and adjustment of starting material composition. For instance, the hydrophobic substrate led to forming the high aspect ratio of perovskite grain because of the reduced drag force on non-wetting surfaces **(Figure 17a)** [89]. A solution-based hot-casting technique produced to form millimeter-scale crystalline grains; the hot perovskite solution of 70 °C was spin-coated on the hot substrate of 180 °C, which confined the excessive solvent on the hot-substrate with delaying the evaporation, accordingly prolonging the growth of perovskite and enlarging the grain size **(Figure 17b)** [86]. Besides, chemically engineered precursors derived by addition of various enhancers, e.g.

CH_3NH_3Cl (MACl) [90], $Pb(SCN)_2$ [91], CH_4N_2S [92], and polymers [93], have yielded monolithically grained perovskite with improved photo-physical properties **(Figure 17c)**. However, precursor engineering or hot-casting method cannot regulate indiscriminate nucleation sites and requires pinpoint control of composition; this is fastidious to reproduce other than in the hands of skilled technicians.

Alternatively, a variety of post-treatment processes have also been introduced to enlarge the perovskite grain size. The post-treatment is a general term including an annealing procedure and additional treatment on the fully annealed-perovskite, which have been frequently combined with the TA and compensates shortcomings of as-prepared pristine perovskite by reorganizing the crystal structure or regulating the solvent evaporation [94]. An infrared flash [95], electric field [96], and micro-wave [97], were employed by replacing the conventional TA in perovskite crystallization to improve the perovskite grain size and crystallinity. Also, treating an additional alkylammonium halide on the full-grown perovskite enlarged the perovskite crystals, where the small-grains were dissolved by the alkylammonium halide and regrown into larger crystals *via* the Ostwald-ripening process [98]. Lastly, vapor-induced post-treatments have been often used to increase the grain size,

where the vaporized chemical is permeated into a perovskite film, heals the existing defects, and rearranges crystal structure. As a representative technique, solvent-annealing (SA) was reported in the PSCs by Huang *et al*. **(Figure 18a)**; a perovskite-coated substrate was covered with a petri dish during the TA, and a dash of solvent, such as DMF or DMSO dissolving the perovskite, was inserted at the edge of the petri dish. Then, the crystallization and degradation of perovskite were repeated due to heat-energy and the solvent vapor, respectively, which drives the increase of crystals [99]. Similarly, the strong Lewis base pyridine vapor was used to bleach the $MAPbI_3$ into the MAI and $PbI_2(pyridine)_2$ **(Figure 18b)**, which was spontaneously recrystallized into the high-crystalline perovskite [100]. These measures created the drastically enlarged perovskite grains, which delivers performance enhancement because the charge carrier diffusion length is proportional to grain size, and non-radiative recombination at shallow defect states, concentrated at GBs, can be mitigated, simultaneously [101, 102].

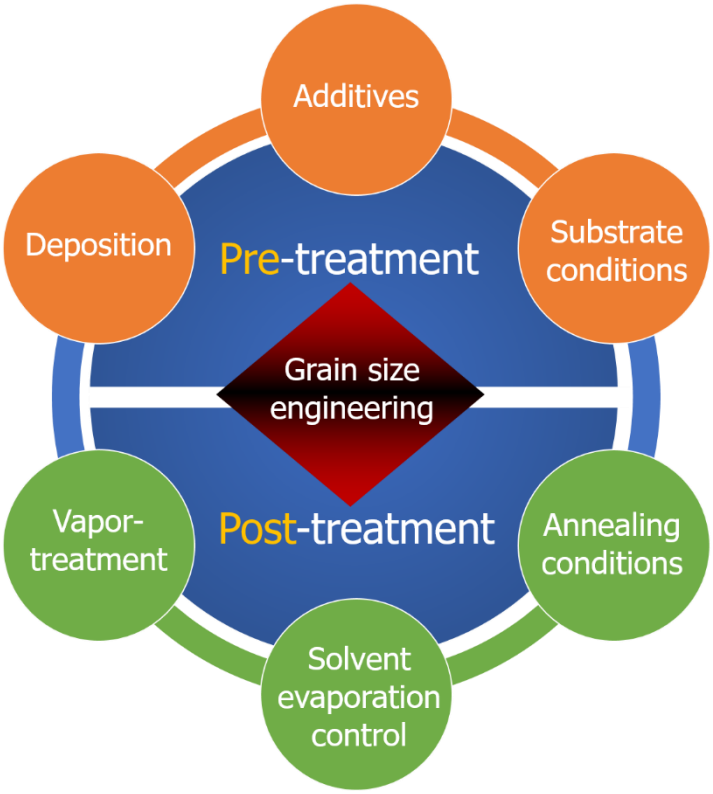

Figure 16. Schematic diagram showing two kinds of approaches to increase perovskite grain size: pre- and post-treatment.

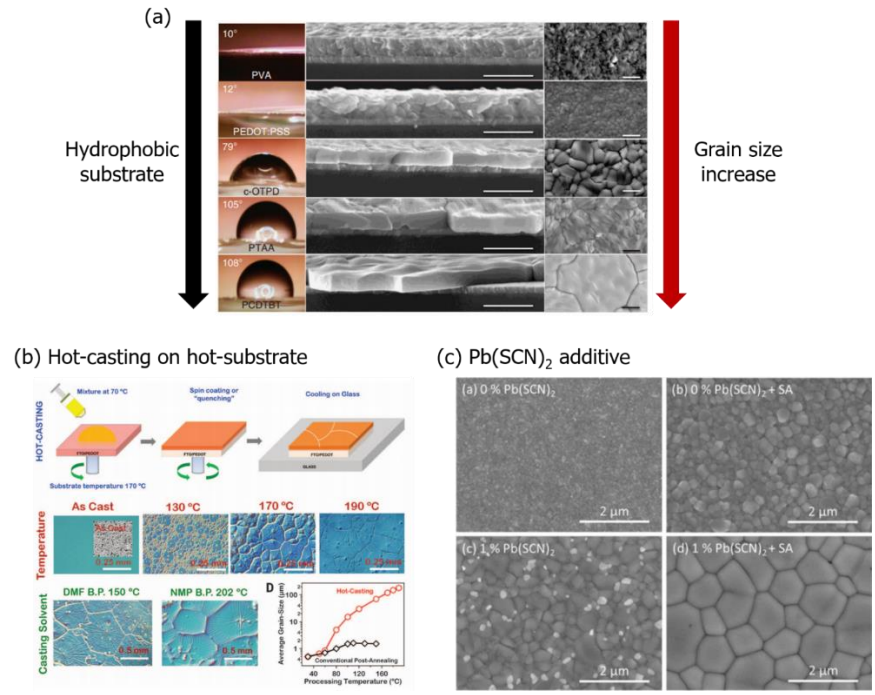

Figure 17. Various strategies for enlargement of perovskite grain size. (a) Non-wetting surface method: hydrophobic substrate induces to form the high aspect ratio perovskite crystal [89]. (b) Hot-casting method: hot-precursor is spread on a hot-substrate, which produces micrometer-sized perovskite grains [86]. (c) Introduction of additive ($Pb(SCN)_2$) into perovskite precursor can facilitate an increase of perovskite crystals [91].

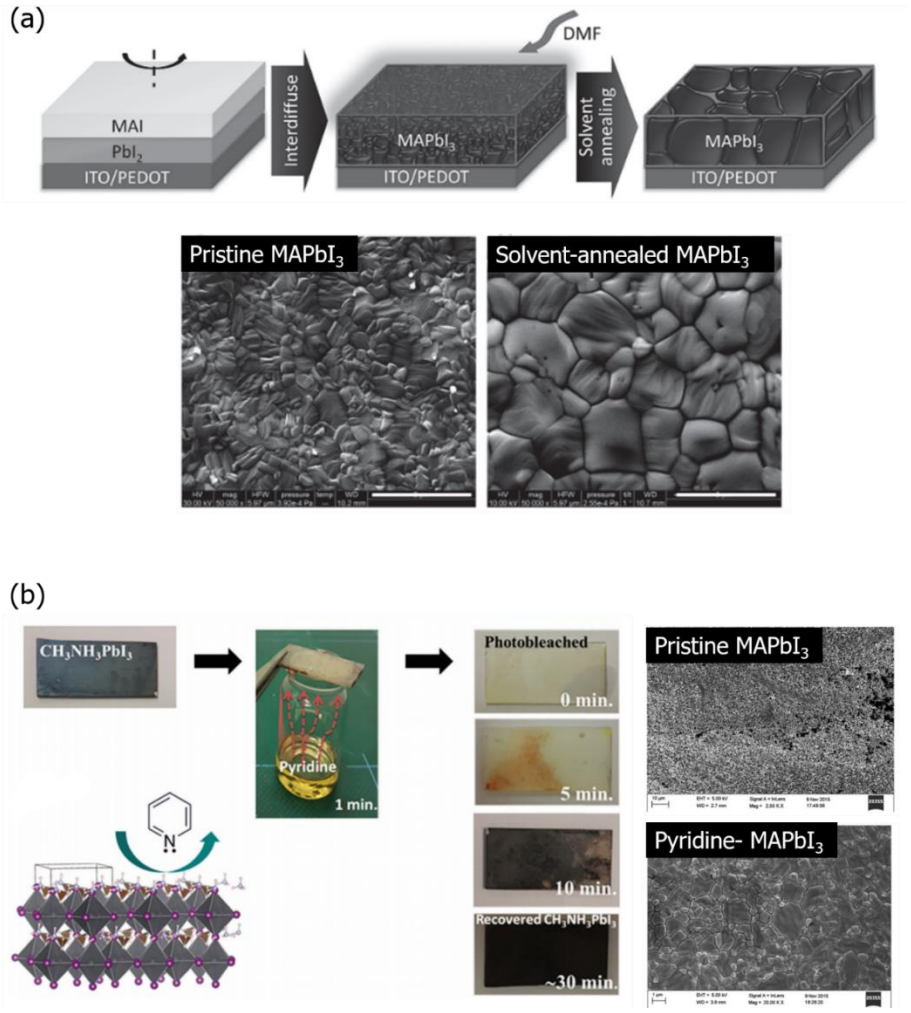

Figure 18. Two kinds of vapor-induced post-treatments to upgrade a quality of perovskite: (a) solvent-annealing process, which is applied during TA process of perovskite film [99]. (b) Pyridine vapor treatment on the full-grown perovskite film to induce recrystallization [100].

1.1.3.2.1.3. Interface engineering for efficient HBL-free PSCs

To successfully realize to fabricate a highly efficient HBL-free PSC, it is pivotal to separate effectively the photoexcited charge carriers from perovskite and quickly convey them toward the TCO despite an absence of the HBL [103]. This charge-migration-dynamics between the TCO and perovskite is strongly influenced by a difference in work function (WF), and surface morphology. Various interface engineering strategies have been carried out to improve performance of the HBL-free PSC up to the equivalent level with the HBL-inserted PSC.

Ke et al. assembled the HBL-free PSCs of 14.1 % by employing a UV/O_3-treated FTO and perovskite of $MAPbI_{3-x}Cl_x$, where the coverage of perovskite and carrier lifetime were improved by passivating the FTO/perovskite interface with chlorine [104]. In addition, an n-type dopant such as cesium carbonate was treated on the TCO surface, which tuned the WF of FTO and improved electron transfer and PCE up to 15.1 % **(Figure 19a)** [105]. In a similar way, a bathocuproine film, an insulated interlayer, was introduced on the FTO to modify surface WF, and led to a considerably high efficiency of 19.07 % in the HBL-free PSC **(Figure 19b)** [106].

Another tractable way for swift charge extraction from the perovskite

to TCO is to augment the interfacial area between the perovskite and the HBL [107]. Considering the contact zone, odd-shaped metal oxide layers have been often formulated as the MPLs, for example, 3D-TiO_2 nanowires [108], and oriented TiO_2 nano-cones [109]. These reports indicated the significance and benefit of enlarging the interfacial area adjacent to the perovskite on PV performance. However, in case of the HBL-free PSC, not only it is meaningless to build such a complex structure on TCO from the perspective of device simplification, but also the required intricate and uneconomical synthesis procedures are detrimental from the commercial perspective. Therefore, to promote the charge extraction efficiency in the HBL-free PSCs and relieve the hysteresis, the FTO must be transformed into a unique morphology having a large interfacial area.

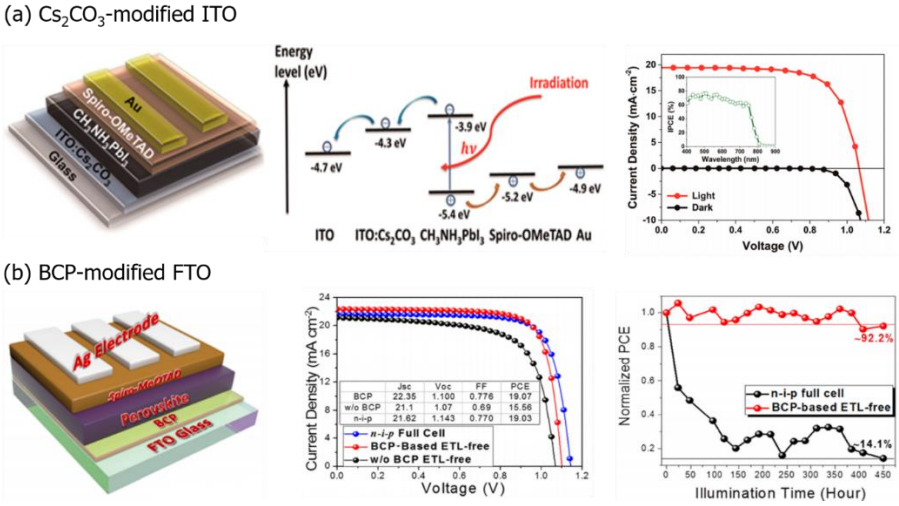

Figure 19. Interface engineering for highly efficient HBL-free PSCs. Introduction of (a) cesium carbonate- or (b) bathocuproine-modified ITO as a TCO substrate of HBL-free PSCs [105, 106].

1.1.3.2.1.4. Electrochemical etching process

An electrochemical process (ECP) is a familiar method used to construct the organic and inorganic nanostructures with unique morphologies, or to etch the surface of metal oxide for increasing surface roughness and forming nanoporousity, which is a simple, cost-effective and LT method. The ECP have been frequently applied to various electronic devices such as sensors [110], PVs [111], and light-emitting diode [112].

Especially, electrochemical etching process (ECEP) has often been introduced as a strategy for surface modification of TCO, which is able to alter not only physicochemical and optoelectrical characters but also interfacial properties. Bae et al. adopted an electrochemically etched FTO as the substrates of DSSCs, which improved photocurrent density through stimulating incident light-scattering at the mesopores formed on the substrate **(Figure 20)** [113]. In addition, Lee *et al*. created the porous SnO_2 layer by simultaneous progress of both an electrochemical deposition and ECEP with the Sn^{4+} source [114]. Since this considerable morphological change has a great influence on the performance of electronic devices, its potential and leverage have to be evaluated in the PSC field.

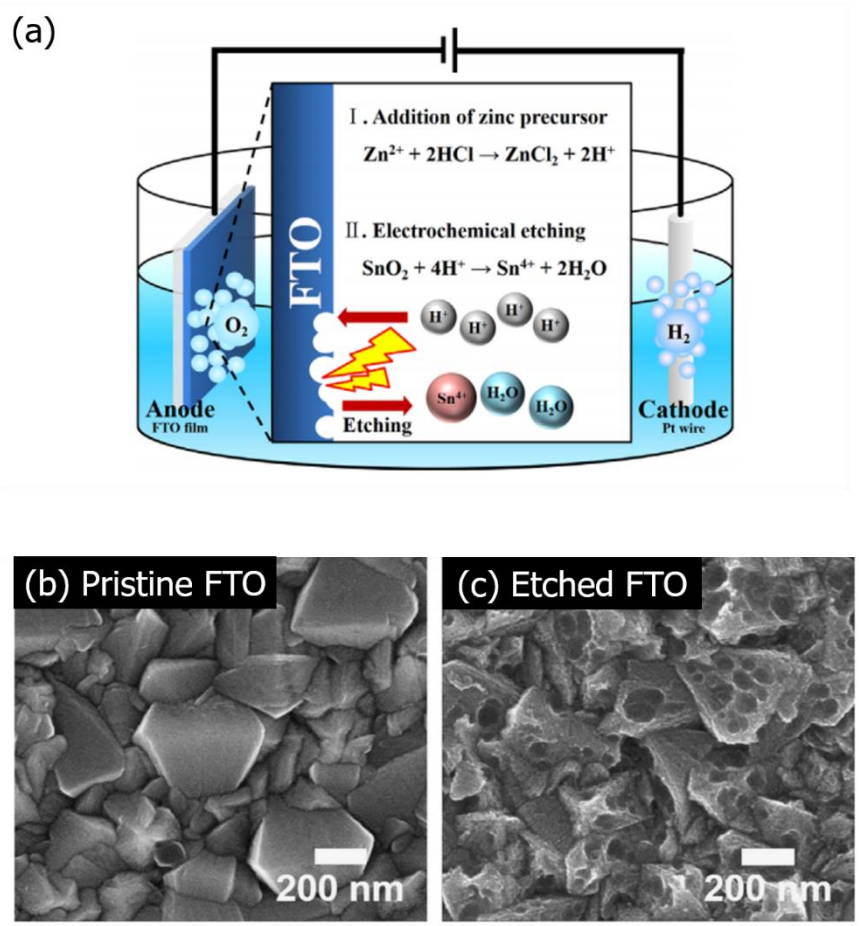

Figure 20. (a) Schematic diagram representing an electrochemical etching process and reaction mechanism. (b) FE-SEM images of surface morphology for (b) a pristine and (c) an electrochemically-etched FTO [113].

1.2. Objectives and Outlines

1.2.1. Objectives

The aim of this dissertation is not only to suggest a method for simplifying the fabrication process and structure of the planar PSC, but also to provide strategies for achieving high performance in the simplified PSC. In detail, a SnO_2 thin film (TF) is activated *via* only atmospheric Ar/O_2 plasma to realize genuine LT and superfast process, which is introduced into the planar PSC as the HBL and evaluated against electrical quality and PV efficiency. Subsequently, the simplified PSC is designed by completely removing the HBL, and evolution in performance, according to the change in perovskite grain size and surface morphology of FTO substrate, is systemically investigated to identify the optimized condition for the efficient HBL-free PSC. This study provides distinctive approaches from the structural and process perspectives to improve productivity, reproducibility, and economic feasibility of the PSC, which are pivotal factors for the commercialization of PSCs.

1.2.2. Outlines

This dissertation focused on not only simplifying the fabrication process and structure of PSC, but also devising the methods for

enhancing the performance of HBL-free PSC. This dissertation involves the following subtopics:

I. Atmospheric O_2 plasma-derived SnO_2 HBL-based PSC

II. Large-grained perovskite-based HBL-free PSCs

III. Hierachically porous FTO-based HBL-free PSCs

A detailed outline of the study is as follows:

1. Atmospheric Ar/O_2 plasma is employed as the key energy source for activation of sol-gel film and formulated a dense SnO_2 HBL (P-SnO_2) at an unimaginable rate within 5 min under the near room-temperature. The P-SnO_2 HBL has the close-packed M−O−M backbones playing a role as electron conductance pathways, which delivers superior electrical properties than those of the thermally annealed-SnO_2 (T-SnO_2) HBL.When introduced to PSCs, not only the average PCE improved from 17.65 % to 18.52 % with a champion PCE of 19.56 %, but also the gentler hysteresis is observed through rapid transient response by fast de-trapping of the accumulated charges at the P-SnO_2/perovskite interface.

Also, the P-SnO_2-based PSCs have a better photo-stability even after 6 h of light exposure, which is ascribed to the relieved charge accumulation. The time for oxidation of SnO_2 TF is remarkably shortened with an increase of O_2 flow rate (90 s under O_2 flow rate of 0.07 L/h), which indicates that the pace of process can be flexibly adjusted with calculating the profit and loss of fabrication cost.

2. HBL-free PSC is designed by removing the ordinary HBL from the planar PSC to not only simplify the structure and fabrication process, but also eliminate operation instability triggered by the HBL. Accordingly, a $MAPbI_3$ film was directly coated on blank FTO without the metal oxide-based HBL. Since perovskite itself plays a role as the HBL in parallel with sensitizer in this type of PSC, the thickness and grain size of perovskite are essential factors to obstruct the contact between HTM and FTO. PV performance of HBL-free PSC is estimated on the basis of $MAPbI_3$ grain size and thickness, which are controlled by the precursor concentration (37, 44, 51 and 58 wt%). All PV parameters are enhanced with increasing the grain size and thickness, and reached the saturated efficiency when the grain size and thickness of $MAPbI_3$ are larger than *ca.* 700 nm. Consequently, the HBL-free PSC exhibits a remarkable PCE

of 18.20 %, and the better light-stability, recyclability compared with TiO_2 HBL-inserted PSCs. Accordingly, the simple and efficient HBL-free PSCs are suitable to a commercial PV model in terms of economic and environmental values.

3. In this section, HBL-free PSCs are assembled based on a transformed FTO including a hierarchically porous structure at the surface, derived by ECEP on the commercially purchased FTO, to further improve the efficiency of HBL-free PSC and surmount the severe hysteresis problem occurred in the HBL-free PSC due to an unbalanced charge transfer rate. The interface area of FTO/perovskite is elevated approximately tenfold after this modification due to the creation of macro- and meso-pores at surface. Using the etched FTO (E-FTO), the average performance is enhanced from 16.80 to 17.61 %, which is originated from a drastic growth in the short-circuit current density (J_{sc}) by the expedited expulsion of unbound electrons in the perovskite due to an increased interface area between the perovskite and E-FTO. Furthermore, the severe hysteretic behavior of control PSCs is relieved in the E-FTO-based HBL-free PSC. Finally, the best PCE of 19.22 % of E-FTO-based

HBL-free PSC, achieved under optimal conditions, had J_{sc} of 22.81 mA/cm^2, V_{oc} of 1.123 V, and FF of 0.750.

2. Experimental Details

2.1. Atmospheric O_2 plasma-derived SnO_2 HBL-based PSCs

2.1.1. Preparation of SnO_2 thin films

An amorphous SnO_2 HBL was developed by a combination of sol-gel process and atmospheric Ar/O_2 plasma. First, anhydrous $SnCl_2$ was purchased from Alfa aesar. The $SnCl_2$ was dissolved in anhydrous ethanol with the concentration of 0.075 M. Secondly, the precursor was spin-coated with 4000 rpm on the O_2 plasma treated-FTO substrates, followed by annealing using thermal or atmospheric-pressure Ar/O_2 plasma energy, respectively. The T-SnO_2 HBLs were formed under the relatively harsh thermal-stress of 180 °C for 1 h. The plasma-annealed SnO_2 (P-SnO_2) HBLs were formulated by an atmospheric-pressure plasma equipment under various gas flow (especially O_2 flow) and time conditions with fixing plasma power to 180 W. The rate of O_2 flow was varied from 0.02 to 0.07 L/h at a fixed flow rate of Ar (0.008 L/h) to uncover that how much time for oxidation of SnO_2 HBLs could be saved. To avoid a dispute about a difference in spreadability of perovskite precursor on each HBLs, the T-SnO_2-based substrates were also plasma-

treated (O_2 of 0.07 L/h and Ar of 0.008 L/h) for 30 s before depositing a perovskite film.

2.1.2. Fabrication of SnO_2 HBL-based PSCs

FTO electrodes with a sheet resistance of 7 Ω/sq were purchased from Wooyang GMS. Cesium iodide (CsI, 99.999 % trace metals basis), Lead (II) bromide ($PbBr_2$, ≥ 98%), Acetonitrile (anhydrous, 99.8 %), *N,N*-dimethylformamide (DMF, anhydrous, 99.8 %), Dimethyl sulfoxide (DMSO, 99.9 %), Lithium bis(trifluoromethanesulfonyl)imide (Li-TFSI), and 4-tert-butylpyridine (4-tBP, 96 %) were purchased from Sigma-Aldrich. Lead (II) iodide (PbI_2, 99.9985 %, metals basis) and chlorobenzene (99 %) were purchased from Alfa aesar. The Formamidinium iodide (FAI, > 99.5 %) and 2,2′,7,7′-tetrakis (N,N-di-p-methoxyphenylamine)-9,9′-spirobifluorene (spiro-OMeTAD) were purchased from LUMTEC and Merck, respectively. MABr was synthesized through well-known method, reaction of methylamine (40% in methanol, Junsei chemical Co., Ltd) with hydrobromic acid. Patterning FTO glass was conducted using polyimide tape, followed by etching with 2 M hydrochloric acid (HCl) and Zn powder. The patterned FTO was rinsed in deionized (DI) water, acetone, and 2-propanol with

sonication, simultaneously. The two types of SnO_2 HBLs were coated on the rinsed FTO. As a role of light-harvesting layer, the cesium-doping mixed cation and halide perovskite ($Cs_{0.056}FA_{0.76}MA_{0.15}PbI_{2.42}Br_{0.48}$) was prepared in a mixed solvent of DMF and DMSO (4:1, *v:v*) as previously reported method. The FAI of 1 M, MABr of 0.02 M, CsI of 0.0075 M, PbI_2 of 1.1 M, and $PbBr_2$ of 0.22 M were blended in the mixed solvent, and the precursor solution was stirred at 50 °C for 1 h, and filtered with polytetrafluoroethylene (PTFE) syringe filter (0.45 μm pore-size). The aged precursor was dropped and consecutively spin-coated at two stages on the SnO_2 HBLs: the rate of 1000 rpm accelerated by 200 rpm/s was maintained for 5 s in the first stage, and the rate of 5000 rpm accelerated by 2000 rpm/s was retained for 23 s in the second stage. Chlorobenzene of 0.1 mL was dropped on the surface of SnO_2 HBL/FTO substrates rotating at a rate of 5000 rpm to quickly crystallize the perovskite, followed by annealing at 100 °C for 20 min under ambient air (30 % relative humidity (RH), 25 °C). Subsequently, spiro-OMeTAD solution in chlorobenzene of 0.7 mL, which was composed of 50.6 mg of spiro-OMeTAD, 20.16 μL of 4-*tert*-butyl pyridine (4-*t*BP), and 12.3 μL of lithium bis(trifluoromethanesulfonyl)imide (Li-TFSI) solution (520 mg in 1 mL of anhydrous acetonitrile), was spin-coated as the HTL on the

annealed perovskite at 2000 rpm for 30 s. Finally, a gold (Au) electrode was deposited with 60 nm thickness onto the HTL by thermal evaporation at a rate of 0.05 nm/s.

2.1.3. Characterization of the SnO_2 HBL and PSCs

Atmospheric plasma oxidation was conducted using MyPL-200 with frequency of 13.56 MHz purchased from Atmospheric Process Plasma Corp. X-ray photoelectron spectroscopy (XPS) analysis were carried out with an AXIS-His (Kratos). Surface morphologies and atomic of various films was obtained from a field-emission scanning electron microscope (FE-SEM, JEOL-6700, JEOL) equipped with an energy dispersive spectroscopy (EDS) spectrometer (Inca). Atomic force microscopy (AFM) analysis was carried out with Innova SPM (Veeco, USA) and SPMLabAnalysis software. PV performance was measured under AM 1.5 solar irradiance with 530 W xenon lamp and intensity of 100 mW/cm^2 (XIL Model 05A50KS source units). Tafel and current density-voltage (*J-V*) plots of the electron-only devices, open-circuit voltage decay (OCVD), and electrochemical impedance spectroscopy (EIS) were characterized by Zahner Electrik IM6 analyzer (Zahner Electrik GmbH & Co., KG, Kronach, Germany). Mott-Gurney law equation was employed to calculate the electron mobility. The equation is below:

$$J = \frac{9}{8}\mu\varepsilon_0\varepsilon_r\frac{V^2}{L^3}$$

μ: electron mobility

ε_0: free space permittivity

ε_r: dielectric constant

L: film thickness

The conductivity (σ_0) of SnO_2 TF was calculated by extracting the slopes from *I-V* curves with an equation, $I = \sigma_0 A d^{-1} V$ as a previous report [115]. IPCE spectra was characterized from 300–850 nm (PV Measurements, Boulder, CO, USA) under a short-circuit current. XRD measurements were conducted using M18XHF–SRA (Mac Science, Buffalo, NY, USA) using a Cu Kα radiation source (λ = 1.5406 Å) at 40 kV and 300 mA (12 W). UV–Vis absorbance, and transmittance spectra were investigated by a spectrophotometer (Shimadzu UV-3600 Plus). Time-resolved photoluminescence (TRPL) spectra was recorded under exposure to 520 nm pulse laser (PicoQuant). The ultraviolet photoelectron spectroscopy (UPS) spectra was measured by Axis Supra (Kratos) with a minimum step size of 1 meV and sensitivity of 1,000,000 cps at 120 meV resolution. The typical femtosecond-transient absorption (FS-TA) spectroscopy was conducted to obtain transient absorption temporal profiles. The light source was regeneratively-amplified

Ti:Sapphire laser (Spectra-Physics) with 0.60 mJ/pulse of output power, 130 fs pulse width, 1 kHz repetition rate at 800 nm. The probe pulse which was a continuum light, was generated by focusing 800 nm light into a sapphire plate (Thorlabs) and detected with photodiodes (New Focus) after a monochromator (250 IS/SM, Chromex).

2.2. Large-grained perovskite-based HBL-free PSCs

2.2.1. Fabrication of HBL-free PSCs and large grain perovskite

FTO glass with a sheet resistance of 7 Ω/sq was purchased from Wooyang GMS, Korea. These were patterned using polyimide tape and etched with 2 M aqueous HCl solution and Zn powder (Junsei chemical Cogk, Ltd.). To rinse the substrates, Hellmanex™ III (Sigma-aldrich) of 2 vol % aqueous-solution, acetone, and 2-propanol were used, respectively. Atmospheric-pressure Ar/O_2 plasma (180 W, 0.02/0.008 L/h) was treated on the FTO glass for 10 min to enhance solution wettability and remove organic contamination. In case of the HBL-free PSC, a perovskite film was directly deposited on the FTO substrate without any additional interlayers or treatments. For the TiO_2 HBL-inserted PSCs, a mildly acidic solution of titanium isopropoxide (TTIP) in ethanol (TTIP of 1 mL and HCl (35 wt% in H_2O) of 0.15 mL in ethanol

of 14.5 mL) was spin-coated at 3000 rpm for 60 s and annealed at 450 ºC for 30 min. The $MAPbI_3$ precursor was obtained by mixing PbI_2 (461 mg) with MAI (159 mg) at 1:1 molar ratio in anhydrous DMF. The MAI was synthesized by reacting methylamine (40 wt% in water) with hydroiodic acid (57 wt% in water) in the ice bath for 2 h with constant stirring. After the reaction, the MAI was precipitated by eliminating the solvent through rotary evaporation. The precipitation was washed with diethyl ether (three times) and the white powder of MAI was obtained with vacuum drying. To prepare a $MAI{\cdot}PbI_2{\cdot}DMSO$ adduct film, 72 µL of DMSO was added in the precursor solution, and stirred at room temperature for 2 h, followed filtering with PTFE syringe filter with 0.45 µm pore-size. Consecutive spin-coating processes with two stages were employed to form perovskite layer: The first (1000 rpm accelerated by 200 rpm/s) and second stages (4000 rpm accelerated by 2000 rpm/s) were maintained for 10 s and 23 s, respectively. During the second stage, diethyl ether of 0.1 mL was dropped on the substrate to crystallize the $MAPbI_3$. The resulting films were annealed at room-temperature for 3 min, 60 °C for 5 min and 100 °C for 1 h to obtain high crystalline perovskite film. To obtain large-grain-based perovskite film, solvent-annealing (SA) was introduced; the perovskite film was covered by petri

dish when the films were annealed at 100 °C, followed by inserting 5 µL of DMSO in edge of the petri dish. Subsequently, the HTM was prepared by dissolving spiro-OMeTAD of 50.6 mg in chlorobenzene of 0.7 mL, which was doped with 20.16 µL of 4-*t*BP, and 12.3 µL of Li-TFSI solution (520 mg in 1 mL of acetonitrile). The 10 µL of spiro-OMeTAD solution was spin-coated at 3000 rpm for 30 s. Finally, gold was deposited on the HTM layer with 60 nm thickness by thermal evaporation at the rate of 0.06 nm/s. A typical active area of the cell was 0.105 cm^2 as defined by shadow mask.

2.2.2. Characterization of the fabricated perovskite and PSCs

Atmospheric Ar/O_2 plasma equipment (MyPL-200) was purchased from Atmospheric Process Plasma Corp. and conducted using with frequency of 13.56 MHz. Both the surface of $MAPbI_3$ and device cross-sectional morphologies were obtained from the FE-SEM (JEOL-6700, JEOL). Surface roughness was analyzed by the AFM (Innova SPM, Veeco, USA) with SPM LabAnalysis software. The SPO, and nyquist plots were obtained from Zahner Electrik IM6 analyzer (Zahner Electrik GmbH & Co., KG, Kronach, Germany). The power output was calculated by the following relation: PCE = [J (mA/cm^2) × V (V) / (100 mW/cm^2)]. PV

performance was measured under AM 1.5 solar irradiance with 530 W xenon lamp and intensity of 100 mW/cm^2 (XIL Model 05A50KS source units). IPCE was measured by K3100 of McScience under a short-circuit current. XRD were conducted using an SmartLab (Rigaku) with a Cu Kα radiation source (λ = 1.5406 Å) at 40 kV and 300 mA (12 W). UV–Vis absorbance spectra was investigated by spectrophotometer (V-770, JASCO) with Spectra Manager™ software. TRPL measurement were carried out using a TRPL board (SPC-150, Becker &Hickl) with 48.9 ps time channel. 405 nm picosecond-pulsed diode laser (LDH-P-C-405, Picoquant) was used for irradiation and the luminescence of perovskite was extracted by 542 nm longpass filter. The perovskite films were scanned by piezo stage (NanoMax-TS, Thorlabs).

2.3. Hierachically porous FTO-based HBL-free PSCs

2.3.1. Preparation of the hierachically porous FTO substrate

Pristine FTO (P-FTO) having a sheet resistance of 7 Ω/sq (Pilkington, TEC-15) was patterned by polyimide tape and etched with 1 M hydrochloric acid and Zn powder, followed by washing with DI- water, acetone, and 2-propanol. The hierarchically porous FTO (etched FTO, E-FTO) was prepared by ECEP of the patterned FTO using a method similar to that previously reported [113, 114]; the etching was conducted in potentiostat mode with two electrodes consisting of Pt wire and the commercial FTO substrate as the anode and cathode, respectively. The electrolyte used for the etching was the solution of 0.01 M $Zn(O_2CCH_3)_2$ (zinc acetate, anhydrous) in 1 M HCl solution. The separation distance between the anode and cathode was *ca*. 5 cm and the etching process was operated at fixed voltage of 4 V for different processing times. **Figure 21** shows digital images of the actual electrode configuration for etching process. In **Figure 21a**, the etching bath is composed of cathode, anode and reference electrode, and Pt and FTO are connected to anode and cathode, respectively. The detailed internal view of the etching bath can be seen in **Figure 21b**. When the electrochemical etching process was conducted, the patterned FTO glasses (by Zn and HCl) were used as

shown in **Figure 22a**, where the active area (*A*) for ECEP was 1.05 cm^2 (1.5 cm × 0.75 cm, sky-blue color). The charge density (charge per unit area) during etching process is shown in **Figure 22b**, which was measured at optimized etching condition (4V, 15 min). The ECEP proceeded at a high rate during the first 3 min, and then conducted slowly. The first stage of ECEP (vigorous region) produced macro pores at surface of FTO mainly, and more small pores were created in the mild stage. It is crucial to keep the current density below 90 mA/cm^2 during ECEP. When the bias voltage of 4 V is exceeded, the charge densities on FTO will be extremely high and it is difficult to control the surface structure. That is, when applying a voltage of 3 ~ 4 V, the FTO surface etching is performed at a controllable rate. Lastly, the completed E-FTO was rinsed with DI water, acetone, and 2-propanol in preparation for PSC fabrication.

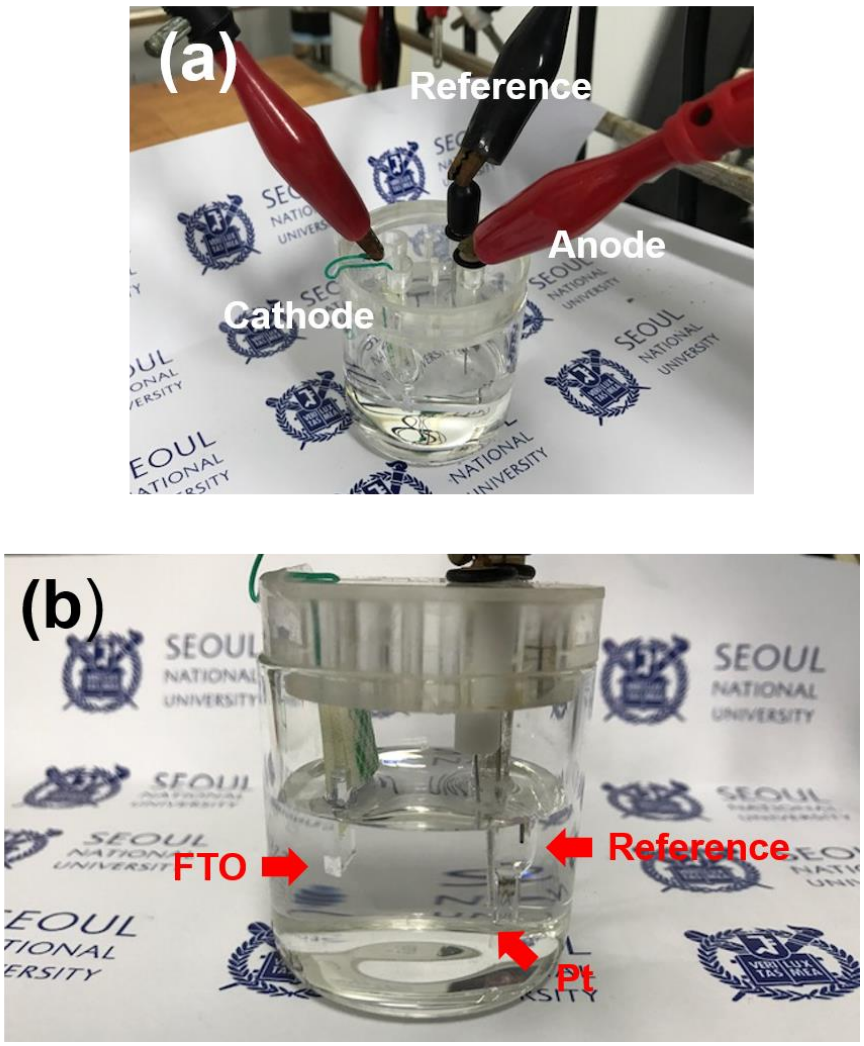

Figure 21. (a) Digital image of the electrochemical etching system based on three electrodes and (b) detailed internal view.

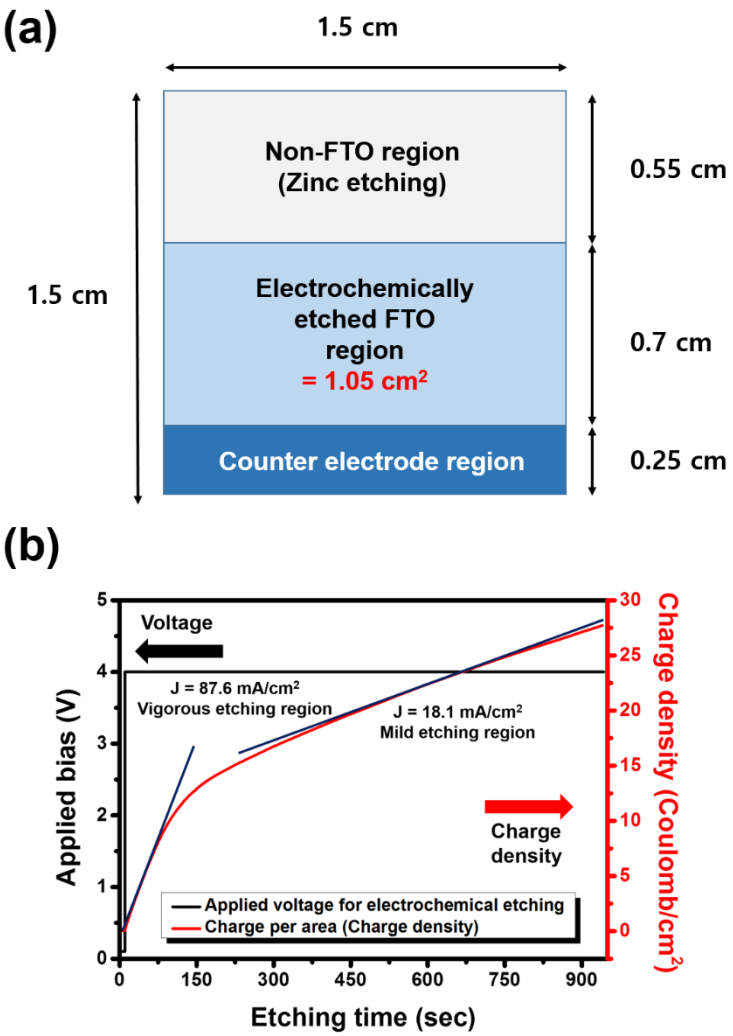

Figure 22. (a) The *A* for ECEP with the prepared FTO glass, and (b) the variation of charge density during ECEP.

2.3.2. Fabrication of the hierachically porous FTO-based PSCs

Atmospheric Ar/O_2 plasma were treated on FTO substrates for 3 min to remove carbon contaminants and to enhance surface wettability. The perovskite precursor was prepared by mixing PbI_2 (461 mg) with MAI (159 mg) at 1:1 molar ratio in anhydrous DMF. To prepare a $MAI{\cdot}PbI_2{\cdot}DMSO$ adduct film, 72 μL of DMSO was added to the precursor solution, which was stirred at room temperature for 2 h [84]. The perovskite precursor was spin-coated on the blank FTO glass (P- and E-FTO) by consecutive spin-coating at two rates: the first stage at 1000 rpm for 10 s with an acceleration of 200 rpm/s and the second stage at 4000 rpm for 30 s with an acceleration of 3000 rpm/s. During the second stage, diethyl ether (80 μL) was dripped onto the substrates, which produced the $MAI{\cdot}PbI_2{\cdot}DMSO$ intermediate films. Annealing at room temperature for 3 min, 60°C for 5 min, and 100°C for 1 h, created a highly crystalline perovskite film. Then, the SA process was carried out to enlarge the perovskite grains [99]. The HTL was then deposited on the annealed perovskite by spin-coating 10 μL of spiro-OMeTAD solution at 3000 rpm for 30 s. The spiro-OMeTAD solution was composed of 50.6 mg of spiro-OMeTAD dissolved in 0.7 mL of chlorobenzene, 12.3 μL of Li-TFSI solution (520 mg in 1 mL of anhydrous acetonitrile), and 20.16

μL of 4-*t*BP. Finally, 60-nm-thick Au coating was deposited onto the HTL by thermal evaporation at a rate of 0.06 nm/s. The *A* of the PSC was typically *ca.* 0.105 cm^2, as defined by a shadow mask.

2.3.3. Determination of roughness factor of the FTO substrate

The D719 dye (2.524×10^{-4} M in ethanol) solution was prepared to conduct dye absorption process. Each FTO was immersed in ethanol-based dye solution and kept at room temperature for 24 h. After dyeing, the FTO substrates were rinsed with distilled water and dried at 80 °C oven for 20 min. For desorption of dye-molecule, the FTO substrates were immersed in 5 mL of 0.01 M NaOH solution, followed by measuring the ultraviolet-visible (UV-Vis) light absorbance of the dye. The *Beer−Lambert law* was used to determine the number of moles of dye adsorbed on the FTO.

Beer-Lambert law

$$A = \varepsilon \cdot b \cdot C \ (C = A / \varepsilon \cdot b)$$

ε : absorptivity [L/g·cm] or [mol·cm]

b : path length [cm]

C : concentration [mol/L]

The absorptivity of N719 dye is 1.47×104 $L \cdot mol^{-1} \cdot cm^{-1}$ at 535 nm in

literature [116], and path length of cuvette is 1 cm. Each D719 molecule occupies a surface area of 1.65 nm [117, 118]. The real surface area was measured by multiplying the surface area of dye molecule with the number of desorbed dye molecules. The geometric surface area (projected area) was 5 cm^2 (5×10^{-4} m^2). Roughness factor (*RF*) of two samples can be calculated from the following formula.

$$RF = \text{Real surface area / Geometric surface area}$$

2.3.4. Characterization of the fabricated FTO and PSCs

J−*V* curves of the P- and E-FTO based PSCs were estimated by 530 W xenon lamp under AM 1.5 solar irradiance with intensity of 100 mW/cm^2 (XIL Model 05A50KS source units). The IPCE spectra was obtained from 300–850 nm (PV Measurements, Boulder, CO, USA) under short-circuit current. The FE-SEM images were obtained from JEOL 6700 instrument. The XRD patterns were characterized by an M18XHF–SRA instrument (Mac Science, Buffalo, NY, USA) using Cu Kα radiation source (λ = 1.5406 Å) at 40 kV and 300 mA (12 W). Water contact angle measurement was confirmed by SDLab-200TEZD goniometer (Femtofab, Korea). UV–Vis absorbance, transmittance, and diffuse reflectance spectras were characterized by Lambda–35 spectrometer

(Perkin–Elmer, Waltham, MA, USA). EIS characteristics (nyquist plot) were measured by Zahner Electrik IM6 analyzer (Zahner Electrik GmbH & Co., KG, Kronach, Germany), which was conducted under light illumination of 100 mW/cm^2 or in the dark. TRPL was measured by using 405 nm pulse laser (PicoQuant). The UPS spectra was measured by PHI 5000 VersaProbe (ULVAC PHI, Japan) with the monochromatized Al Kα source

3. Results and Discussion

3.1. Atmospheric Ar/O_2 plasma-derived SnO_2 HBL-based PSCs

3.1.1. Preparation of SnO_2 HBL *via* atmospheric Ar/O_2 plasma

Amorphous SnO_2 TFs employed for the HBL of PSCs were prepared by spin-coating of anhydrous $SnCl_2$ solution (0.075 M in absolute etahnol), followed by annealing with thermal or Ar/O_2 plasma energy (T- and P-SnO_2), as illustrated in **Figure 23**. The T-SnO_2 TF was sluggishly developed by a heat stress of 180 ºC for 1 h, similar to the method used in previous work [29], whereas the P-SnO_2 TF formed instantaneously within 5 min by atmospheric Ar/O_2 plasma (0.008/0.06 L/h) with a fixed power of 180 W and unintentional heating (*ca*. 50 ºC) accompanied by plasma ion bombardment **(Figure 24).** Even if inevitable thermal energy is partially involved, the degree of oxidation is mainly ruled out by the exposure time and O_2 flow rate. When the treatment time and power were fixed, the rate of oxidation was proportional to the O_2 flow rate (0.02 – 0.07 L/h), and the required annealing time for the full oxidation of SnO_2 TFs was dramatically reduced from 450 to 90 s with increasing the O_2 flow rate from 0.02 to 0.07 L/h, which was mediately judged by the P-SnO_2-based PSCs (P-PSCs) performance results.

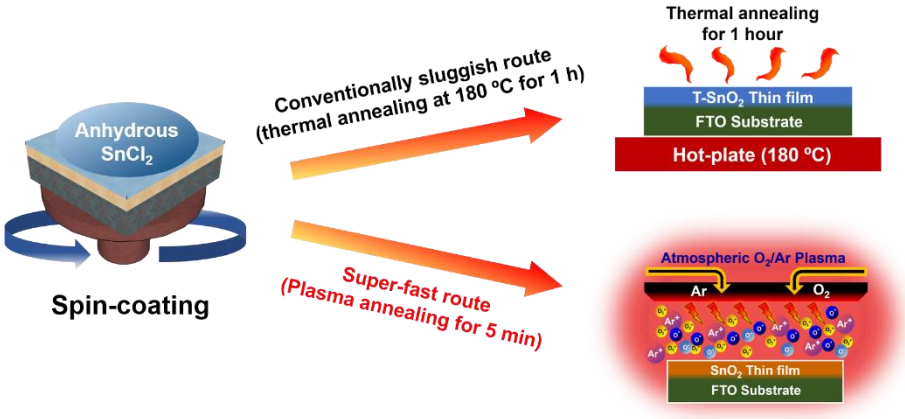

Figure 23. Schematic diagram of the deposition and oxidation processes of SnO_2 TFs *via* the conventionally thermal route or superfast Ar/O_2 plasma approach.

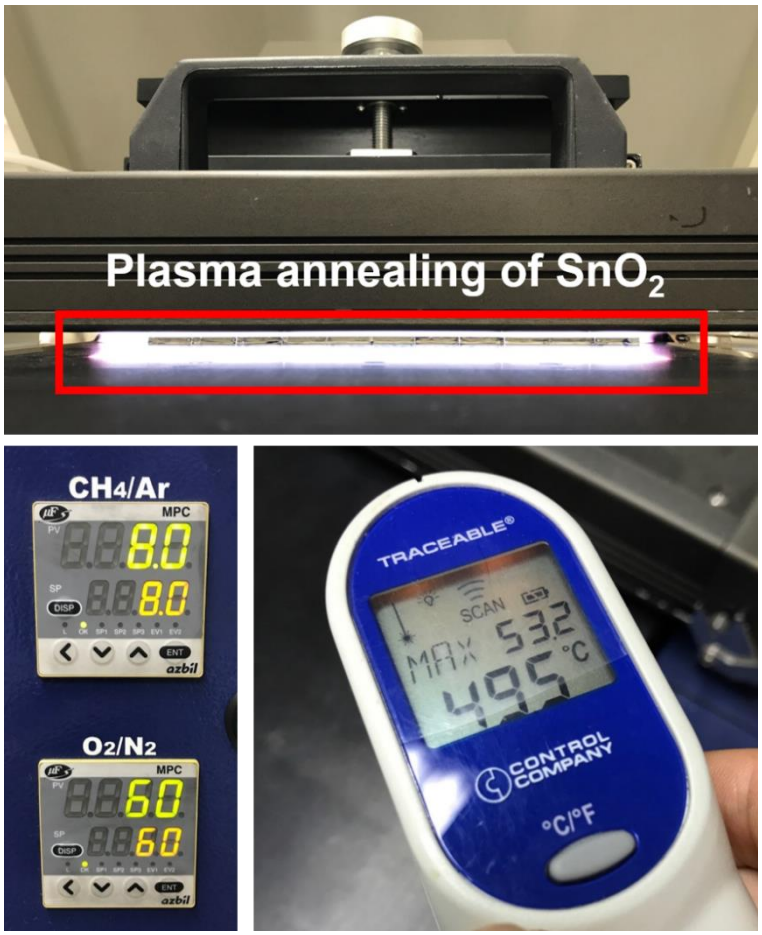

Figure 24. Digital image of plasma oxidation process to fabricate P-SnO_2 TF. The FTO substrates exposed to Ar/O_2 plasma are distinguished by a rectangular red-line. At the right of this, the real image showing the extent of gas flow and unintentional plate heating by plasma were displayed.

3.1.2. Physicochemical and electrical analysis of SnO_2 thin films

The surficial morphologies of two types of SnO_2 TFs were confirmed by FE-SEM as displayed in **Figure 25**. The SnO_2 TFs oxidated by thermal and plasma energy have *ca.* 15 nm thickness with an amorphous phase in both T- and P-cases, which was verified by XRD and spectroscopic ellipsometry **(Figure 26)**. There was no clear distinction in the atomic ratio between Sn and O as characterized by EDS **(Figure 27)**, which is parallel with the result obtained by XPS analysis in **Table 1**. Also, the optical transmittances of T- and P-SnO_2 TFs were analogous over the entire wavelength range, without opacification by metallic reduction **(Figure 28)**, and the band-gap (E_g) of 4.02 eV was observed in both T- and P-SnO_2 TFs **(Figure 29).** Furthermore, the negligible difference was observed in a root-mean-square (*RMS*) roughness and average roughness values of each SnO_2 TF, measured over three line profiles by AFM images **(Figure 30)**.

XPS analysis was carried out to determine the surface chemical states of the SnO_2 TFs and its survey spectra is displayed in **Figure 31**. The characteristic peaks of Sn^{4+} $3d_{5/2}$ and Sn^{4+} $3d_{3/2}$ (488.0 and 496.5 eV) were identically recorded in T- and P-SnO_2 TFs without shift, and O 1s peaks were clearly observed at 531.4 eV, which roughly suggests that the

pure SnO_2 TFs formed regardless of the annealing method. To better understand the difference in chemical bonding of the two films, the O 1s peaks were deconvolved from the two spectra, where the individual peaks at lower and higher binding energies were originated from the lattice oxygen atoms in the fully coordinated environment (M-O-M) [119, 120], and the hydroxide species (M-OH), respectively [121, 122]. The peak of M−O−M backbones, serving as electron conductance pathways [123], were more prominent in P-SnO_2 than T-SnO_2, and the peak corresponding to M-OH, playing a role as shallow trap sites [124], was slightly weak in the P-SnO_2 TF. It can be seen numerically that hydroxyl fraction is much more diminished in P-SnO_2 TF compared to T-SnO_2 TF. The extensive presence of M-OH is due to incomplete oxidation of the oxide lattice [119], which decreases the mobility of SnO_2 TF and hinders electron transport [121]. Accordingly, the highly densified oxide film was formed with lower impurity levels *via* the PA and noticeable improvement in electrical conductivity of P-SnO_2 TF was observed from Tafel and corresponding *J-V* plots **(Figure 32a)**, and average conductivity was calculated as $1.01 \pm 0.137 \times 10^{-4}$ and $2.43 \pm 0.196 \times 10^{-4}$ for T- and P-SnO_2, respectively **(Table 2)**. In addition, the P-SnO_2 yielded a higher mobility of 6.78×10^{-7} $cm^2/V{\cdot}s$ compared with T-SnO_2

having a mobility of 5.12×10^{-7} $cm^2/V \cdot s$ **(Figure 32b)**. Furthermore, the electron trap density (N_t) decreased by PA route from 1.03×10^{-18} cm^{-3} (T-SnO_2) to 5.25×10^{-17} cm^{-3} (P-SnO_2) **(Figure 33),** which guarantees rapid separation of photo-excited electrons when the perovskite is integrated, and relaxed hysteresis during PSC operation [125, 126]. In this case, TA probably induces more GBs due to active necking between SnO_2 interparticles, in which a large density of shallow trap sites may be formed due to lattice mismatch [127].

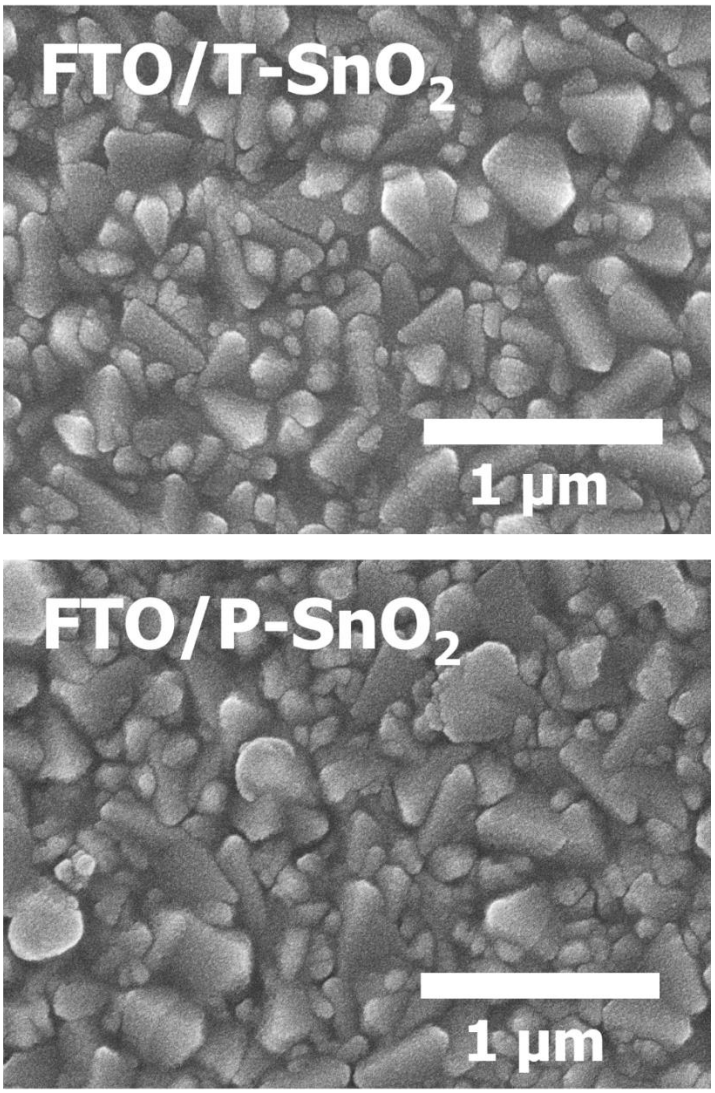

Figure 25. Surface FE-SEM images of the of SnO_2 TFs activated by thermal and plasma energy.

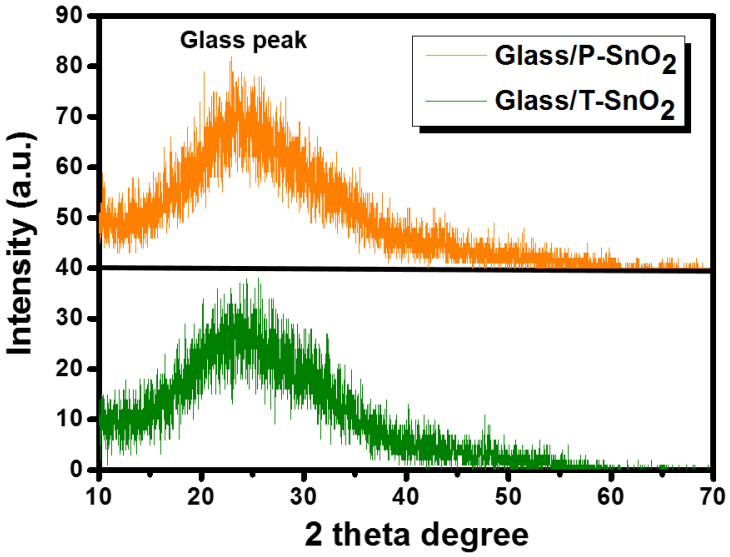

Figure 26. XRD patterns of FTO glass/T- and P-SnO_2 TFs. The result reveals the amorphous phase of SnO_2.

(a)

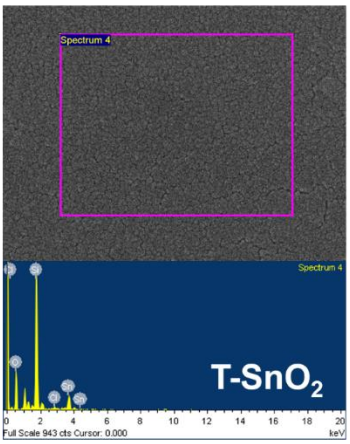

(b)

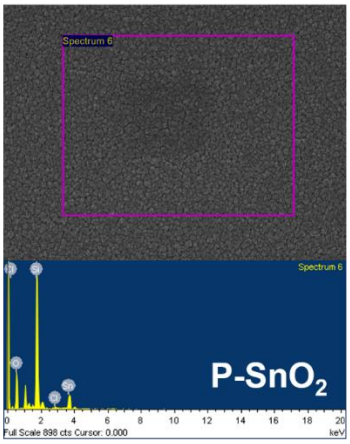

(c)

Element	T-SnO_2 (Atomic%)	P-SnO_2 (Atomic%)
O	68.65	67.70
Si	29.69	30.62
Cl	0.25	0.11
Sn	1.41	1.57
Totals	100.00	100.00

Figure 27. EDS results of (a) T-SnO_2 and (b) P-SnO_2 TFs formed on the bare glass. (c) Summarizing the element composition in each SnO_2 TF by atomic percentage.

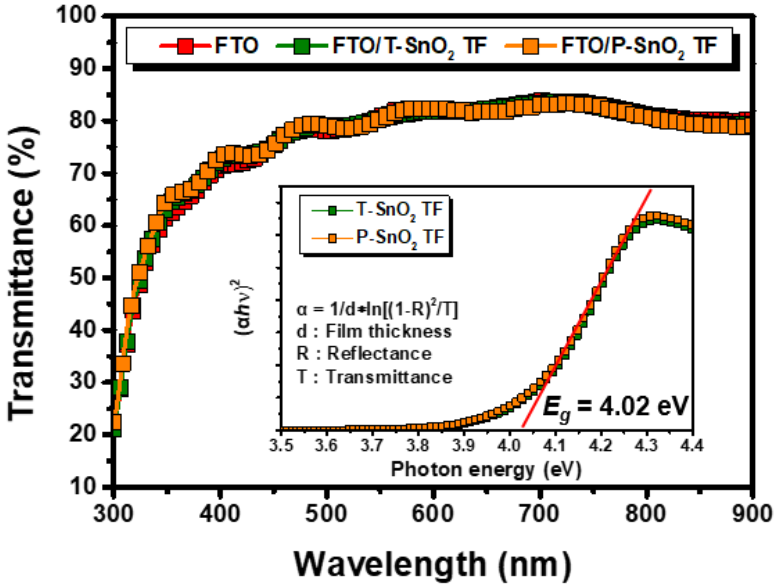

Figure 28. Transmittance spectra of FTO glass and two types of SnO_2 TFs deposited on FTO glass, and the E_g, computed by Tauc-plot (inset graph). The Tauc-plot was drawn by combining the reflectance and transmittance spectra of T-and P-SnO_2 TFs coated on quartz glass. The E_g of 4.02 eV was determined by extrapolating the linear portion of the plot.

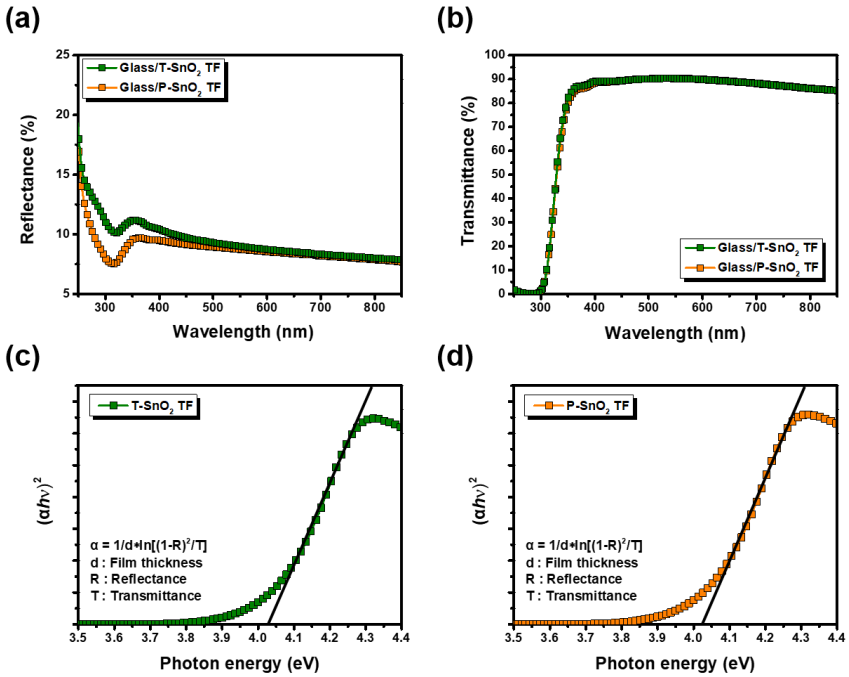

Figure 29. UV-Vis (a) reflectance and (b) transmittance spectra of T- and P-SnO_2 TFs coated on quartz glass. Tauc-plot of (c) T- and (d) P-SnO_2 TF extracted from the glass based-reflectance and transmittance spectra.

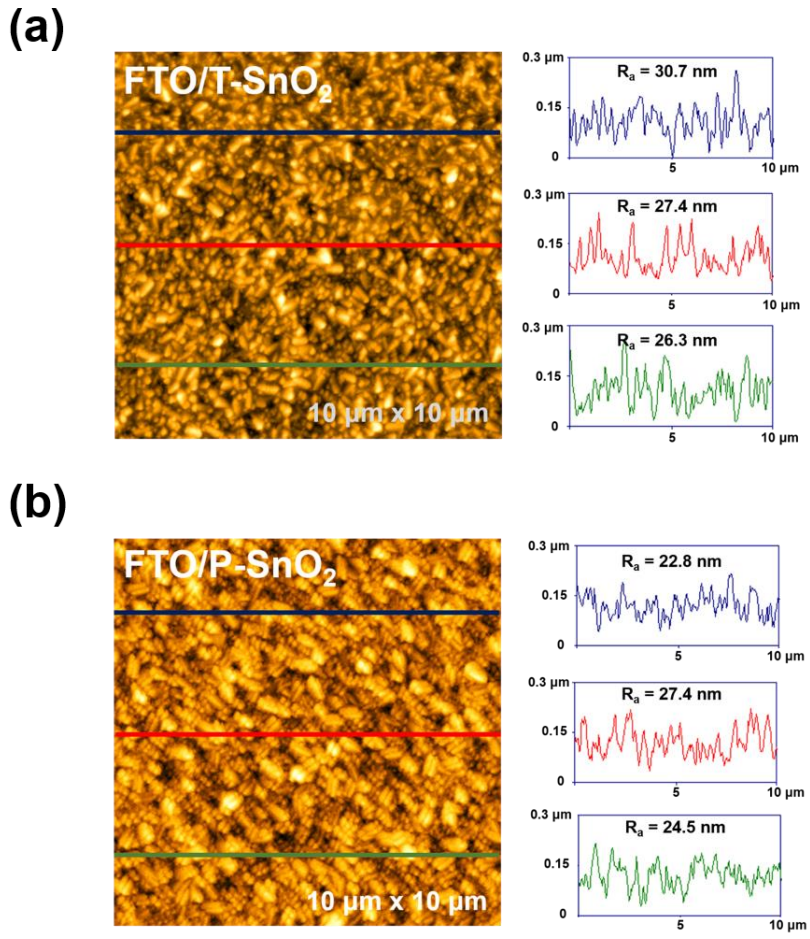

Figure 30. Two-dimensional AFM images of the SnO_2 TFs on FTO glass prepared by (a) the TA at 180 ºC for 60 min and (b) PA with Ar/ O_2 flow of 0.008/0.06 L/h for 5 min. The roughness was analyzed by line profile measurement at three different regions.

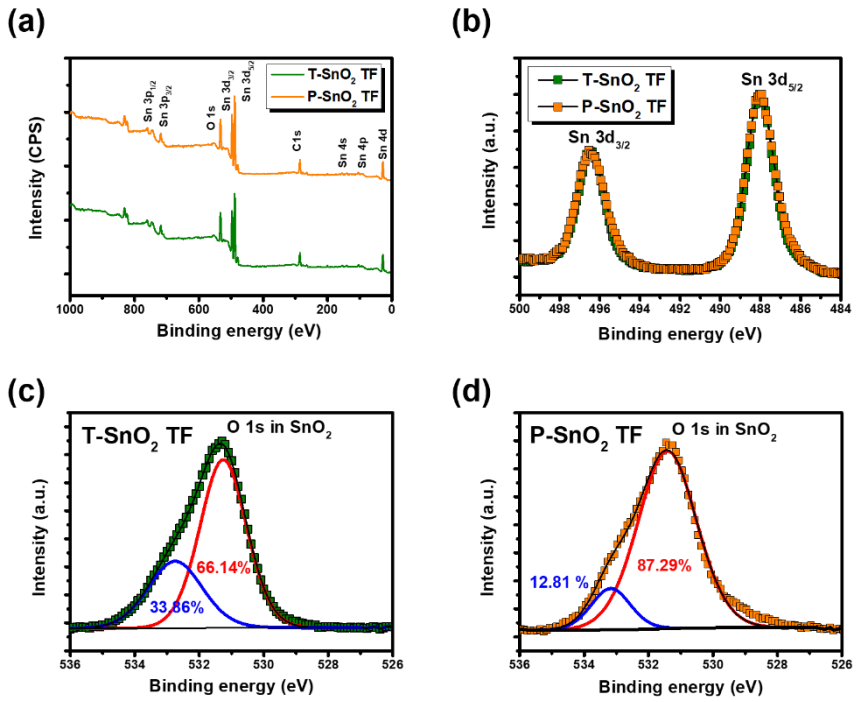

Figure 31. (a) XPS survey spectra of SnO_2 TFs activated by thermal and plasma routes. (b) Sn 3d peaks of two SnO_2 TFs and O_2 1s peaks for (c) T-SnO_2 and (d) P-SnO_2 TFs.

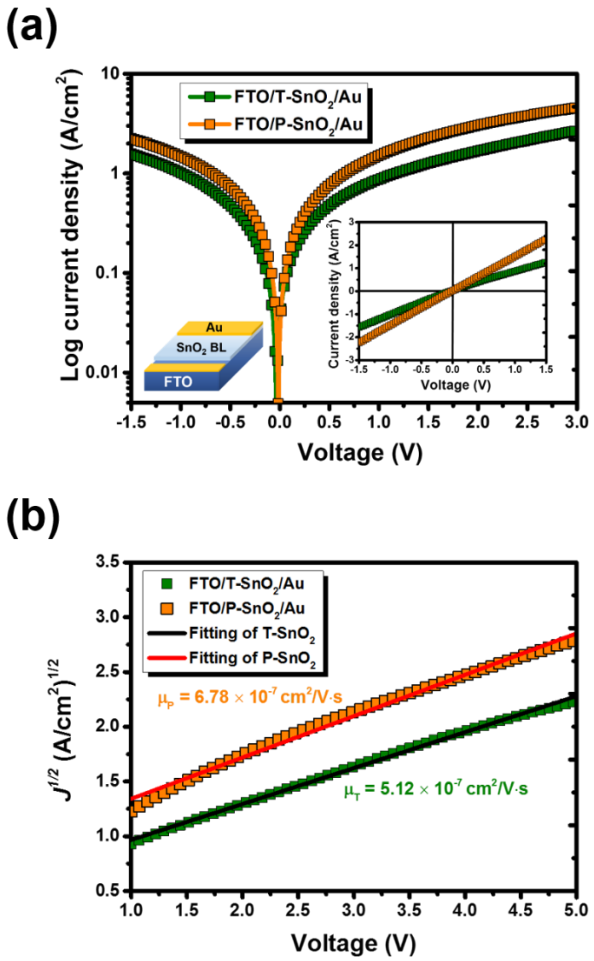

Figure 32. (a) Tafel plot and corresponding *J–V* curves (inset) of the FTO/T-SnO_2 or P-SnO_2/Au devices measured under dark conditions to analyze the vertical conductivity (b). $J^{1/2}$–*V* curves, plotted *via* the Mott–Gurney law [81], to calculate the SCLC electron mobility (μ) based on the structure of FTO/T- of P-SnO_2/Au devices.

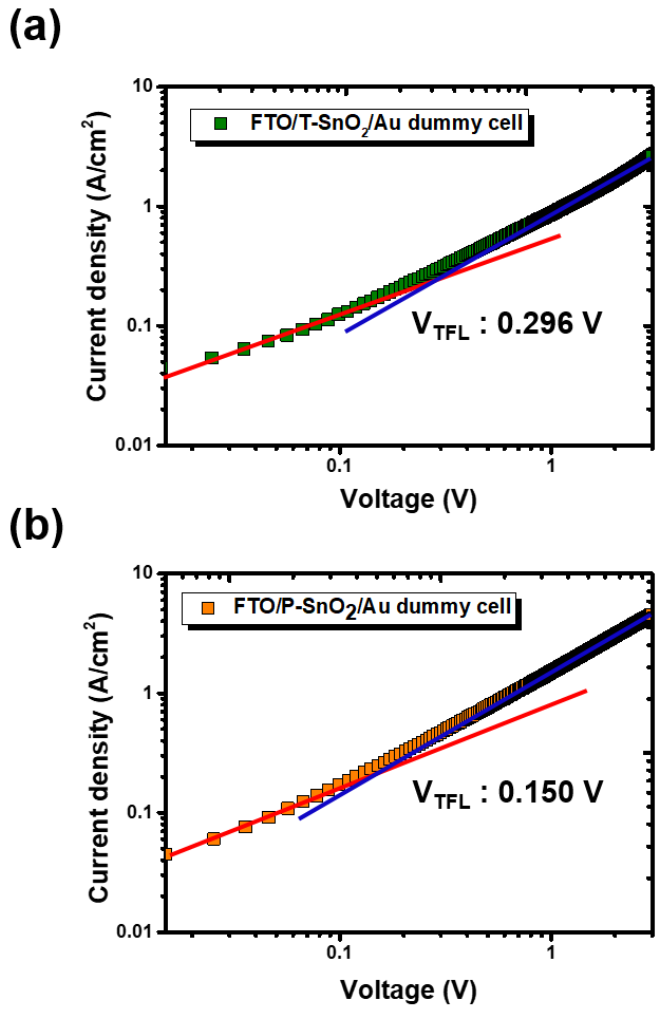

Figure 33. Dark *J-V* curves of FTO/(a) T- and (b) P-SnO_2/Au dummy cells for exploring the V_{TFL} kink point.

Table 1. Composition ratio of each element in the T- and P-SnO_2 TFs calculated from XPS analysis.

Element	T-SnO_2 (%)	P-SnO_2 (%)
Sn 3d	60.81	57.99
O 1s	19.41	21.13
Cl 2p	2.25	2.93
C 1s	17.53	17.94

Table 2. Conductivity of four SnO2 TFs annealed by thermal and plasma routes. Conductivity (σ_0) was calculated from equation, $I = \sigma_0 A d^{-1} V$.

	Conductivity (σ_0, S/cm)	**Average σ_0 (S/cm)**
Thermal 1	9.926×10^{-5}	$(1.01 \pm 0.137) \times 10^{-4}$
Thermal 2	9.674×10^{-5}	
Thermal 3	1.235×10^{-4}	
Thermal 4	8.584×10^{-4}	
Plasma 1	2.238×10^{-4}	$(2.43 \pm 0.196) \times 10^{-4}$
Plamsa 2	2.314×10^{-4}	
Plasma 3	2.752×10^{-4}	
Plasma 4	2.414×10^{-4}	

σ_0 : Conductivity (S/cm)

A : Active area

d : Thickness of sample

3.1.3. Photovoltaic performance of the P-SnO_2 HBL-based PSCs

Successful formulation of highly uniform and conductive P-SnO_2 TFs in the short time frame motivates their use as HBLs in PSCs. The PSC architecture and its side view are depicted in **Figure 34a** and **34b** with the energy band diagram, where the $Cs_{0.056}FA_{0.76}MA_{0.15}PbI_{2.42}Br_{0.48}$ perovskite with *ca.* 650 nm thickness was spin-coated onto SnO_2 HBLs **(Figure 35)** [19], followed by vertically stacking spiro-OMeTAD and Au in sequence as a HTM and cathode, respectively. The band alignment between SnO_2 HBL and perovskite was determined by UPS analysis **(Figure 36)** [128]. There was no obvious difference in crystallinity and light harvesting ability of perovskite with respect to the type of SnO_2 HBL **(Figure 37 and 38)**.

To evaluate PV performance based on the oxidization paths of the SnO_2 HBL, we examined the full-fledged condition of PSCs by manipulating the O_2 flow rate and plasma exposure time under fixed power and Ar flow rate at 180 W and 0.008 L/h, respectively. Performance was first investigated with respect to the plasma exposure time from 15 to 600 s at a fixed O_2 gas flow of 0.02 L/h **(Figure 39, Table 3)**. Under the mild O_2 flow, the maximized performance (MP) of the P-PSC was observed after an exposure time of *ca.* 450 s, which may

mirror the complete oxidation of the P-SnO_2 TF after 450 s. In the semi-oxidized state of the SnO_2 TF (< 450 s), residual Sn^{2+} and Cl^- ions may be incorporated into the perovskite lattice, spoiling the performance of P-PSCs because the Sn^{2+} ions oxidize readily under ambient air [129]. To further shorten the duration, the amount of O_2 flow increased from 0.02 to 0.07 L/h with a fixed exposure time of 300 s, obtaining the MP of P-PSCs above the O_2 flow rate of 0.06 L/h **(Figure 40, Table 4)**, which indicates that the time required for absolute oxidation can be further diminished to less than 300 s using a more powerful supply of O_2 plasma. As expected, only 90 s was enough to achieve MP with an O_2 flow rate of 0.07 L/h **(Figure 41)**. From these results, it is deduced that the time for preparing the fully oxidized SnO_2 TF by plasma is somewhat flexible according to the processing environment, such as the extent of gas flow and power of the system; nevertheless, PA can reduce considerably the overall processing time. In the case of T-SnO_2-based PSCs (T-PSCs), it was found that the TA time of at least 45 min at 180 ºC was required to achieve the MP as shown in **Figure 42**.

Based on one of the optimal conditions (O_2 of 0.06 L/h for 300 s), the comparison between T- and P-PSCs was conducted by measuring the typical *J-V* characteristics **(Figure 43)**. Surprisingly, beyond a similar

level, using PA improved the PCE from 17.46 to 18.64 % in J_{sc} and V_{oc}. To verify the reliability, the statistical PV metrics and PCE histogram were checked from 26 T- and P-PSCs as displayed in **Figure 43b**, **Figure 44**, and **Table 5**; the average J_{sc} increased from 20.66 ± 0.259 to 21.36 ± 0.415 mA/cm^2. This was consistent with IPCE results for the two cells **(Figure 45a)**, in which the integrated J_{sc} of T- and P-PSCs were 20.07 and 20.95 mA/cm^2, respectively. This rise was attributed to the higher electron conductivity and lower N_t of the P-SnO_2 HBL. Furthermore, the well-matched conduction band minimum (CBM) between P-SnO_2 HBL and perovskite allows photo-excited electrons in perovskite to be injected efficiently into the P-SnO_2 HBL [125]. The CBM of P-SnO_2 can be shifted upwardly due to a surface passivation effect induced by healing intrinsic defects and replacing the carbon impurities with oxygens during the PA [46]. The average V_{oc} increased from 1.098 ± 0.008 to 1.124 ± 0.014 V, which can also be interpreted in terms of electron lifetime *via* the lower density of shallow traps such as M-OH in the P-SnO_2 lattice. The low rate of electron mobility and numerous traps induces a disproportionate number of charge carriers, which leads to a sharp rise in recombination probability [109, 130, 131]. Sequentially, the steady-state V_{oc} was measured under illumination to validate our

performance compared with previous reports [132, 133], where the V_{oc} was stabilized to values of 1.14 V and 1.09 V for P- and T-PSC, respectively **(Figure 45b)**. An impressive PCE of 19.56 % was achieved from the P-PSC (J_{sc}: 22.03 mA/cm^2; V_{oc}: 1.147 V; *FF*: 77.4%) **(Figure 45c)**. The SPO corresponding to this cell measured at V_{max} = 0.934 V was 18.53 %, with a steady-state J_{sc} of 19.85 mA/cm^2 **(Figure 45d)**.

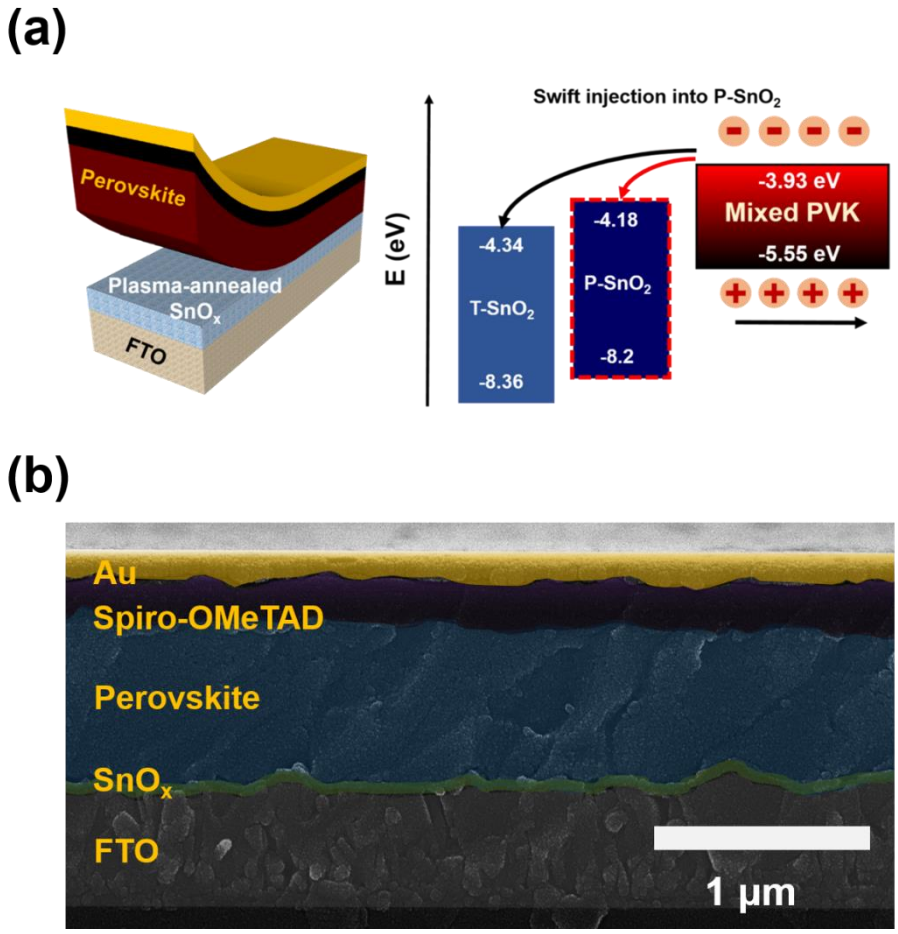

Figure 34. (a) Schematic diagram of the device architecture including the SnO_2 TF as an HBL and band energy diagram showing the behavior of photo-excited electrons at the interface between perovskite and the two types of SnO_2 TFs. The band structure of the perovskite was clarified by a previous report [134]. (b) Cross-sectional FE-SEM image of the P-PSC with a $Cs_{0.056}FA_{0.76}MA_{0.15}PbI_{2.42}Br_{0.48}$ perovskite film.

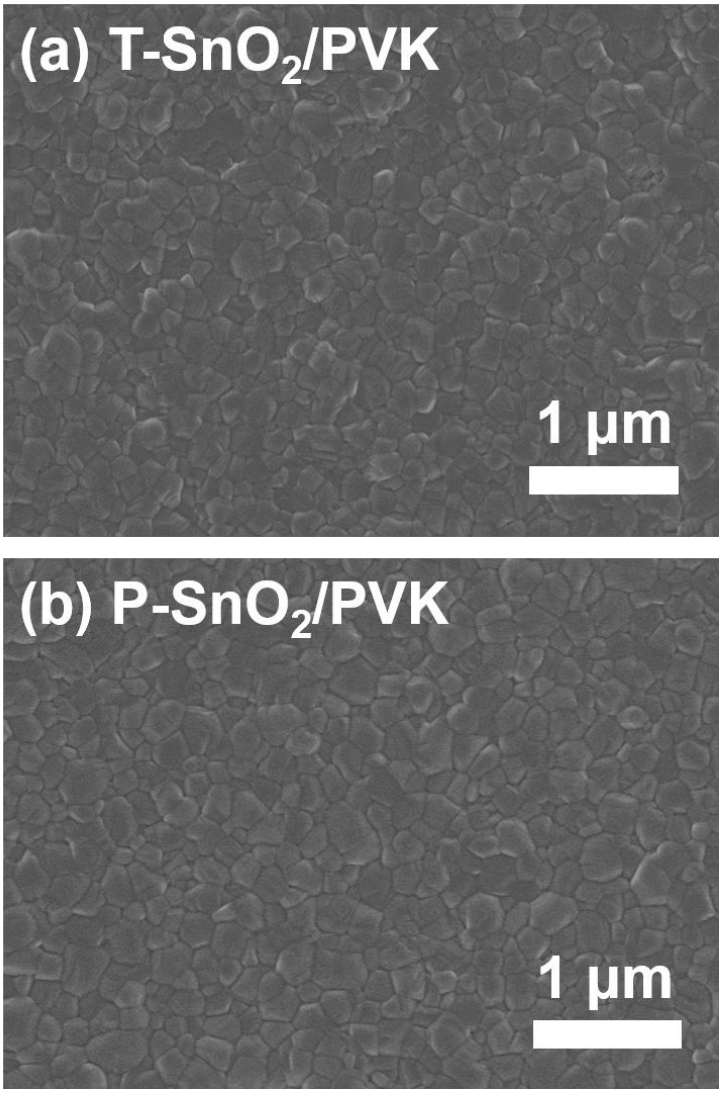

Figure 35. Top-view FE-SEM image of perovskite film ($Cs_{0.056}FA_{0.76}MA_{0.15}PbI_{2.42}Br_{0.48}$) deposited on (a) T-$SnO_2$ and (b) P-SnO_2/FTO glass.

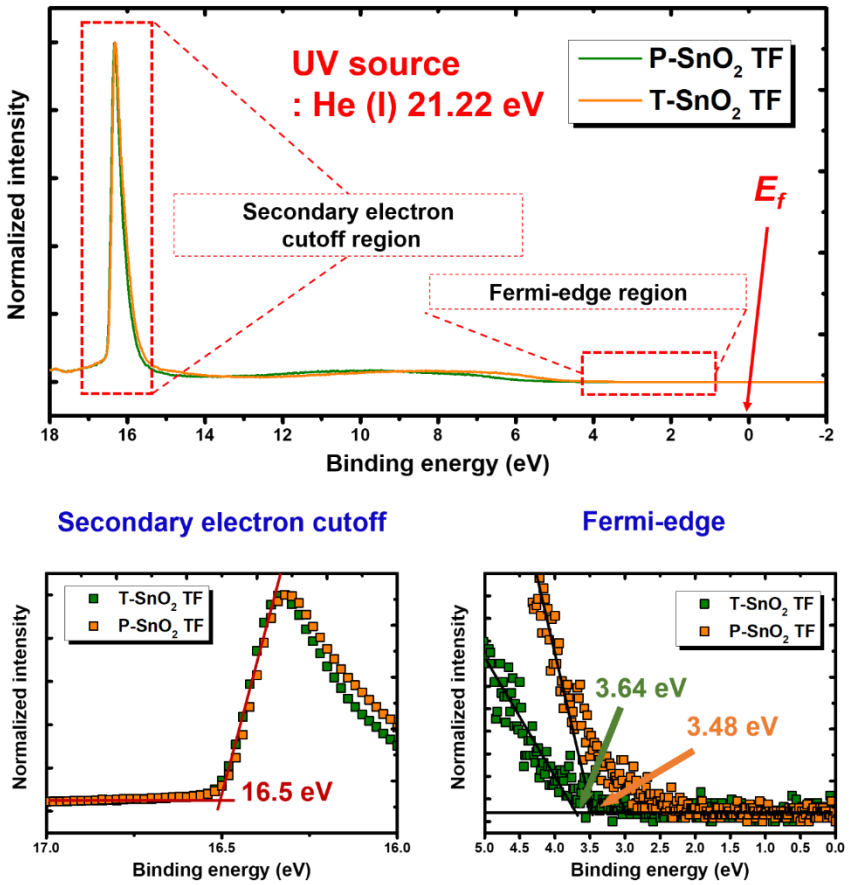

Figure 36. Overall UPS spectra of T- and P-SnO_2 TF coated on FTO glass (upper side), and the expanded spectra at secondary electron cutoff and fermi-edge regions (bottom side).

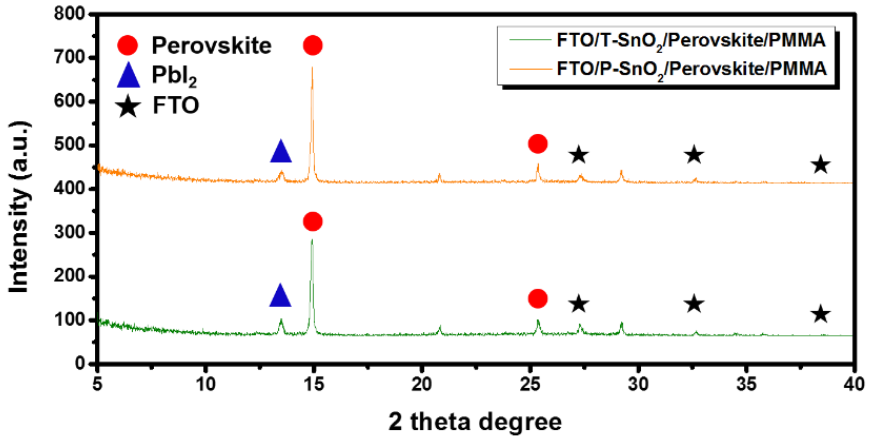

Figure 37. XRD patterns of FTO glass/SnO_2/perovskite devices. Residual PbI_2 was observed in the both cases.

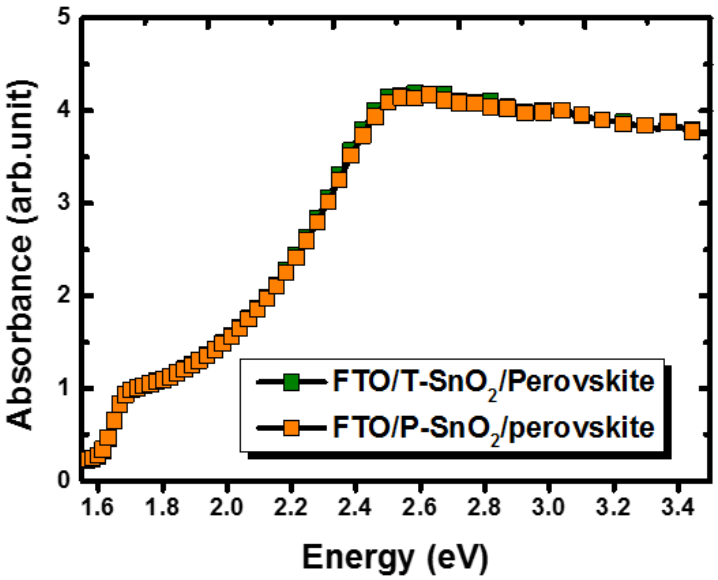

Figure 38. UV/Vis light absorbance spectrum of perovskite coated on the P- and T-SnO_2/FTO glass. The light absorption efficiency was negligible in two cases.

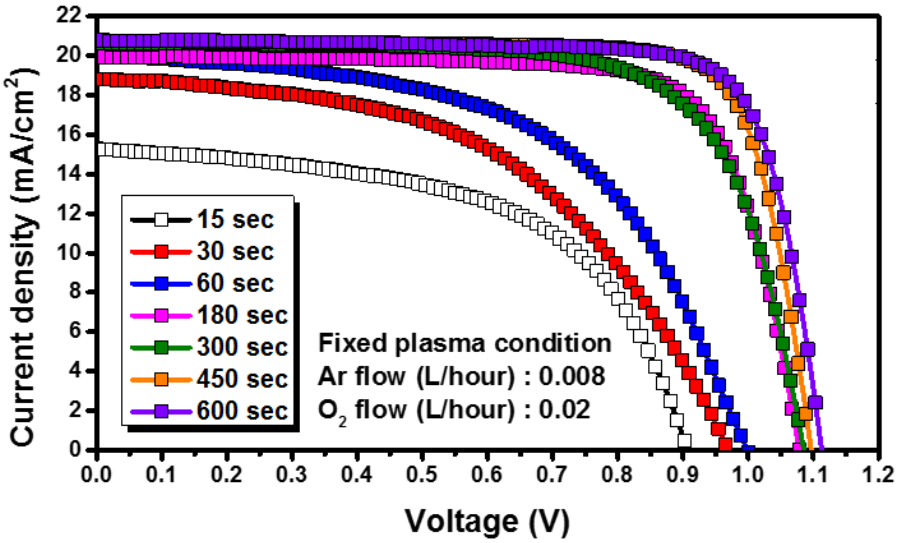

Figure 39. *J-V* characteristics of P-PSCs depending on plasma oxidation time from 15 to 600 s at the fixed gas flow. After 450 s, the PV performance was saturated to a specific point.

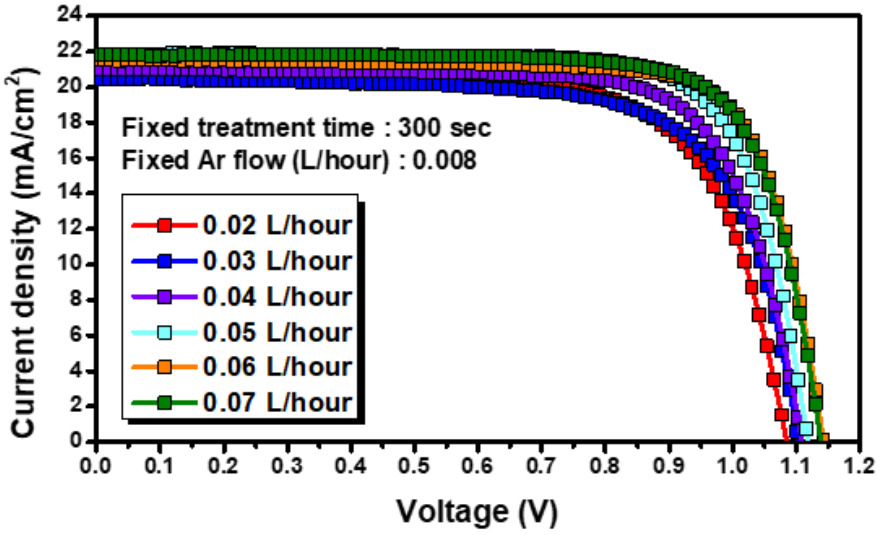

Figure 40. *J-V* characteristics of P-PSCs depending on oxygen gas flow under plasma oxidation from 0.02 to 0.07 L/h at the fixed exposure time (300 s).

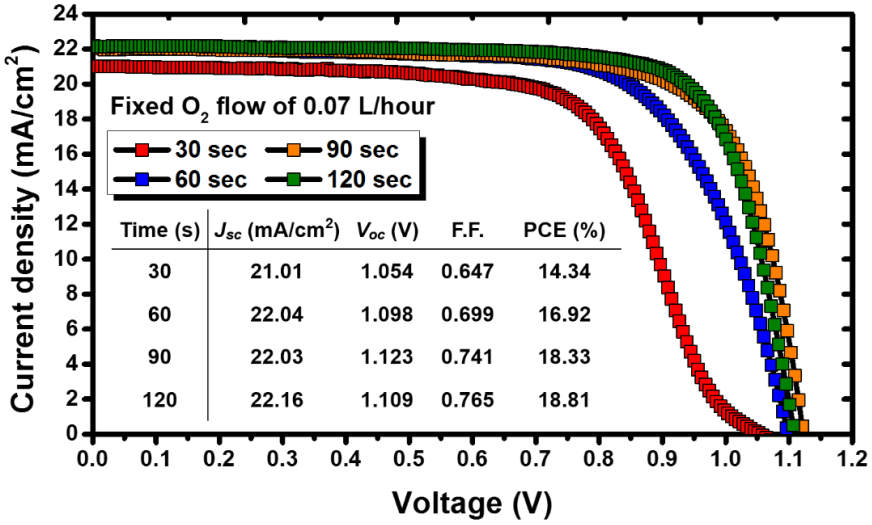

Time (s)	J_{sc} (mA/cm^2)	V_{oc} (V)	F.F.	PCE (%)
30	21.01	1.054	0.647	14.34
60	22.04	1.098	0.699	16.92
90	22.03	1.123	0.741	18.33
120	22.16	1.109	0.765	18.81

Figure 41. *J-V* characteristics of P-PSCs depending on plasma oxidation time from 30 to 120 s at the fixed gas flow (O_2 and Ar of 0.07 L/h and 0.008 L/h, respectively).

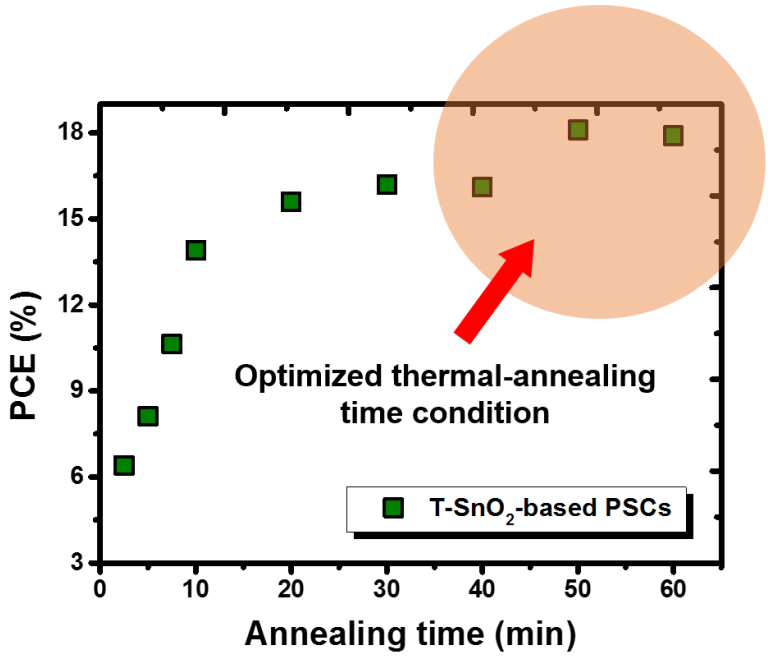

Figure 42. Variation of PCE obtained from T-PSC according to thermal annealing time from 2.5 to 60 min.

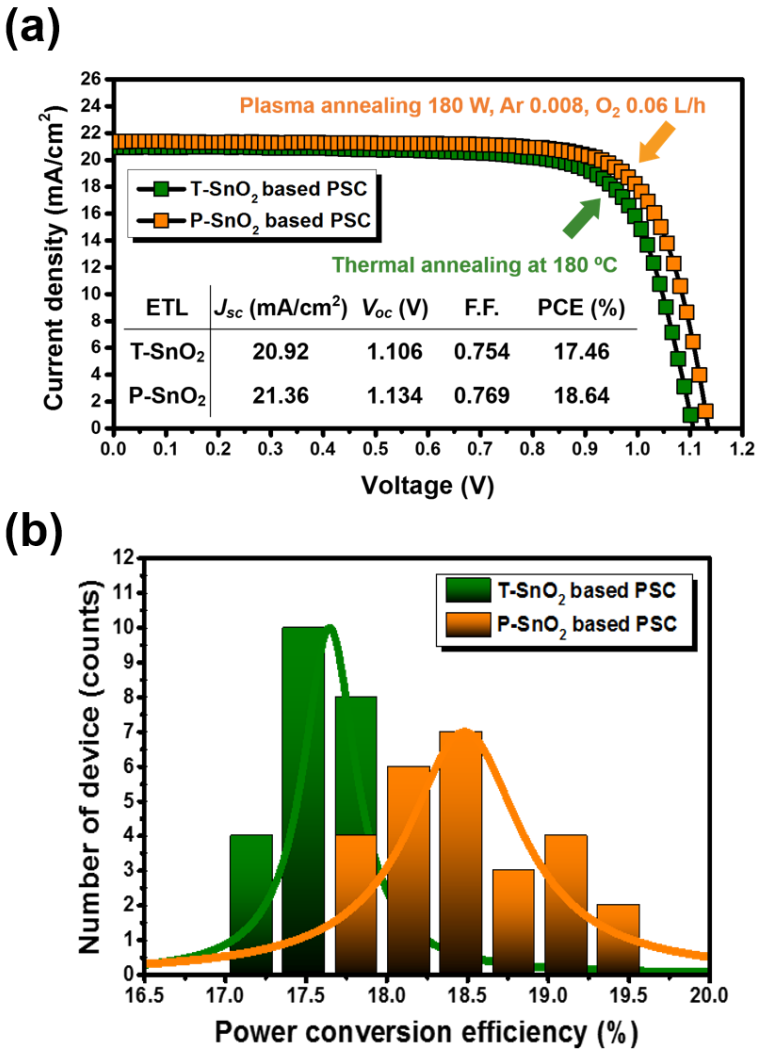

Figure 43. (a) *J-V* curves of the PCSs with T-SnO_2 and P-SnO_2 HBLs measured with an *A* of 0.09 cm^2 under 1 sun illumination. (b) Histogram of the PCE values obtained from each device.

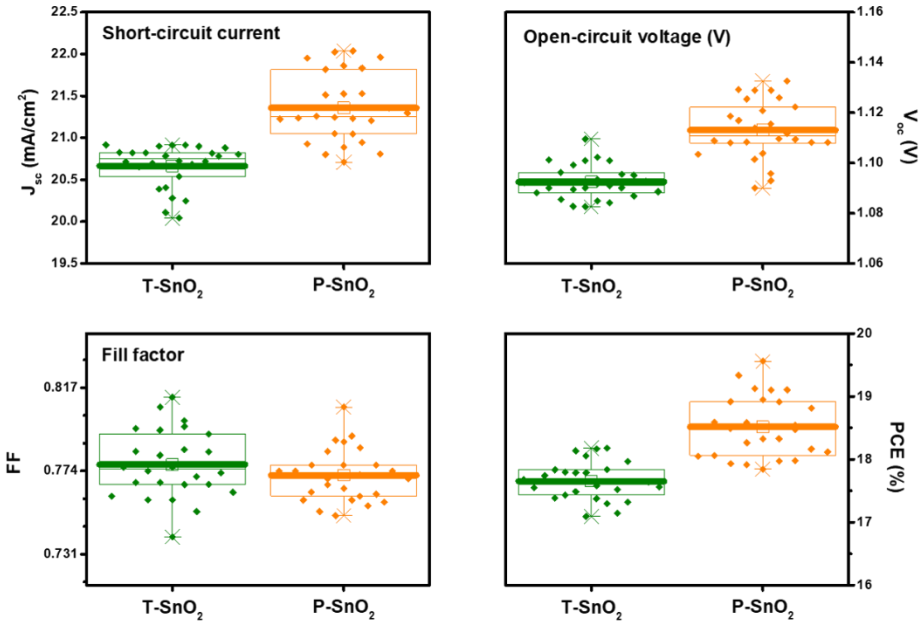

Figure 44. Box charts of PV parameters obtained from T- and P-PSCs to compare the average performance. The mean values are expressed as open squares inside of the boxes and bold lines.

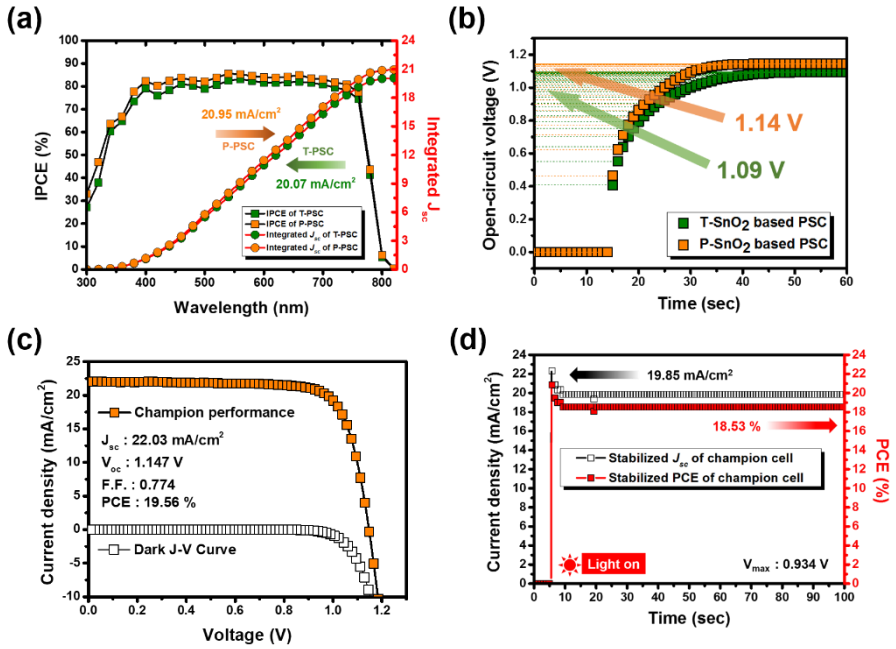

Figure 45. (a) IPCE spectra of PSCs with T-SnO_2 and P-SnO_2 HBLs. The integrated J_{sc} of T- and P-PSCs were 20.07 and 20.95 mA/cm^2, respectively. (b) The steady-state V_{oc} curves measured under 1 sun illumination of each type. (c) Improved performance of the P-PSC, showing a PCE of 19.56 %, and (d) its corresponding steady-state performance measured at a V_{max} of 0.934 V.

Table 3. PV performance evolution of P-PSCs by varying the plasma treatment time from 15 – 450 s at fixed O_2 gas flow rate of 0.02 L/h to confirm the time required for fully oxidation.

Second (s)	J_{sc} (mA/cm^2)	V_{oc} (V)	*FF*	PCE (%)
15 s	15.27	0.906	0.56	7.76
30 s	18.71	0.969	0.508	9.21
60 s	20.01	0.998	0.549	10.97
180 s	19.95	1.078	0.756	16.27
300 s	20.62	1.085	0.712	15.94
450 s	20.78	1.096	0.794	18.09

Table 4. PV performance evolution of P-PSCs by varying the O_2 gas flow rate from 0.02 to 0.07 L/h to check that there is a possibility of further saving of annealing time.

O_2 flow rate	**J_{sc} (mA/cm^2)**	**V_{oc} (V)**	***FF***	**PCE (%)**
0.02 L/h	20.62	1.085	0.712	15.94
0.03 L/h	20.45	1.103	0.714	16.10
0.04 L/h	20.97	1.109	0.745	17.33
0.05 L/h	21.83	1.117	0.762	18.59
0.06 L/h	21.52	1.142	0.777	19.10
0.07 L/h	21.81	1.138	0.770	19.12

Table 5. The tabulated statistical PV metrics of two types of devices, which are corresponds to the result of box charts in **Figure 44**.

SnO_2 type	***J_{sc}*** **(mA/cm^2)**	***V_{oc}*** **(V)**	***FF***	**PCE (%)**
T-SnO_2 TF	20.66 ± 0.259	1.098 ± 0.008	0.777 ± 0.017	17.65 ± 0.299
P-SnO_2 TF	21.36 ± 0.415	1.124 ± 0.014	0.772 ± 0.014	18.52 ± 0.490

3.1.4. Interface charge carrier dynamics at the HBL/perovskite

The electron transfer kinetics was investigated at the SnO_2 HBL/perovskite interface using TRPL with preparing four types of dummy cells: glass/perovskite, glass/FTO/perovskite, and glass/FTO/T- and P-SnO_2 HBL/perovskite **(Figure 46a)**. The resulting curves were fitted by a double exponential model [135]:

$$y = y_0 + A_1 e^{(-t/\tau_1)} + A_2 e^{(-t/\tau_2)}$$

The fast and slow PL decay time constants (τ_1 and τ_2) correspond to quenching of charge carriers by electron extraction from perovskite to HBL and non-radiative decay in the bulk perovskite phase, respectively [136]. The decay mechanism is dominated by electron transfer, in that the τ_2 was overwhelmed by τ_1 having a relative amplitude of over 94 % **(Table 6)**. The fast time constant (τ_1) decreased from 6.6 (T-SnO_2, τ_{avg} of 18.3 ns) to 6.5 ns (P-SnO_2, τ_{avg} of 9.4 ns) with adopting the PA, which indicated the efficient electron extraction from perovskite to P-SnO_2. However, since the difference was smaller than the time-resolution of our TRPL set-up, FS-TA spectroscopy was characterized to precisely gain insight into the charge carrier dynamics under short-circuit conditions **(Figure 46b)** [23, 137]. The behavior of populated carriers such as excited electrons *via* pump energy can be monitored by

stimulated emission after generation of photoexcited charge carriers at the valence band maximum and CBM [9]. The average decay time constant (τ_{avg}) was shortened dramatically from 158.9 to 123.4 ps by introducing the P-SnO_2 HBL, which embodies that the photoexcited electrons in perovskite are extracted more efficiently to the conduction band of P-SnO_2 compared with that of T-SnO_2, possibly explaining the discrepancy in J_{sc}.

OCVD measurements were conducted on second-time scale for the two types of PSCs to figure out the charge carrier kinetics at the SnO_2 HBL/perovskite interface **(Figure 47a)**. Previous studies corroborated that the second time-scale OCVD is strongly connected with charge accumulation and relaxation of electrical dipoles as opposed to electron lifetime in that the electron lifetime calculated from TRPL measurements is within sub-microseconds [138, 139]. The long-lived photovoltage, coincident with an electrostatic potential triggered by the slow release of trapped ions or charge carriers [140], was lower in the P-PSC than the T-PSC; this may be ascribed to the large accumulation of charge carriers in the vast of defects of T-SnO_2 TF due to poor interfacial charge transfer. The strongly existing E-field can deform the perovskite structure by dragging the cation out of PbI_6 cages [141], which makes the PSCs

unstable under operation. The efficient electron injection without accumulation at the P-SnO_2/perovskite junction is in good agreement with TRPL findings shown in **Figure 43a**. Avoiding the accumulation of electrons may alleviate radiative recombination with accumulated holes, thereby leading to not only amelioration of performance hysteresis but also light stability in PSCs [142].

To more accurately observe the differences in electronic transport and carrier recombination at the SnO_2 HBL/perovskite interface as well as the inner series resistance, EIS analysis was carried out on the two devices under 1 sunlight exposure in the frequency range of 1 Hz–1 MHz **(Figure 47b)**. The P-PSC described a smaller semi-circle than T-PSC in the high-frequency range, which reflects prompt charge transfer at the P-SnO_2 HBL/perovskite interface, as demonstrated in OCVD and TRPL measurements**.** This unblocked charge transfer can also reduce the probability of recombination between electrons and holes [142].

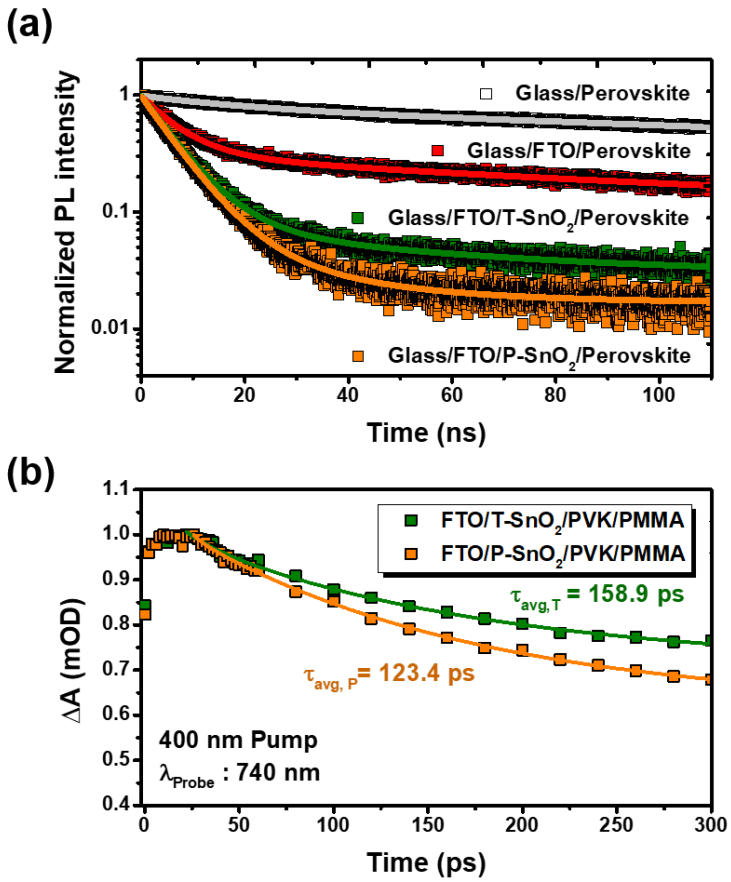

Figure 46. (a) TRPL decay curves extracted from the dummy cells of glass/perovskite, glass/FTO/perovskite, glass/FTO/T-SnO_2 or P-SnO_2/perovskite with an excitation wavelength of 520 nm. (b) The FS-TA time profile of the FTO/T- and P-SnO_2/perovskite/PMMA devices, showing kinetics at 740 nm for the films after excitation at 400 nm.

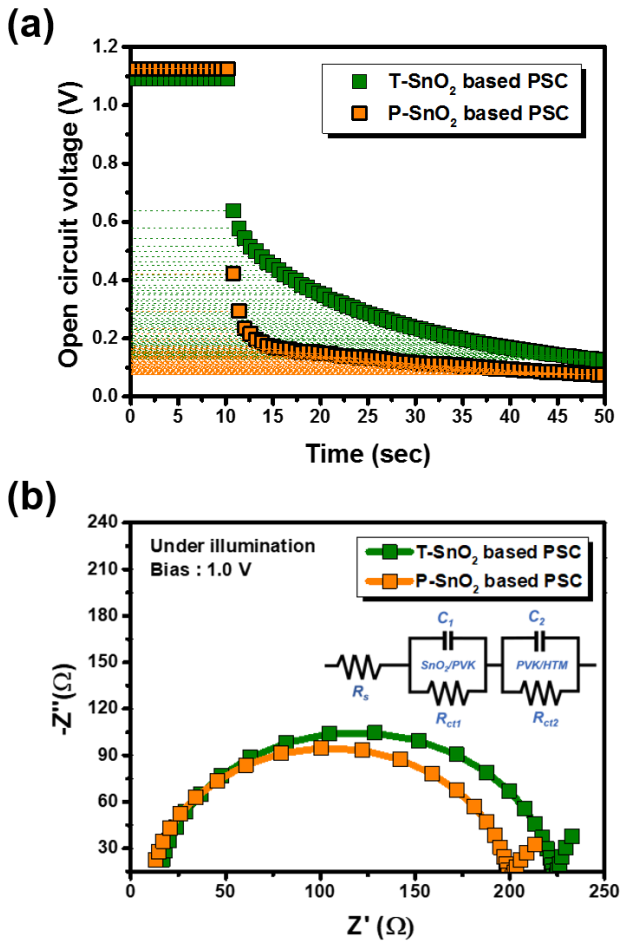

Figure 47. (a) OCVD curves for two types of PSCs recorded in the absence of sunlight. (b) Nyquist plots of the two types of PSCs recorded under illumination conditions over a frequency range of 1 Hz–1 MHz, with a bias of 1 V.

Table 6. Summarizing TRPL decay parameters obtained from glass/perovskite, glass/FTO/perovskite, and glass/FTO/P- and T-SnO_2/perovskite dummy cells. The bi-exponential equation was employed for fitting the TRPL curves.

Dummy cell	τ_1	τ_2	[a] τ_{avg}	W_1	W_2	$W_1/(W_1 + W_2)$
Glass	1258.3	22.8	1258.3	2.320	0.0012	0.99
Glass/FTO	6.8	100.1	83.1	0.718	0.2187	0.76
Glass/FTO /T-SnO_2	6.6	45.4	18.3	0.8574	0.0541	0.94
Glass/FTO /P-SnO_2	6.5	22.6	9.4	0.8491	0.0532	0.94

[a)] $\tau_{avg} = \sum_i W_i \tau_i^2 / \sum_i W_i \tau_i$

Time scale of τ is *ns (nanosecond).*

3.1.5. Device hysteresis and long-term stability

The *J-V* hysteresis of each device was checked by changing the direction of scanning **(Figure 48a)**. The hysteretic behavior of the T-PSC was mitigated by substituting T-SnO_2 with the P-SnO_2 HBL, which was ascribed to the relieved charge accumulation at the P-SnO_2 HBL/perovskite interface. To summarize, the rapid transient response by fast de-trapping of the accumulated charges at the interface can be accomplished due to the low density of traps in the P-SnO_2 HBL, consequently reducing hysteretic behavior [143]. This is reflected in the steady-state J_{sc} test, where the J_{sc} of the P-PSC was stabilized quickly to a saturation point compared with that of T-SnO_2-based PSCs **(Figure 48b)**. The fast response of P-PSCs to sunlight is in good agreement with the relieved hysteresis behavior, as hysteresis is closely associated with charge accumulation at the HBL/perovskite interface [28].

The durability of T- and P-PSC in an ambient environment was tested without encapsulation **(Figure 49a)**. There is little difference in air stability according to HBLs, and it seems to be more dominated by the perovskite itself or the encapsulation. Against 30% RH stress, our PSCs boasted a respectable stability by retaining *ca*. 85% of its original performance even after 320 h. However, the photostability, which is

highly influenced by the charge carriers at the perovskite/HBL interface, was superior in the P-PSCs compared with the T-PSCs **(Figure 49b)**. The performance of the P-PSC degraded to *ca.* 75% of its initial performance under constant 1 sun illumination without UV-filter, whereas the T-PSC suffered severely deteriorated performance (*ca*. 45% of its initial PCE). As characterized above, the serious charge accumulation at the perovskite/HBL interface would cause degradation of adjacent perovskite by combining with moisture [144], and might induce deformation of the perovskite structure under operation [141].

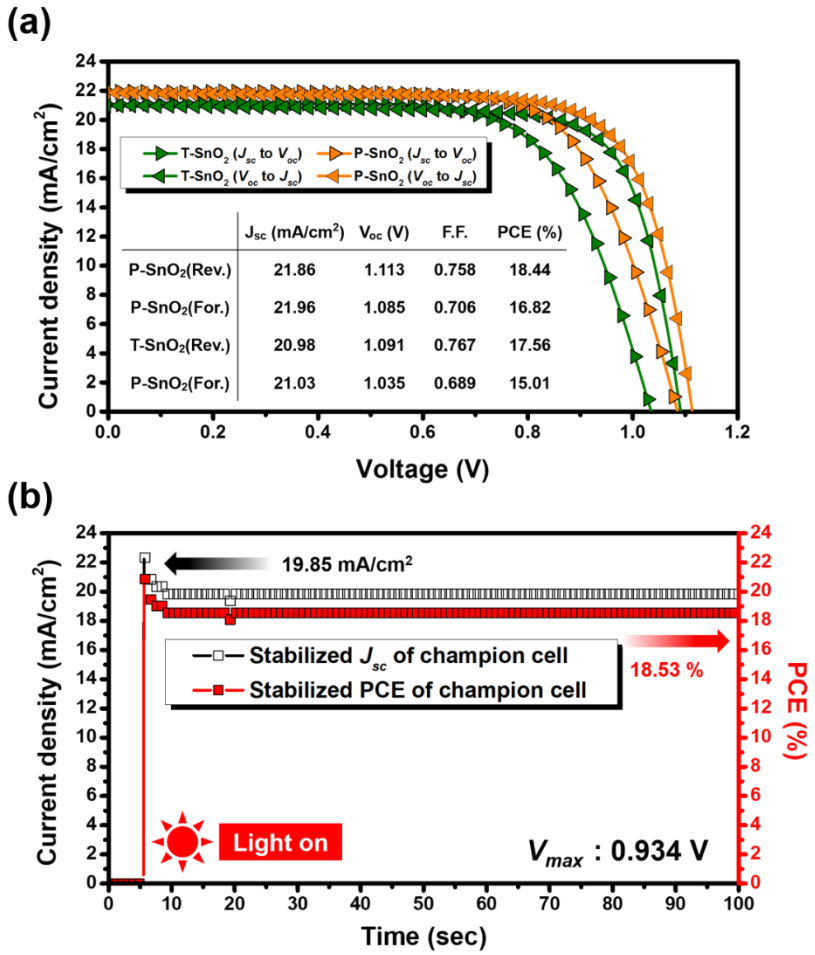

Figure 48. (a) *J-V* curves of each type of PSC measured by forward and reverse scans where the hysteresis was alleviated by introduction of the P-SnO_2 HBL. (b) The SPO results of T- and P-PSCs measured at their maximum power voltage (V_{max}) of 0.914 and 0.921 V, respectively.

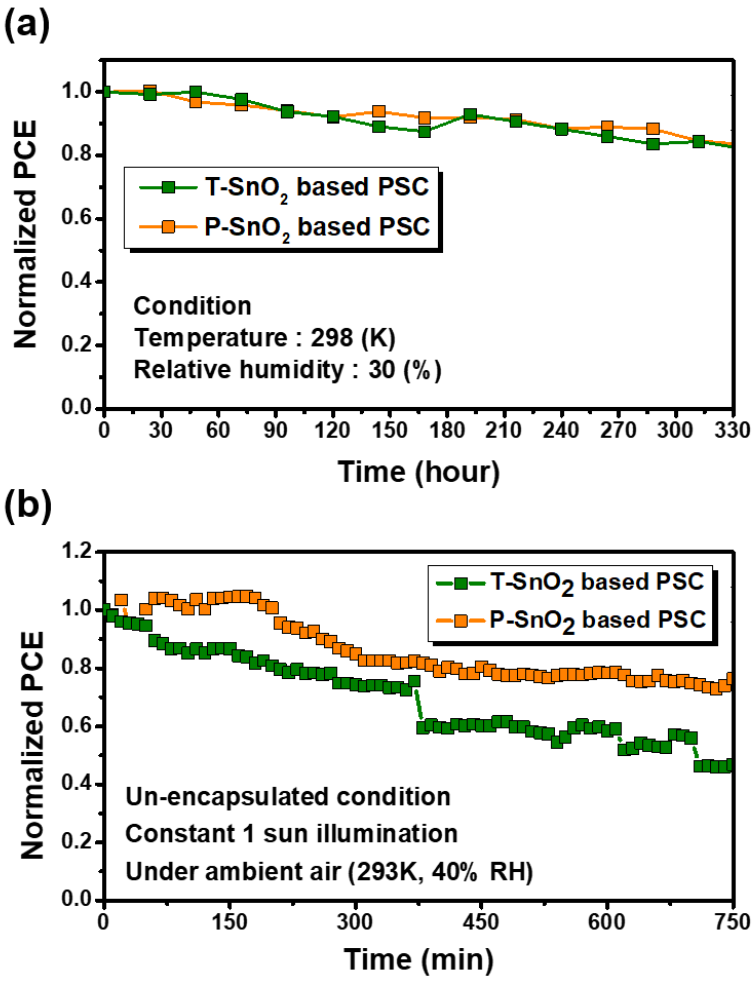

Figure 49. (a) Air-stability test of the T- and P-PSC stored in an ambient environment of 298 K and 30 % RH conditions without encapsulation. (b) Evolution of normalized PV performance of T- and P-PSC during the photostability test under constant 1 sun illumination and an ambient environment (298 K, 40% RH) without encapsulation or UV-filter.

3.2. Large-grained perovskite-based HBL-free PSCs

3.2.1. Device fabrication based on large-grain perovskite

Overall schematic configuration of the PSCs rendered in this work is shown in **Figure 50a**, portraying the simple-structured PSC without a HBL. To construct the $MAPbI_3$ film which plays a role as the HBL as well as a sensitizer, the precursor prepared with various concentration (37, 44, 51, 58 wt%) was directly spin-coated on the blank FTO substrate without coating a HBL, followed by introducing a HTL with a thickness of *ca.* 200 nm to allow holes to be quickly separated from the $MAPbI_3$ phase. The HTM spread evenly in all cases, which not only facilitated a charge migration because of conformal contact of the metal with the HTL but also provided high light absorption due to excellent reflection by the metal [145]. The fabrication process was completed by thermally evaporating the 60-nm-thick layer of gold.

The energy level diagram for our device is illustrated in **Figure 50b**. The free charges generated in $MAPbI_3$ by the sunlight absorption can be transported to the FTO or HTL by charge gradient-induced diffusion and charge shifting triggered by the built-in potential of *p–i–n*-type solar cells [146]. Respective layers are clearly indicated at low and high magnifications in **Figure 50c** and **51b**. Also, a surface of $MAPbI_3$ with a

large grain size (*ca.* 400 – 900 nm) was developed with full coverage, which is evident in the **Figure 51a**. A photograph of the completed device is shown in **Figure 51c**.

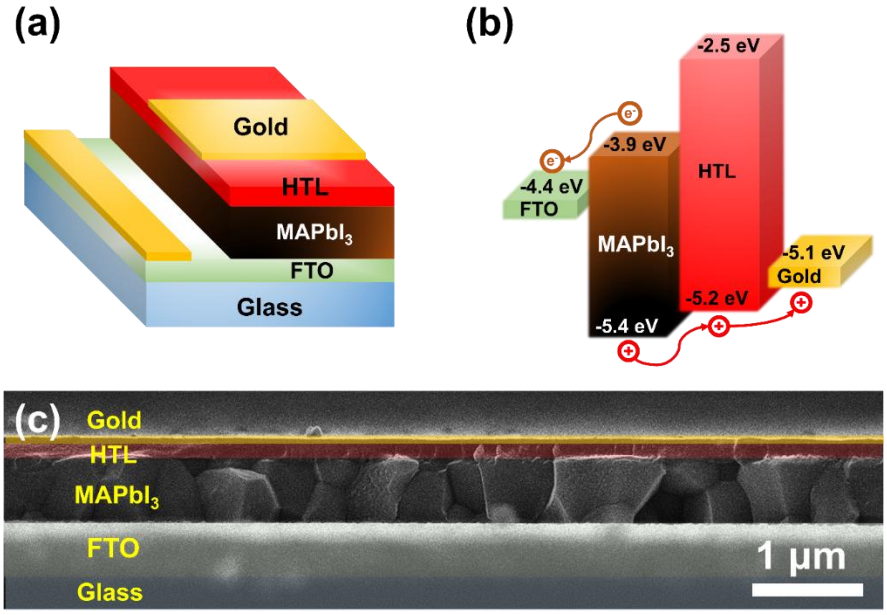

Figure 50. (a) Schematic images representing device configuration and (b) band-gap diagram of the HBL free PSCs. (c) FE-SEM side-view of the HBL-free PSCs.

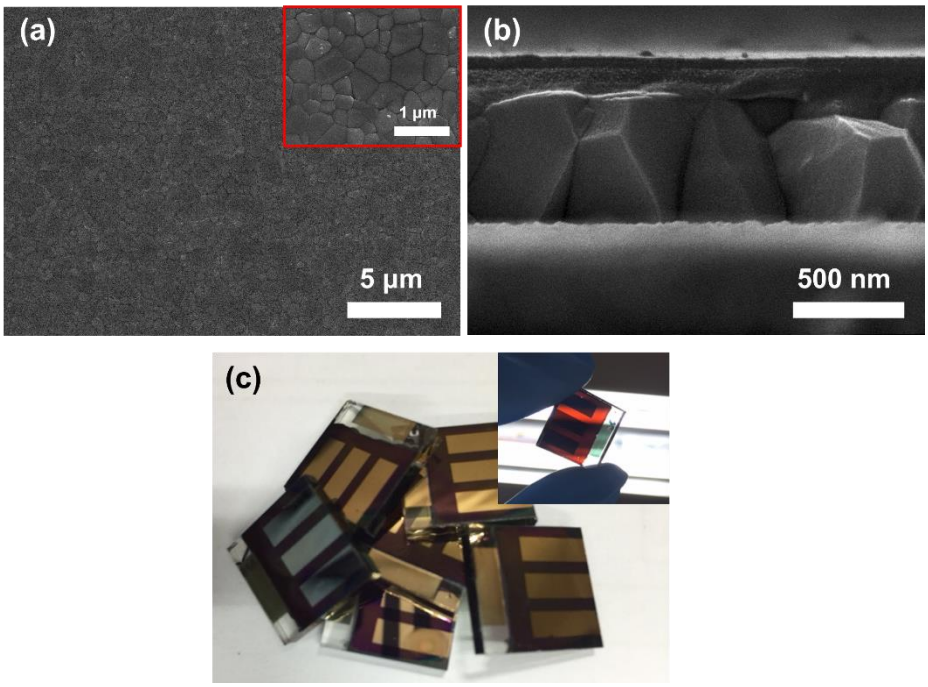

Figure 51. (a) FE-SEM image of $MAPbI_3$ surface crystallized from 51 wt% precursor solution. The inset is a high-magnification view of the same film. (b) FE-SEM cross-sectional image of the PSCs obtained at high magnification. (c) Digital image of highly transparent PSCs fabricated in the laboratory.

3.2.2. Characterization of the prepared perovskite film

To evaluate the effects of $MAPbI_3$ grain size and film thickness on blockage of HTM permeation, the four types of films were prepared using the before-mentioned $MAPbI_3$ precursors. (37, 44, 51 and 58 wt%) All of the $MAPbI_3$ films spin-coated with different precursors were crystallized with the SA procedure to ensure better electrical performance [99, 147]. The $MAPbI_3$ films were solvent-annealed for 1 h to guarantee maximum grain size for each precursor concentration.

From FE-SEM images of the prepared films as shown in **Figure 52**, the thickness of films increased from *ca.* 330 nm (37 wt%) to 870 nm (58 wt%) at the indicated spin-coating rate **(Figure 52a-d).** And it is also evident from **Figure 52e-h** and **Figure 53** that the grain size simultaneously followed the same trend as thickness, which is in good agreement with previous findings [99]. While the grain size of the $MAPbI_3$ obtained from the 37 wt% precursor solution was *ca.* 200 – 300 nm horizontally, that from the 58 wt% precursor solution was significantly greatened up to *ca.* 1000 nm.

The surface roughness of $MAPbI_3$ was characterized by AFM images **(Figure 54)**. Lower film roughness was apparent for larger grain sizes (17 - 19 nm) because the ratio of large grains with smooth surfaces was

greater. Smooth films are desirable for better attachment between $MAPbI_3$ and the HTM, and free holes can be efficiently extracted from $MAPbI_3$ to the HTM [148]. Therefore, it is obvious that large-grain-based PSCs would exhibit better electrical performance than small-grain-based PSCs.

XRD patterns were analyzed to assess the crystallinity of the $MAPbI_3$ films **(Figure 55a)**. All films were consistent with the tetragonal phase of $MAPbI_3$, with diffraction peaks at 15.04 and 27.36° corresponding to the (110) and (220) planes, respectively. The (110) and (220) diffraction peaks were intensified with increasing grain size, indicating that the $MAPbI_3$ crystal structure was highly oriented with low defect density [149]. Forming the large crystals is unconditional in HBL-free structure to offset the disadvantages originated from the absence of adjacent charge transport layer (e.g. TiO_2 or ZnO).

Figure 55b denotes the incident light absorption properties of the prepared films. With increasing grain size and thickness, the light soaking to $MAPbI_3$ was enhanced from the UV range to 800 nm without any band-gap shift. This was attributed primarily to the high volume of the light absorber and improved crystallinity because of the large grains [150].

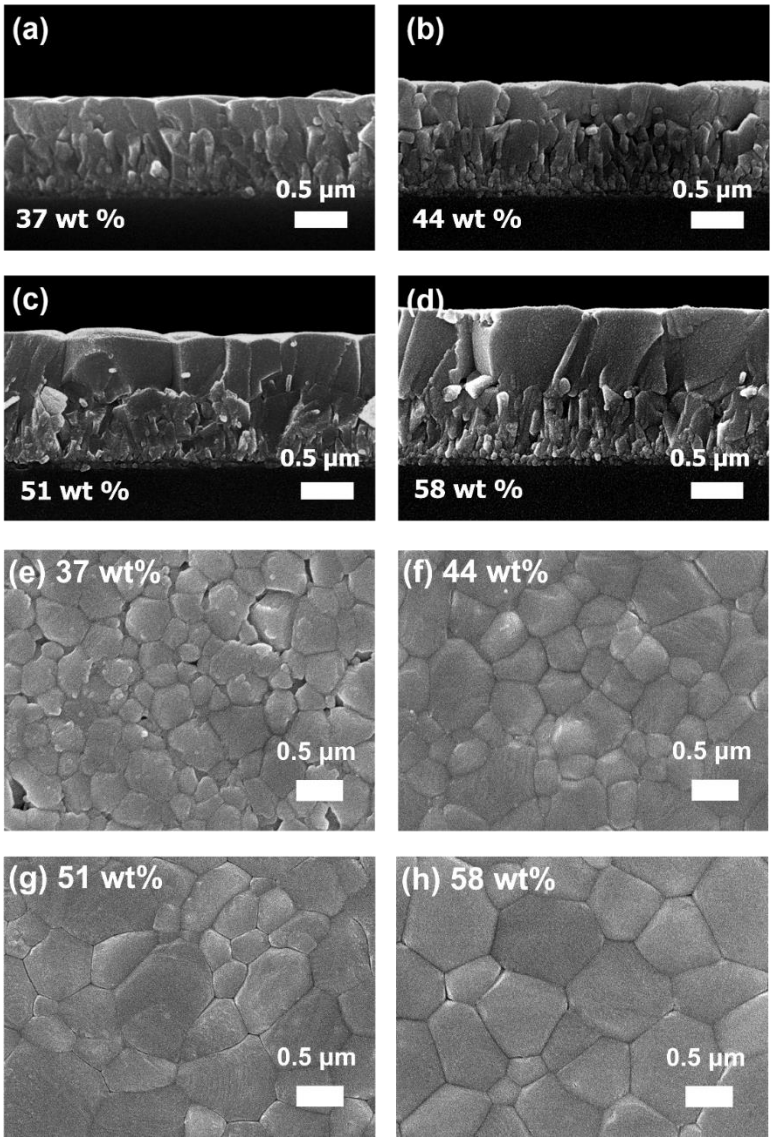

Figure 52. Cross-sectional (a-d) and surfacial FE-SEM (e–h) showing $MAPbI_3$ films prepared by stock solutions of 37, 44, 51, and 58 wt% respectively

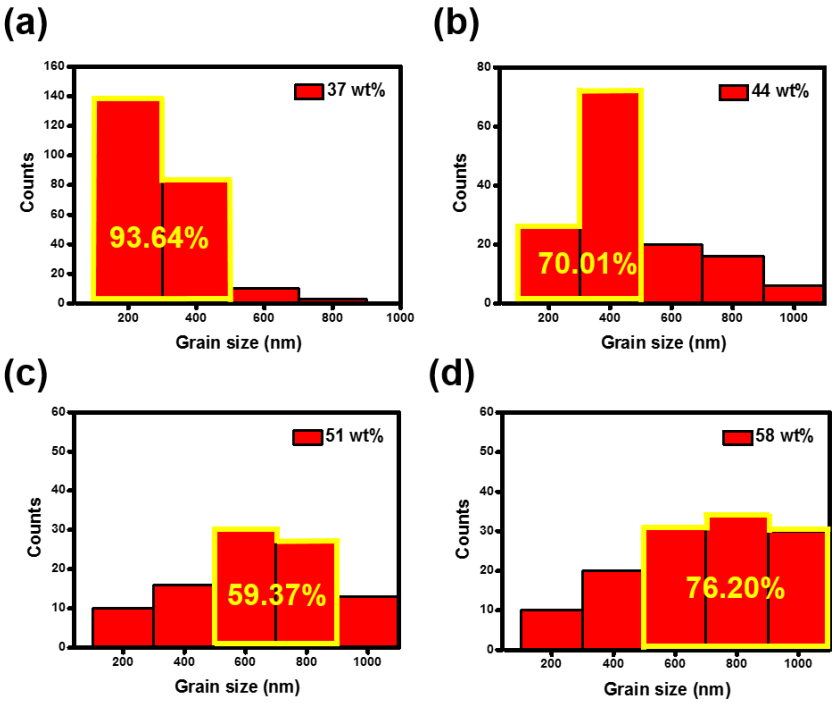

Figure 53. Grain size distribution of $MAPbI_3$ perovskite films coated using (a) 37 wt%, (b) 44 wt%, (c) 51 wt% and (d) 58 wt% precursor solution, respectively.

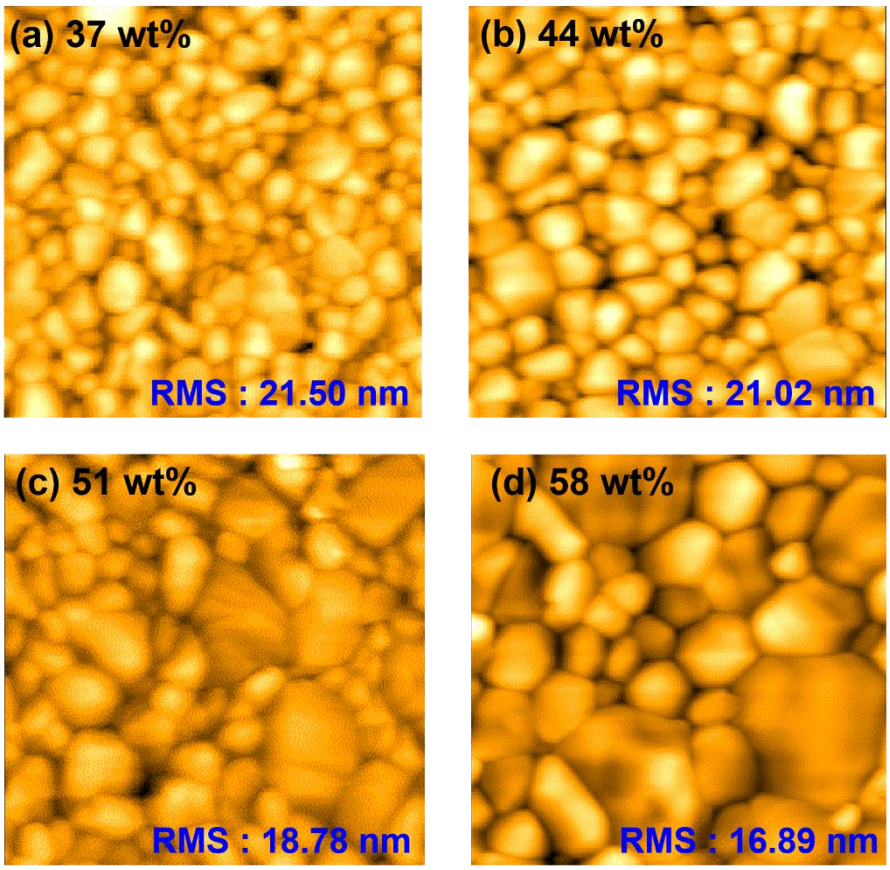

Figure 54. Surface AFM images (a–d) showing $MAPbI_3$ films prepared by stock solutions of 37, 44, 51, and 58 wt% respectively. The projected area of the AFM images is 25 μm^2 (5 × 5 μm). The RMS means root-mean-square roughness of the films.

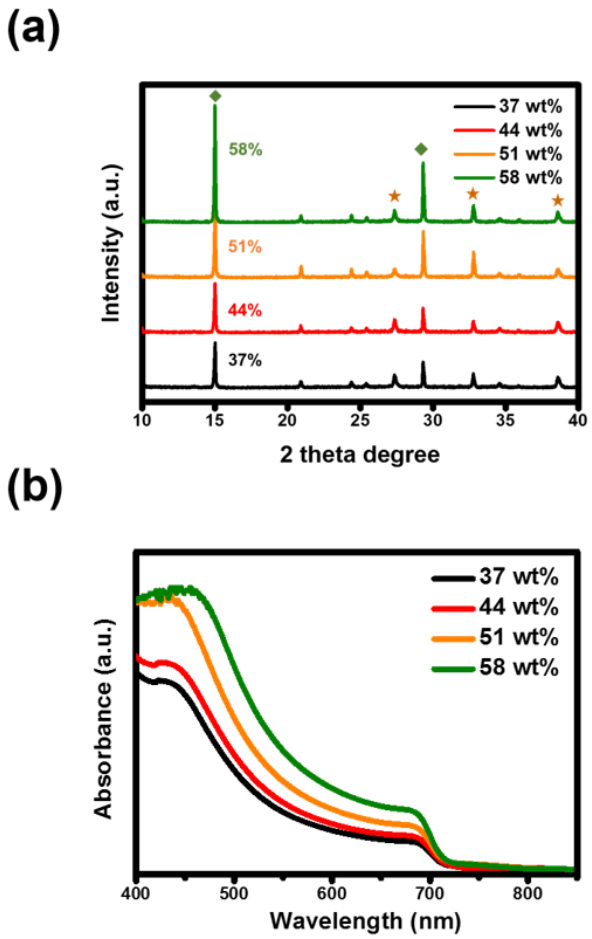

Figure 55. (a) XRD patterns, (b) UV-Vis absorption spectra for $MAPbI_3$ thin films deposited using various precursor solution concentrations.

3.2.3. Photovoltaic performance of HBL-free PSCs

On the basis of $MAPbI_3$ grain size and film thickness information, the performance of assembled devices was estimated under 1 sun illumination. **Figure 56a** exhibits that cell performance was improved with increasing concentration of stock solution. Average performance was confirmed for 25 devices prepared at each concentration **(Figure 57).** All PV parameters were comparatively poor for the 37 wt%-based PSCs. The parameters were steadily increased with thickening stock solution, and reached saturated values in the 51 wt%-based PSCs. At greater than the optimal concentration, although the J_{sc} was exiguously reduced because of mismatch between the perovskite absorption depth and diffusion length of charge carriers, the significant reduction of J_{sc} could be avoided and sufficiently high performance was maintained in the 58 wt%-based PSCs.

The V_{oc}, that is conventionally defined as the difference between the lowest unoccupied molecular orbital (LUMO) level of the perovskite and the highest occupied molecular orbital (HOMO) of the HTM, typically exceeded 1.05 V in all cases [151]. There would have been negligible changes in the HOMO or LUMO levels of the films because the same type of perovskite and HTM were applied to fabricate the PSCs.

However, the much improved V_{oc} was obtained in the concentrated film-based PSCs (51, 58 wt%), which was possibly ascribed to decrease of non-radiative recombination due to the large grain and heavy thickness of $MAPbI_3$ [152].

The obtained photocurrents were in good agreement with the external quantum efficiency (EQE) spectra **(Figure 56b)**. The champion efficiency of 18.20% was achieved with J_{sc} of 21.45 mA/cm^2, V_{oc} of 1.127 V, and FF of 0.751 **(Figure 56c)**. The EQE spectra and integrated photocurrent were consistent with those acquired from the *J–V* characteristics **(Figure 56d)**.

The hysteretic behaviors of the HBL-free PSCs were also evaluated using the PSCs fabricated by 51 wt% based-$MAPbI_3$ film **(Figure 58a)**. The ratio between the forward- and reverse-scan PCEs was *ca*. 0.8, which was a low level hysteresis in consideration of absence of n-type HBL and was comparable with that of the previously reported result [153]. However, the extent of hysteresis in HBL-free PSC was quite serious compared with that of TiO_2 HBL-inserted PSC due to the slightly slow charge extraction rate **(Figure 58b)** [154], and accordingly further works are in progress to achieve the hysteresis-less HBL-free PSC.

To accurately approve the confidence of performance measured from

HBL-free PSC, and assure the extent of device hysteresis, the steady-state photocurrent density and PCE were estimated at maximum power output (0.925 V deduced from reverse scan result) for 80 s in **Figure 59**. The stabilized photocurrent density (black) of HBL-free PSC was 16.86 mA/cm^2, corresponding to a power output of 15.59 mW/cm^2 (= PCE of 15.59 %). The SPO is close to the average value of efficiencies obtained from forward and reverse scan direction, which denotes the performance credibility of HBL-free PSCs.

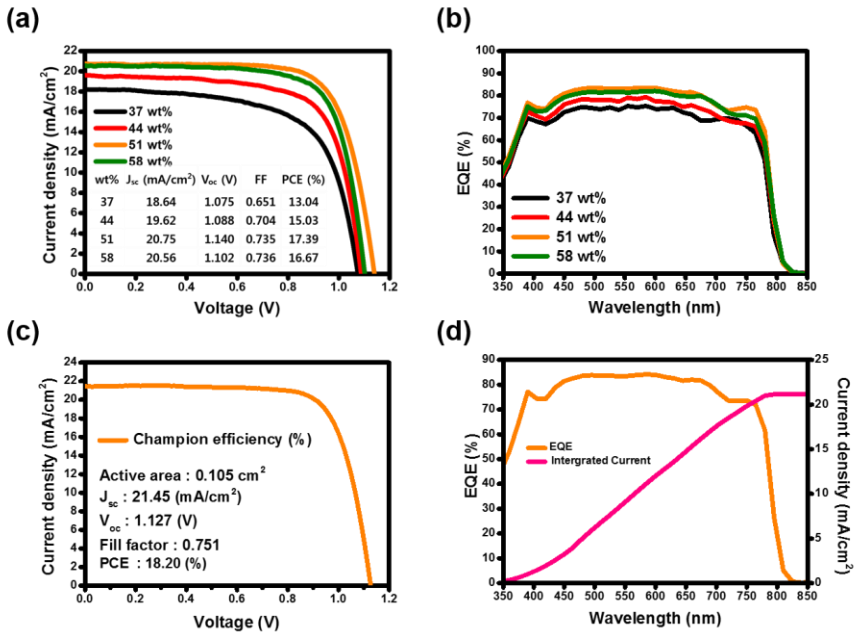

Figure 56. (a) *J–V* characteristics and (b) EQE spectra of PSCs of different $MAPbI_3$ thicknesses. (c) Performance and (d) EQE spectrum for the best-performing cell. The integrated current density derived from the EQE spectrum was 21.20 mA/cm^2.

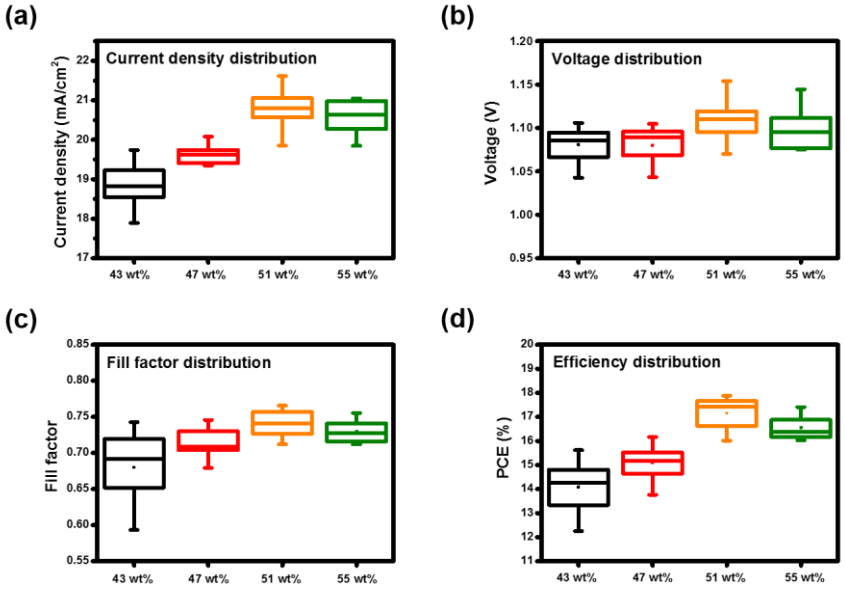

Figure 57. Variation and comparison of the PV parameters such as (a) J_{sc}, (b) V_{oc}, (c) FF, and (d) PCE of the HBL-free PSCs. These parameters were evaluated from 25 devices fabricated for each concentration.

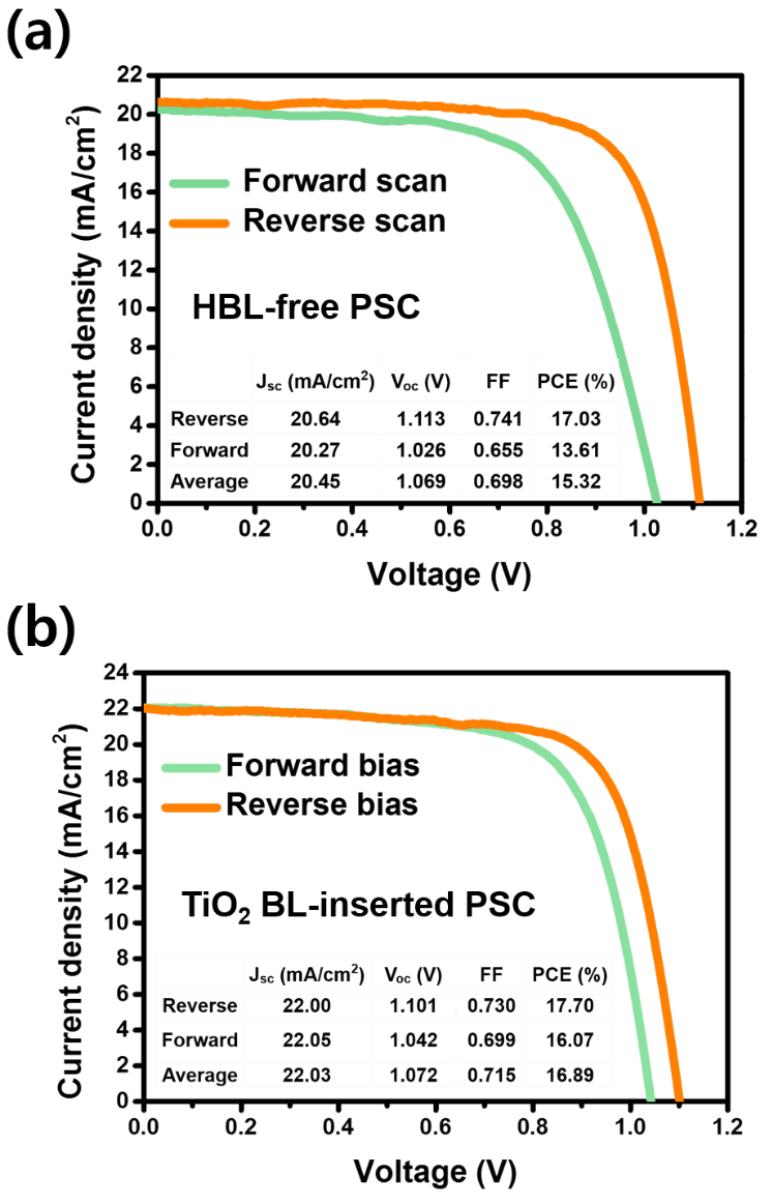

Figure 58. *J–V* hysteresis of the (a) the HBL-free and (b) TiO_2 HBL-inserted PSCs fabricated with 51 wt% based-$MAPbI_3$ film.

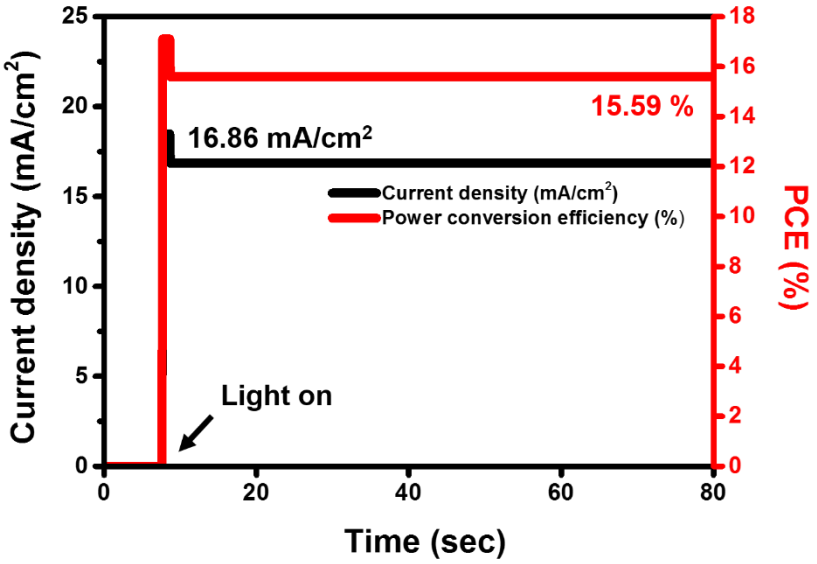

Figure 59. Stabilizing photocurrent and PCE of the HBL-free PSCs fabricated by optimized condition (51 wt% of perovskite precursor), measured at the maximum power point (0.925 V) for 80 s.

3.2.4. Key factors for high performance of HBL-free PSCs

To clarify key factor on the improved performance in this simplified type, the perovskite grain size dependent *J-V* characteristics were tested under a condition of the fixed film thickness **(Figure 60)**. On the contrary to the solvent-annealed film **(Figure 60d)**, the normally-annealed $MAPbI_3$ films were built with very small grains **(Figure 60c)**, and the completed devices indicated the humble PCE which is *ca*. 80 % of the PCE obtained from solvent-annealed device **(Figure 60b)**. Furthermore, to understand the effect of film thickness in HBL-free PSCs without a big variation in grain size, the performance of 37 wt%-based PSCs (*ca*. 330 nm thickness, SA) could be compared with the normally-annealed film shown in **Figure 61** (51 wt%, *ca*. 650 nm thickness). The latter showed the slightly increased J_{sc}, FF and PCE than those of the former, and it can be seen that film thickness slightly contributed to optimization of the efficient HBL-free PSC. From these results, it was proved that the $MAPbI_3$ grain size is a more decisive factor than film thickness for realization of the highly efficient HBL-free PSC and effective interruption of HTM penetration. As corroborated above, the outstanding PCE was acquired from 51 and 58 wt% based PSCs, which implies that the penetration of HTM is completely prevented from the $MAPbI_3$ film

on condition that the perovskite is crystallized with an ideal grain size (0.6 ~ 1 μm) and perfect coverage. Moreover, these highly crystalline grains intrinsically have lots of merits such as the long diffusion length of charge carriers and fewer defects [86, 99, 152]. This is why the high performance is continued in 58 wt%-based PSCs over the optimum concentration (51 wt%).

To assure our hypothesis about the recombination between HTM and FTO, the EIS was measured from 1 Hz to 1 MHz under dark and illumination conditions at 0.7 V bias. Under the dark condition **(Figure 62a)**, the charge transfer resistance (R_{ct}) of HTM in the high-frequency region and charge recombination resistance (R_{rec}) between FTO and HTM in the low-frequency region were analysed [155]. It was challenging to characterize the difference in charge transport behavior because the arcs were indistinct in the high-frequency region. However, the main arcs in the low-frequency region clearly indicated that the R_{rec} was elevated with increasing the grain size of $MAPbI_3$. It stands for that harmful contact of HTM with FTO frequently occurred in the small $MAPbI_3$ grain-based PSCs. Accordingly, the V_{oc}, FF and PCE of HBL-free PSC could be enhanced in 51 and 58 wt% based-PSCs consisting of large grains [152].

In other words, as can be seen from **Figure 62b**, the performance variation stems from the difference in the HTM blockage ability determined by $MAPbI_3$ grain size. In case of the 37 and 44 wt%-based PSCs, it is awkward to effectively inhibit the penetration of the HTM to the FTO, and there is a high probability of electron-hole recombination at the interface. It would be a main reason of poor performance in PSCs fabricated by stock solution of 37 wt%. However, over the *ca*. 700 nm of $MAPbI_3$ grains (51 and 58 wt%), the outstanding performance was achieved, which demonstrated that the hole-blocking effect of $MAPbI_3$ film could be feasible if a satisfactorily large grain $MAPbI_3$ films were prepared with perfect surface coverage. The $MAPbI_3$ film consisting of large grains has a small number of crevices per unit area, which can reduce the passage for HTM infiltration and alleviate damaging recombination provoked at interface between FTO surface and HTM. Additionally, it is reckoned that the infiltrating HTM may frequently collide with the $MAPbI_3$ grains in a thick film and stop penetrating, thereby minimizing the likelihood of arrival at FTO. Even though the thickness is judged as a minor factor compared with grain size from the results of **Figure 60b and 61**, it is imperative to harmoniously combine the two factors for excellent PV performance.

Also, the influence of perovskite crystallinity on PCE is need-to-know factor to verify our hypothesis. As shown in **Figure 63**, after DMSO annealing, the PCE of TiO_2 HBL-inserted-PSC increased by 7 % due to the enhanced crystallinity of $MAPbI_3$ with enlarging grain size. However, the increase of 21 % in PCE was confirmed in case of HBL-free PSC, which demonstrates that the effect of HTM blockage was significantly involved in performance improvement as a pivotal factor besides the enhanced crystallinity. In brief, the control of HTM permeation through increasing $MAPbI_3$ grain size is a more reasonable cause for the improved performance.

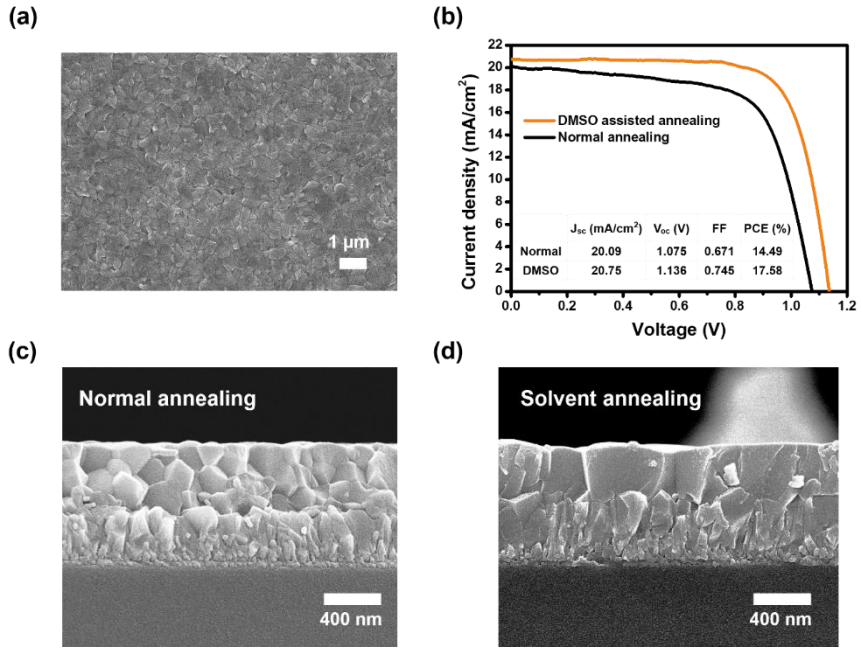

Figure 60. (a) FE-SEM image of $MAPbI_3$ surface crystallized through a normal annealing method. (b) Performance comparison of HBL-free PSCs depending on annealing methods. (c) Cross-sectional FE-SEM image of $MAPbI_3$ film fabricated with normal annealing and (d) solvent-annealing.

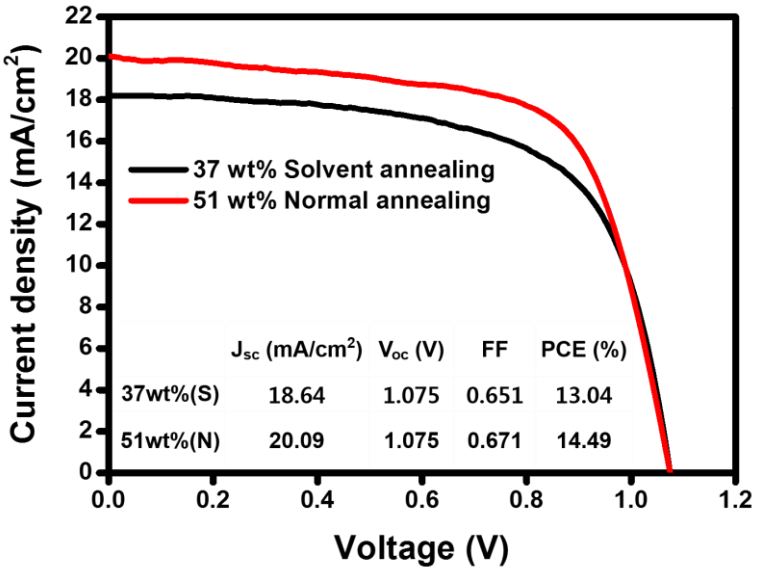

Figure 61. Performance comparison of the HBL-free PSCs depending on film thickness. The grain size of solvent-annealed film prepared by 37 wt% precursor has similar with that of the normally annealed film prepared by 51 wt% precursor.

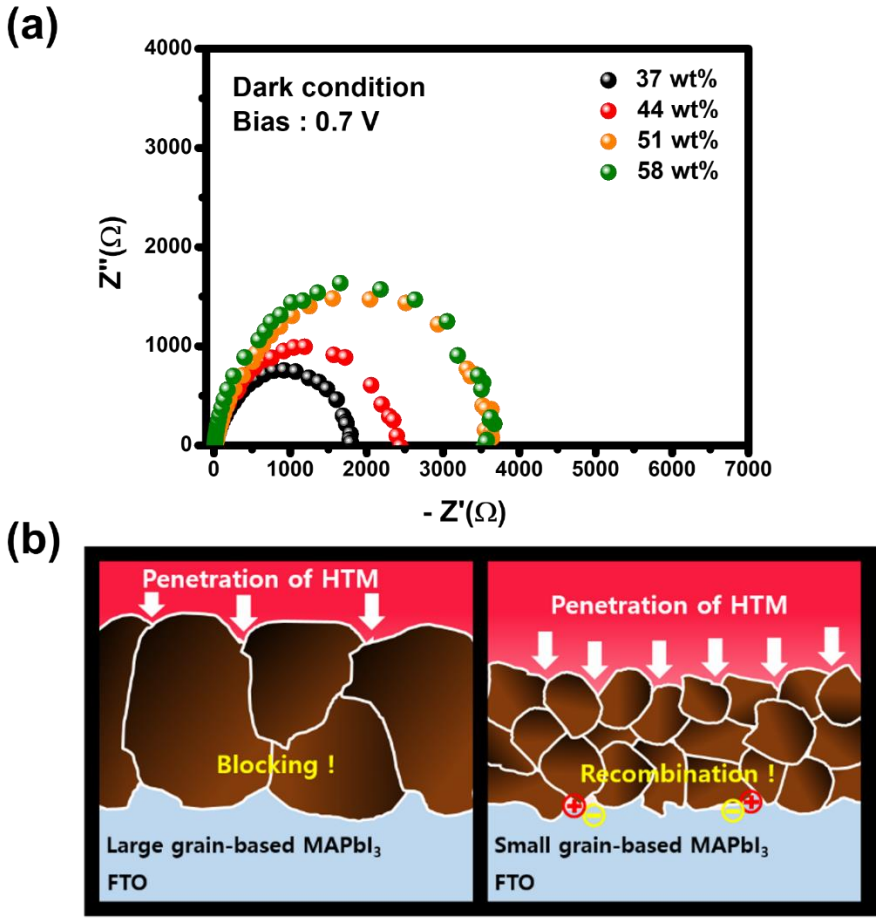

Figure 62. (a) Nyquist plots of the HBL-free PSCs as a function of precursor concentration under dark condition at 0.7 V bias. (b) An illustration depicting the penetration of the HTM into a perovskite film through a crevice. (Left) The penetration of HTM can be disturbed by large grains densely located along an orthogonal path in a high-thickness film. (Right) On the other hand, the HTM can easily reach the FTO surface through many penetration pathways (GBs).

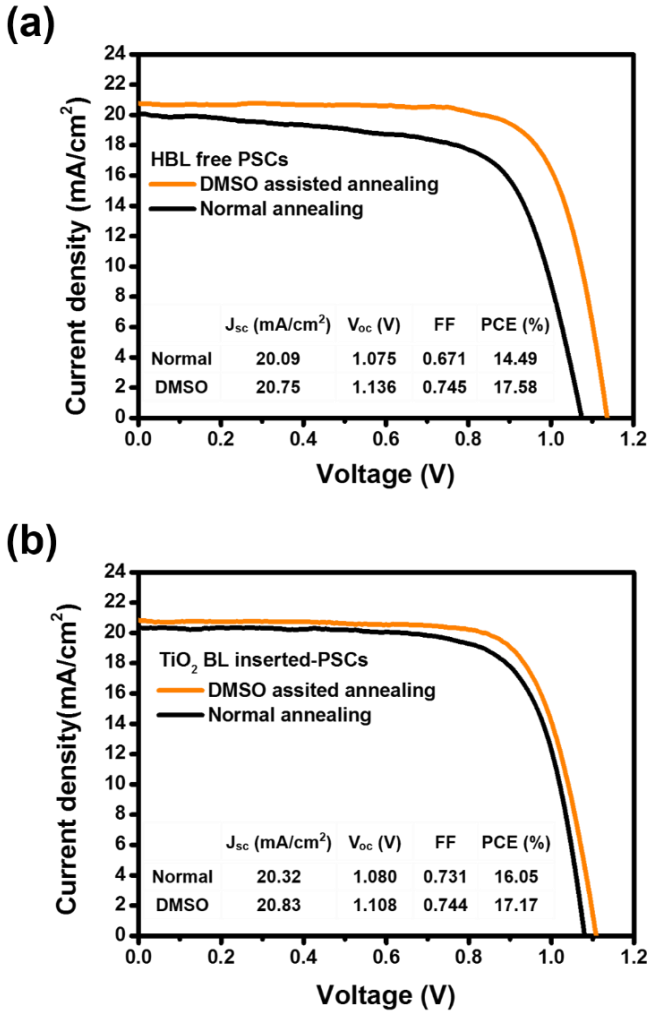

Figure 63. *J-V* characteristics obtained from (a) the HBL free and (b) TiO_2 HBL-inserted PSCs according to annealing method. All PSCs were fabricated with the precursor of 51 wt%. After the DMSO annealing, the PCE of HBL-free PSCs increased by 21 %, while the PCE of TiO_2 HBL inserted-PSCs increased by 7 %.

3.2.5. Interface charge carrier dynamics at the FTO/perovskite

TRPL was explored to monitor the charge transfer properties of $MAPbI_3$ with charge selective layers **(Figure 64a)**; the configuration of the samples was glass/FTO/$MAPbI_3$/spiro-OMeTAD. Carrier lifetime is grain size dependent, becoming longer with increasing precursor concentration because of GB-related defects [156]. When quenching layers were inserted onto the $MAPbI_3$ interface, fast fluorescent quenching occurred and the lifetime dramatically shortened. A bi-exponential decay equation was employed to fit the displayed curves. The calculated decay lifetimes are summarized in **Table 7**. The first exponential part (fast decay) is related to non-radiative recombination (surface properties) and exciton transport to a charge collection layer, and the second part (slow decay) contributes to radiative recombination in the bulk perovskite phase [157-159]. The ratio of W_1, which reflects the charge extraction efficiency, increased with enlarging $MAPbI_3$ grain size. The fast decay time (τ_1) of 3.0 ns for the small grain-based sample (37 wt%) decreased to 0.5 ns for the large grain case (58 wt%). The rate of PL quenching was quickened with increasing $MAPbI_3$ grain size, which was strikingly attributed to the accelerated hole migration at the interface between $MAPbI_3$ and HTM owing to upgraded contact by

surface flatness of $MAPbI_3$ **(Figure 54a-d)** [160]. Further, the free charges might be efficiency extracted in the film having a better quality of perovskite crystallites and low trap density [161].

To support the results of TRPL and comprehend the R_{ct} of identical PSCs, the EIS measurement was conducted under full illumination of simulated solar AM1.5 global light at 100 mW/cm^2 **(Figure 64b)**. The arcs of Nyquist plots recorded in the high-frequency region indicated internal resistance at the FTO/$MAPbI_3$, $MAPbI_3$/HTM, and HTM/Au interfaces [162]. Apart from the HTM/Au interface prepared by an identical process, the arc size of the Nyquist plot could be affected by the contact of the $MAPbI_3$ layer with the HTM or FTO. Small arcs were obtained for the large $MAPbI_3$ grain-based PSCs (51, 58 wt%), which represented excellent charge transfer between the internal layers of the device. In these devices, the electron migration from $MAPbI_3$ to FTO was facilitated because of improved crystallinity and low trap density of perovskite [161]. Furthermore, the HTM was more efficiently deposited on the $MAPbI_3$ films having flat and uniform surface, which accelerated hole-migration into the HTM. From this characterization, it is determined that the current density could be improved by more effective charge transport as well as incident light harvesting level. This EIS result

was consistent with the trends in the TRPL data **(Figure 64b)** and the PV performances.

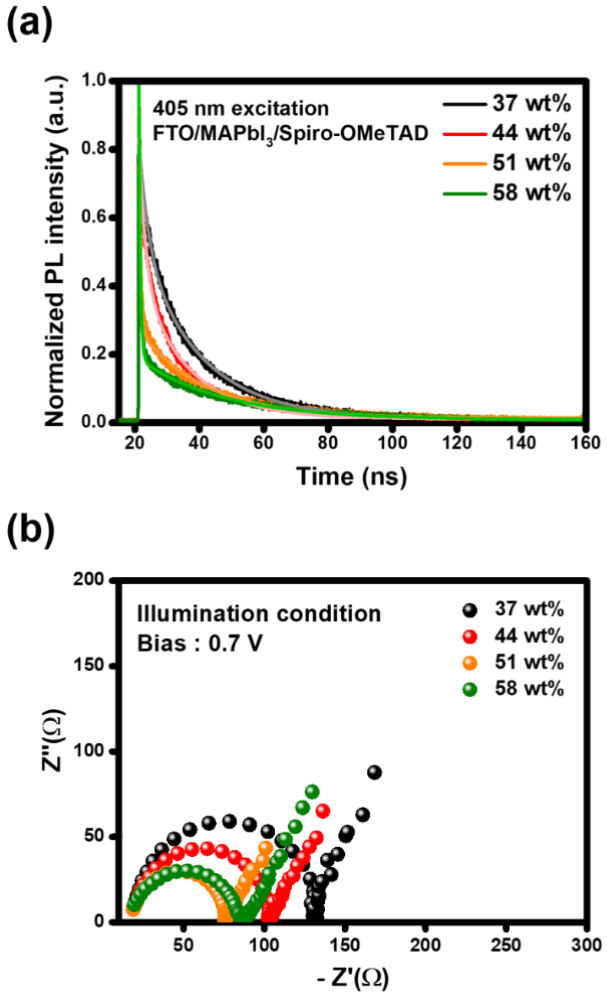

Figure 64. (a) TRPL decay curves for $MAPbI_3$ TFs deposited using various precursor solution concentrations. The sample for time-resolved PL consists of FTO/$MAPbI_3$/spiro-OMeTAD layers. (b) Nyquist plots of the HBL-free PSC as a function of precursor concentration under illumination condition at 0.7 V bias.

Table 7. Summary of time-resolved PL decay parameters evaluated by fitting the raw TRPL curves with bi-exponential decay equation.

Concentration (wt%)	**W_1 (%)**	**W_2 (%)**	**τ_1 (ns)**	**τ_2 (ns)**
37	43.4	56.6	3.0	18.8
44	59.7	40.3	2.1	15.3
51	94.9	5.1	0.5	20.4
58	98.1	1.9	0.5	26.3

3.2.6. Device long-term stability and recyclability

Figure 65 investigates the long-term stability and recyclability of both HBL-free PSCs and TiO_2 HBL-inserted PSCs to suggest the potentiality for commercial application. The HBL-free PSCs had strong durability from attack by sunlight or moisture compared with the TiO_2 HBL-inserted type, and it can be seen that a TiO_2 HBL mainly destroys $MAPbI_3$ at the interface by an UV light-induced photocatalytic effect and trap-charge driven degradation **(Figure 65a)** [62, 163]. After illuminating sunlight on the samples for 6 h, the peak of PbI_2 was soared in case of the TiO_2-inserted sample while there was little change of XRD patterns in the TiO_2-free sample **(Figure 66)**. In addition to long-term stability, it was confirmed that the PCE of HBL-free PSC measured at reverse scan direction was comparable with TiO_2 HBL-inserted PSCs with an augmentation of V_{oc} from 1.09 to 1.12 averagely **(Figure 67)**, even though the photocurrent decreased by low electron extraction rate from perovskite due to large energy barrier between FTO and perovskite [22]. This V_{oc} enhancement was caused by reducing the capacitive current and trapped charges accumulated in defects of TiO_2 HBL, and the static electrons have trouble in jumping over the TiO_2 HBL, which can trigger the unwanted non-radiative recombination and voltage drop

[164, 165]. In case of FF, the distinct gap was not observed in our experiment and the quite high values were obtained in all cases. Consequentially, the superiority of PCE were fluctuated depending on the values of Jsc and Voc, which is meaningful that the performance of HBL-free PSC is quite close to the PCE of HBL-inserted PSC in that the commercialization was innovatively facilitated in terms of production cost and process simplification. For the sake of validating cell recyclability **(Figure 65b)**, the layered thin films were washed off from the completed cells just using DMF, DI water, acetone and 2-propanol, which differed from the previous report in that high temperature calcination process is excluded [166]. The performance of TiO_2-inserted cell was dramatically debased after just one recycle, which was attributed to existence of residual polar protic solvents and PbI_2 on TiO_2 surface [166], whereas the performance of HBL-free cell was equally maintained with that of the initial cell after four recycles **(Figure 68)**. These highly simple and efficient HBL-free PSCs are very suitable to a commercial solar cell model in terms of economic and environmental values.

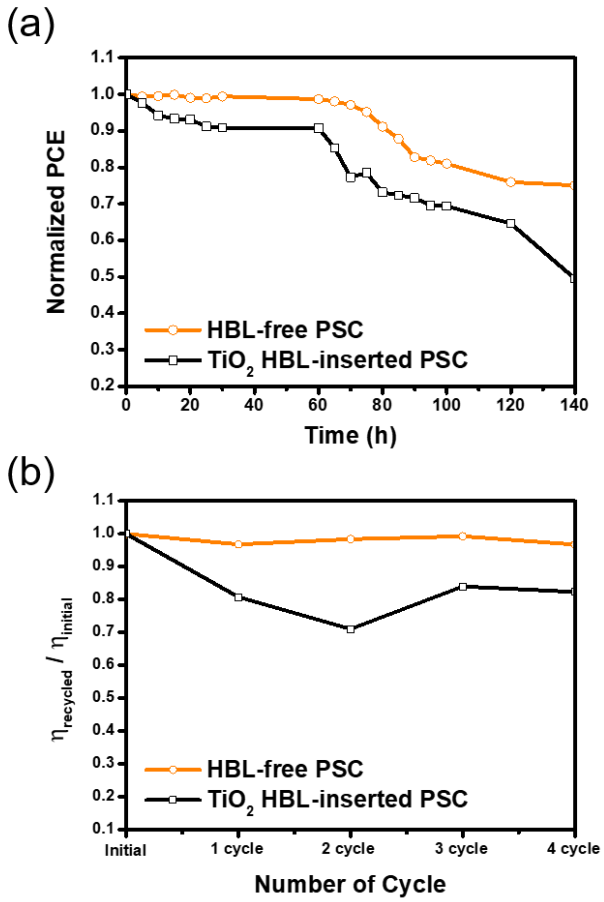

Figure 65. Comparison of (a) long-term stability and (b) recyclability of PSCs fabricated as the HBL-free and TiO_2 HBL-inserted types. All samples were not encapsulated, and the performance was measured without an UV-blocking filter. Long-term stability (air and sunlight) was characterized under ambient condition (25 °C, 35 % RH), and the PCEs obtained at each time point were estimated after sunlight exposure for 7 min.

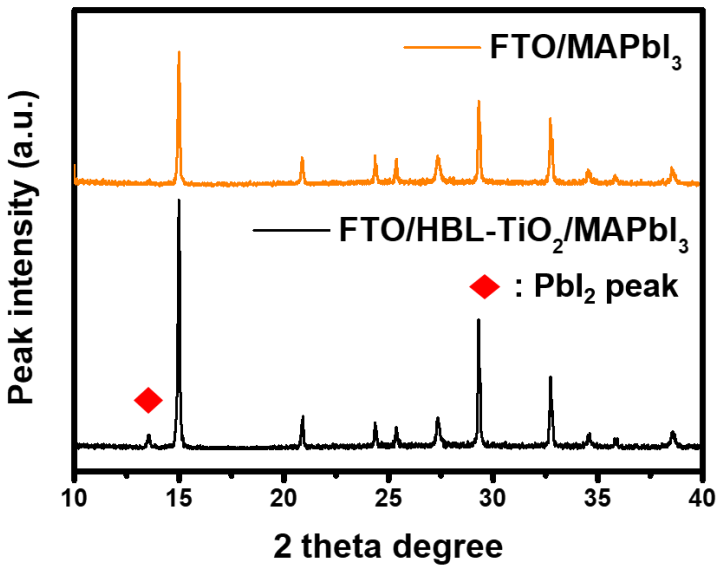

Figure 66. XRD patterns for FTO/$MAPbI_3$ and FTO/TiO_2 HBL/$MAPbI_3$ samples. Before the characterization, these samples were exposed to sunlight for 6 h. The rhombus in the XRD pattern indicates the characteristic peak for PbI_2.

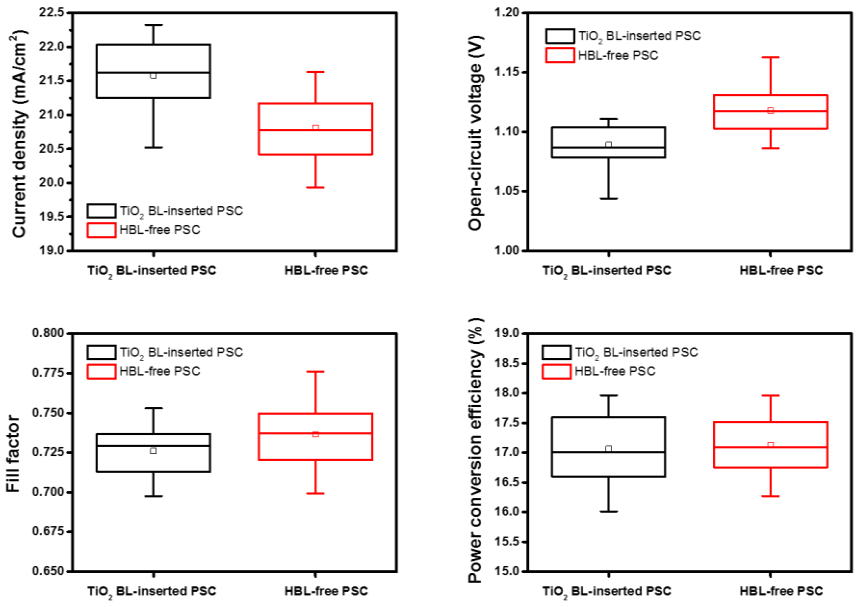

Figure 67. Variation and comparison of the PV parameters obtained from 35 devices fabricated as HBL-free and TiO_2 HBL-inserted types.

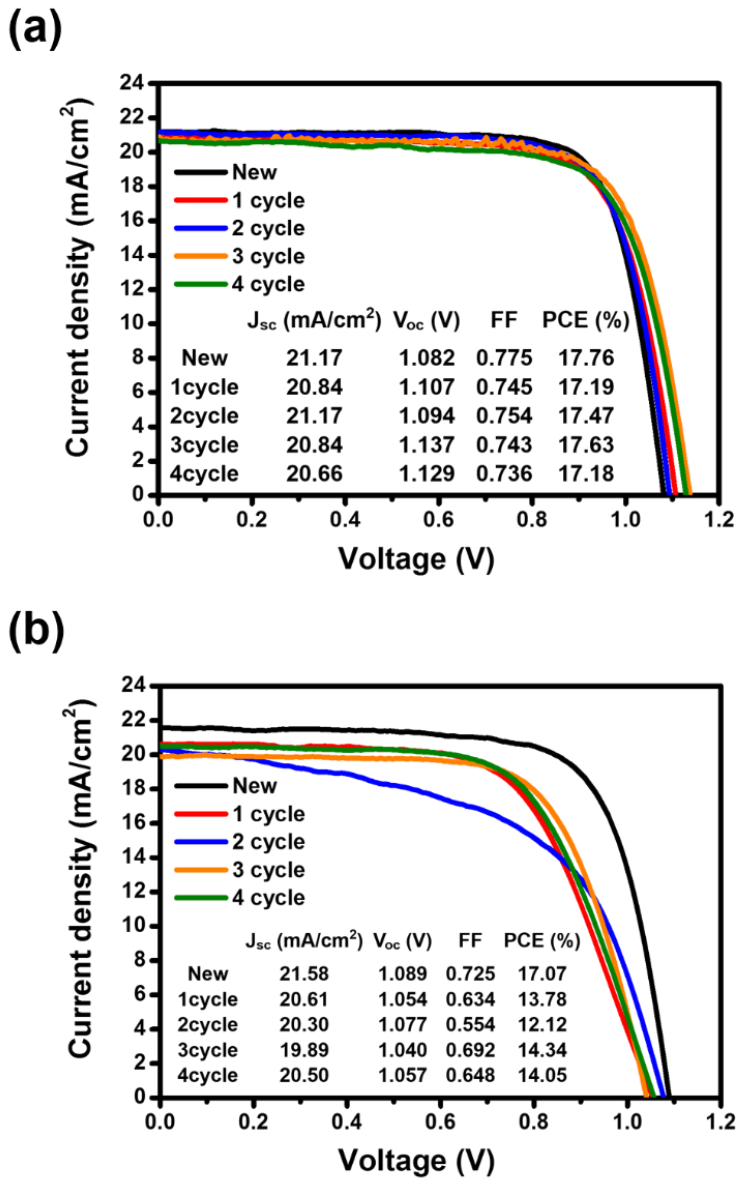

Figure 68. *J–V* curves of the recycled PSCs fabricated as (a) the HBL-free and (b) HBL-inserted types.

3.3. Hierachically porous FTO-based HBL-free PSCs

3.3.1. Morphology and optical properties of FTO substrate

Two types of FTO were prepared to investigate the influence of FTO surface morphology on PV performance. While the pristine FTO (P-FTO) referred to a pure-state of the commercial FTO substrate without any treatment, the hierarchically porous FTO (E-FTO) was fabricated *via* the ECEP. **Figure 69** displays surface FE-SEM images of P- and E-FTO. Notably, the prepared E-FTO featured numerous meso- and macro-pores at the surface, which was intensified with increasing etching time at the fixed voltage **(Figure 70)**. These features differ from those of commercially purchased FTO, whose monotonous surface consists of large, sharp SnO_2 crystals.

The intrinsic properties of E-FTO were compared to those of P-FTO. **Figure 71a** shows the XRD pattern for P-FTO; characteristic peaks for bulk tetragonal cassiterite were displayed at 2θ equal to 27.4, 34.6, 38.8, 52.3, 62.5 and 66.3°, corresponding to the (110), (101), (200), (211), (310) and (301) planes, respectively [167]. These approximately matched those of E-FTO, which suggested that there would be little difference in crystalliinty of the two FTOs. Their *I–V* characteristics, displayed in **Figure 71b**, demonstrated the same conductivity before and after surface

etching without a critical reduction in thickness of FTO **(Figure 72)**.

Figure 73a plots the UV-Vis transmittance spectrum of each FTO; digital images of the P- and E-FTO are inset. The transmittance of E-FTO was lower than that of P-FTO due to augmented light scattering at the surface from various-sized pores; this is in qualitative agreement with previous reports [114]. The scattering effect in the E-FTO/$MAPbI_3$ sample was ascertained by UV-Vis diffuse reflectance spectroscopy over the range of 400 to 800 nm **(Figure 73b)**. The introduced light was scattered by the E-FTO surface pores adjacent to the bottommost perovskite, thus extending the light path length and the light-soaking efficiency through optical confinement **(Figure 74)** [168, 169]. The result was evident in the UV-Vis light-harvesting efficiency of the perovskite, in which the light absorption was more intense in the E-FTO-based sample (E-FTO/$MAPbI_3$) compared with the P-FTO-based sample **(Figure 73c)**. Thus, the enhancement of light-absorption by scattering effect counterbalanced the slightly decreased light transmittance after etching.

To further scrutinize differences in surface area, a dye adsorption/desorption measurement was conducted on each FTO **(Figure 75)**. The detailed processes were described in **2.3.3 section**, and

results were tabulated in **Table 8**. The extent of adsorption of D719 on each FTO was elevated approximately tenfold after etching (E-FTO) due to the creation of macro- and meso-pores at the surface. This significant finding impacted device performance because the electron migration rate is crucially affected by the contact at the FTO/perovskite interface. Furthermore, it was speculated that the E-FTO-based PSC was comparable to the mesostructured-type of PSC, in that the electron injection area and rate increased by introducing an n-type metal oxide nanoparticle-based MPL. Fluorine-doped SnO_2 (SnO_2:F) nanoparticles were produced by the etching process in the top layer of E-FTO **(Figure 76)**; better adherence was expected for perovskite due to the increased contact area from the SnO_2:F nanoparticle layer.

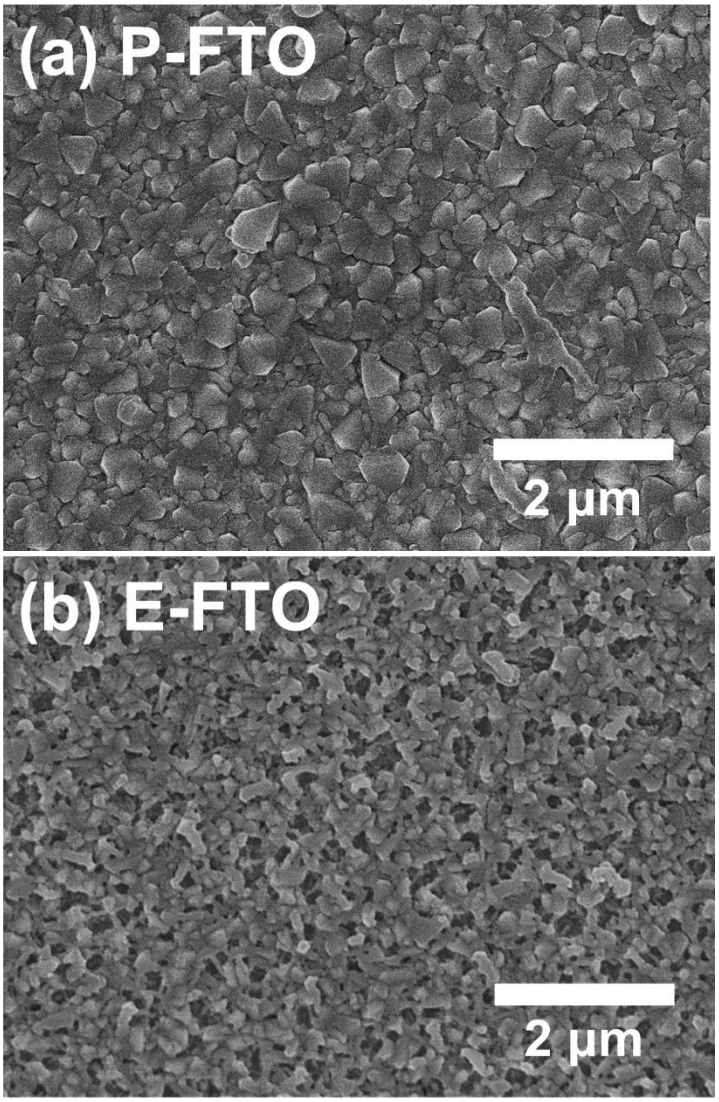

Figure 69. Surface FE-SEM images of (a) P-FTO and (b) E-FTO.

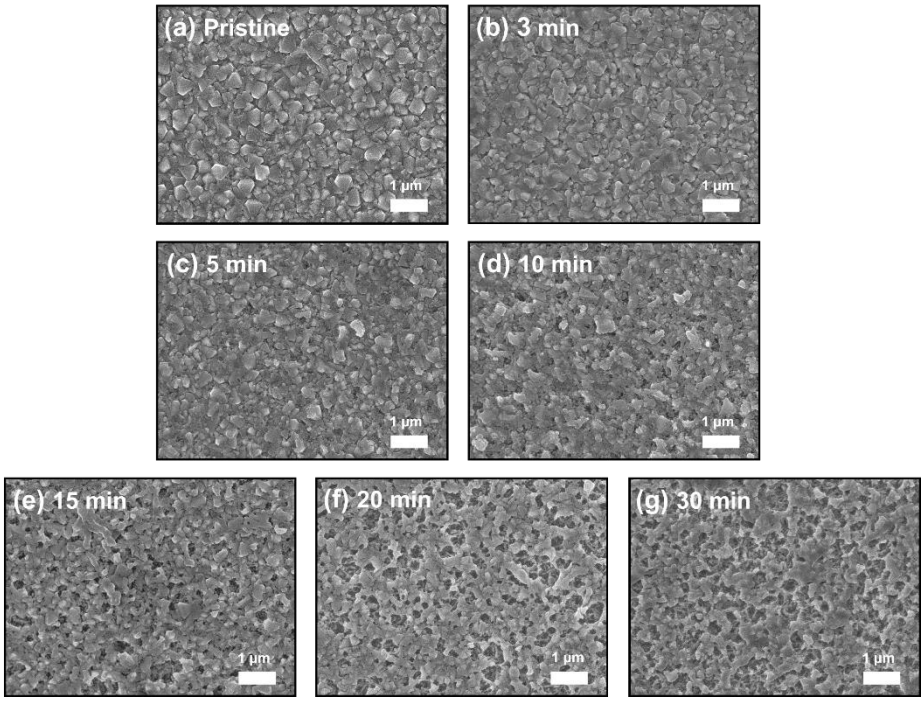

Figure 70. Changes in the FTO surface as a function of electrochemical etching time for 0 – 30 min (a-g). The etching was done in an electrolyte composed of 1 M aqueous HCl solution with 0.02 M zinc acetate solution.

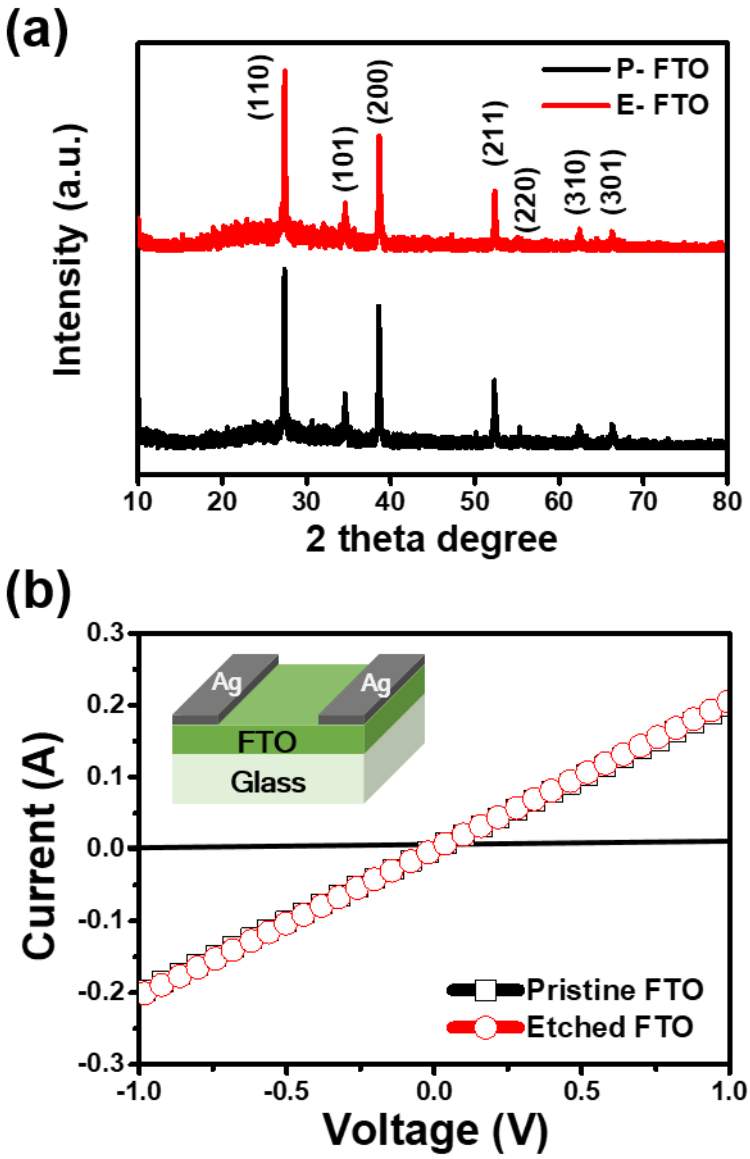

Figure 71. (a) XRD patterns of P- and E-FTO. (b) *I–V* curve of the dummy cells with a structure of glass/P- and E-FTO/Ag electrode.

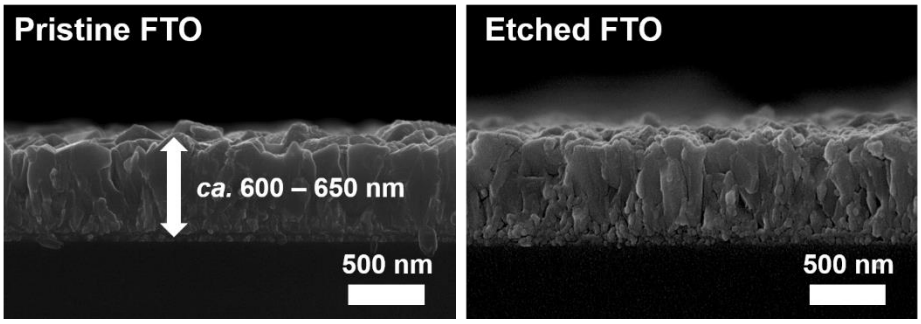

Figure 72. Cross-sectional FE-SEM images that compare the thickness of P-FTO and E-FTO. The average thickness of P-FTO of *ca.* 600 – 650 nm was not significantly different from that of E-FTO.

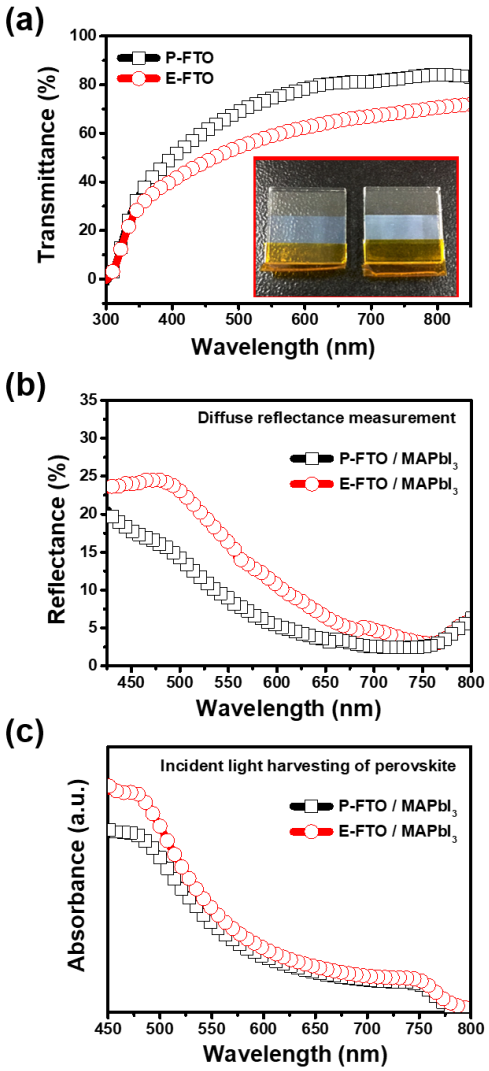

Figure 73. (a) UV-Vis light transmission efficiency and (b) UV-Vis diffuse-reflectance spectra of P- and E-FTO. (c) UV-Vis light absorption spectra of MAPbI3 deposited on P- and E-FTO. The E-FTO used for all of these characterizations was formed using optimal etching conditions (15 min).

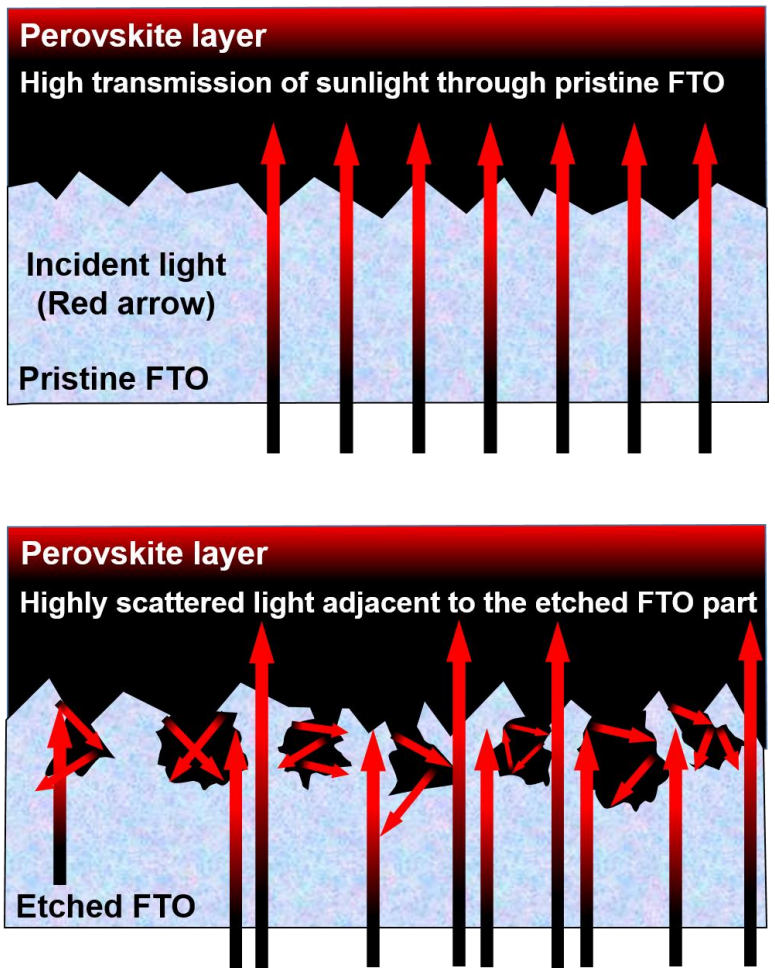

Figure 74. Schematic diagram of the light transmission and light scattering effects in the PSCs fabricated with P- and E-FTO substrates. The incident light was more easily transmitted in the P-FTO-based PSC case. The incident light was highly scattered mostly adjacent to the etched parts of E-FTO; additional light absorption by the perovskite would be possible in these regions.

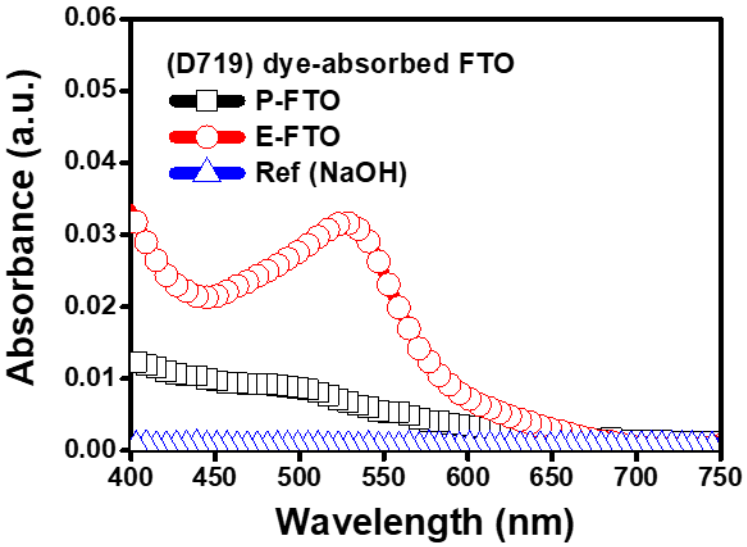

Figure 75. UV-Vis incident light absorption spectra by the adsorbed dyes on P- and E-FTO. 0.25 mM dye solution was used to adsorb dye on the substrate. The desorption process was carried out using 0.01 M NaOH solution.

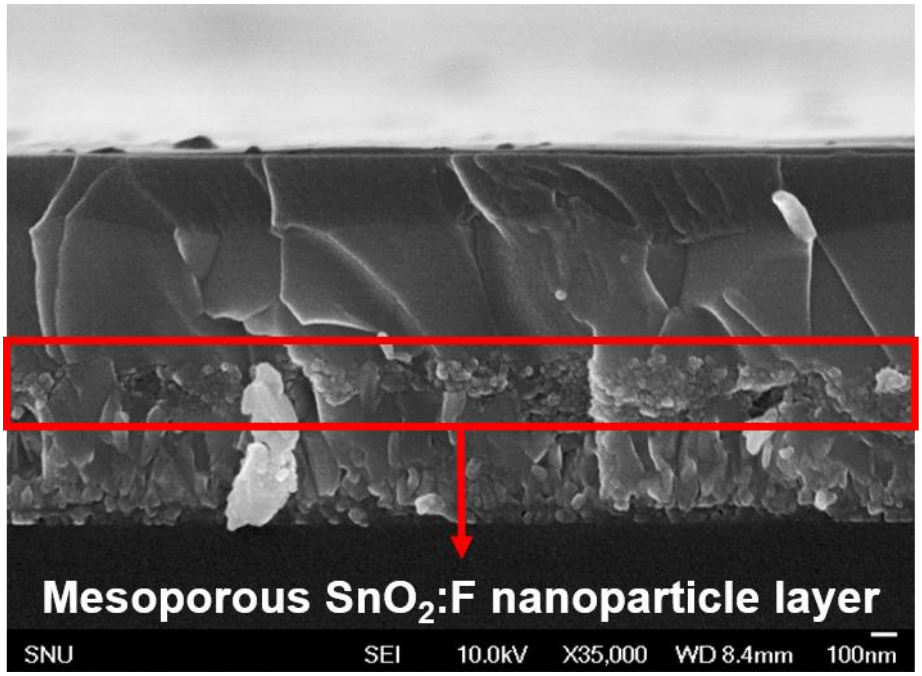

Figure 76. Cross-sectional FE-SEM image of the E-FTO-based PSC. The ECEP produced a mesoporous SnO_2 layer composed of SnO_2 nanoparticles at the top of the FTO. The perovskite penetrated into every feature of the mesoporous SnO_2 region.

Table 8. Parameters used to calculate the roughness factor. The roughness factor was measured by the dye adsorption/desorption method.

	Pristine FTO	**Etched FTO**
Concentration of dye (M)	6.73×10^{-10}	6.82×10^{-9}
Number of dye molecule	4.05×10^{14}	4.11×10^{15}
Real surface area (m^2)	6.68×10^{-4}	6.78×10^{-3}
Roughness factor	1.3365	13.536

3.3.2. Photovoltaic performance of the HBL-free PSCs

The E-FTO substrate was employed as an anode; the perovskite and the spiro-OMeTAD were deposited consecutively on the substrate as the photon-absorber and HTL, respectively. Finally, the device was capped with a thermally deposited 60-nm-thick Au layer **(Figure 77a)**. As noted above in **3.3.1 section**, the E-FTO somewhat resembles the metal oxide nanoparticle-based MPL in the conventional PSC, used to facilitate charge transport [107]. Building on this perspective, it was predicted that by using E-FTO in a PSC, a greater number of photo-excited electrons would be quickly transferred to the anode due to the increased contact surface area between the perovskite and the FTO **(Figure 77b)**. As expected, the E-FTO-based PSC notably outperformed the P-FTO-based PSC under optimized etching conditions (etching for 15 min). J_{sc} increased from 20.16 to 22.46 mA/cm^2 **(Figure 78a)**, most likely due to the improved electron extraction ability of E-FTO. This result was confirmed by the IPCE spectra, where each integrated J_{sc} was in good agreement with *J–V* results **(Figure 78b)**. The IPCE spectra showed an improvement over the entire range of the spectrum (from 400 to 800 nm), which further indicated that the free electrons were more quickly and efficiently injected into the E-FTO from the perovskite [170].

Furthermore, this IPCE enhancement, especially at longer wavelength (650 – 800 nm), was ascribed to additional light absorption of perovskite, caused by the scattering effect at the E-FTO surface [171, 172]. However, the immoderate etching on FTO deteriorates device performance due to a reduction in conductivity of FTO **(Figure 79)**.

The average PV performance achieved from 32 P- and E-FTO-based PSCs was compared to demonstrate the reliability of this design **(Figure 80, Table 9).** Replacing the P-FTO with E-FTO caused the average J_{sc} to increase markedly from *ca*. 20.3 to 21.7 mA/cm^2 with only small variation, and the V_{oc} to decrease exiguously from *ca*. 1.125 to 1.115 V. The increment in J_{sc} was attributed to facilitation of charge extraction through surface area enhancement, better wettability, and improved light scattering. To figure out more dominant factor for an increase in current density among various causes, the TiO_2 HBL inserted-PSCs were fabricated using P- and E-FTO. This eliminates the effects of precursor spreadability and reduces the light scattering effect, and allows to roughly analyze the impact of increasing interface areas. As shown in **Figure 81**, the J_{sc} of 1.1 mA/cm^2 increased with replacement of P-FTO with E-FTO, which is *ca*. 78 % increase rate compared with the J_{sc} increment of *ca*. 1.5 mA/cm^2 in HBL-free PSC. It indicates that the

dominant factor for J_{sc} increment may be fast extraction of electrons into the electrode due to the augmentation of the interfacial area. The changes in V_{oc} were determined by the intrinsic properties of the FTO and the perovskite crystallized on the different substrates. A perovskite-induced change to the V_{oc} can be neglected because XRD measurements revealed similar perovskite crystallinity for the two cases **(Figure 82)**. UPS analysis suggested that the tiny reduction in V_{oc} of E-FTO-based PSCs stemmed from the decrease in the WF from −4.4 eV to −4.7 eV with FTO etching **(Figure 83)**. The energy barrier between the perovskite and FTO increased by introducing E-FTO to the device, which impeded electron transfer; this allowed electrons to accumulate at the FTO surface, leading to subsequent interfacial recombination [104, 151, 173]. However, the PCE of the E-FTO-based device was greatly improved due to the outstanding J_{sc}, despite the disturbance of charge migration induced by the energy barrier that caused the slight V_{oc} drop. Therefore, the WF-induced deterioration was nearly offset in this design.

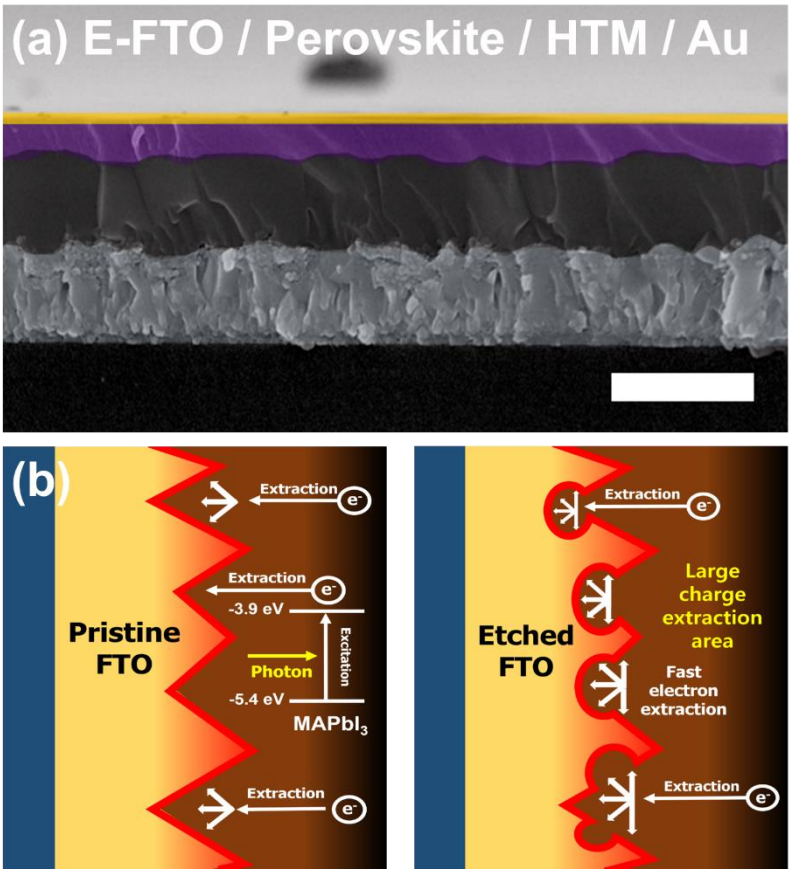

Figure 77. (a) Cross-sectional FE-SEM images of the E-FTO-based PSC. (b) Illustration of the extraction behavior of photo-excited electrons from perovskite into the FTO. The charges quickly accumulated at the interface between the E-FTO and perovskite due to the larger charge contact area of the E-FTO compared with the P-FTO.

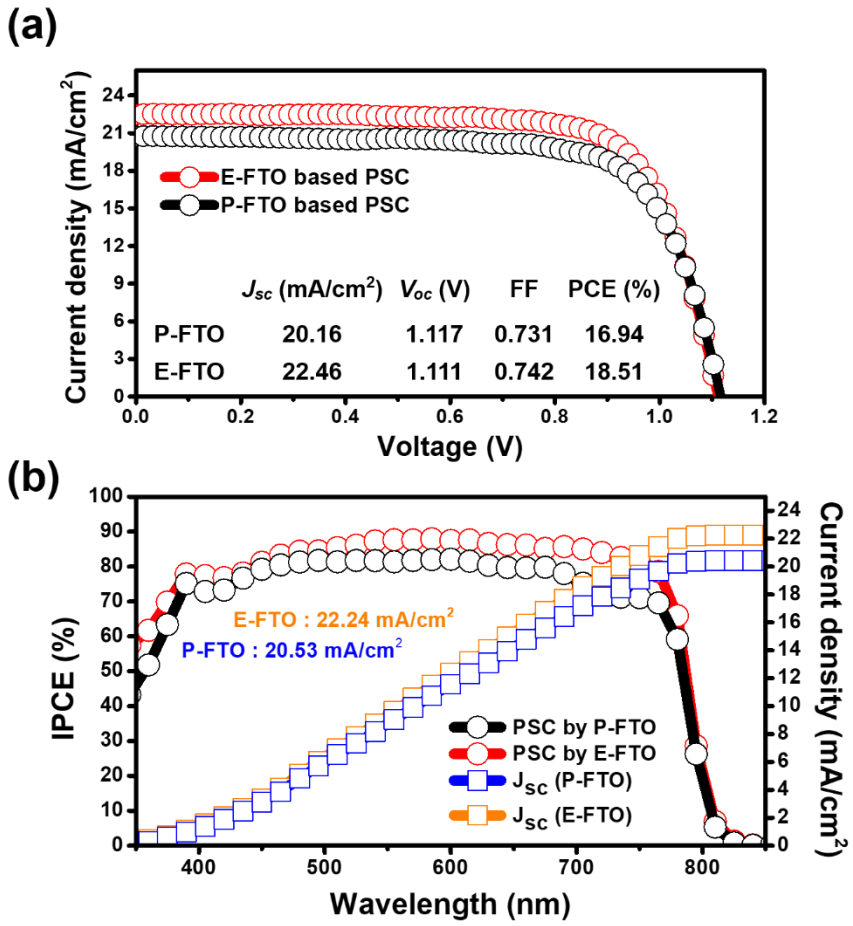

Figure 78. (a) *J–V* characteristics and (b) IPCE spectra of E-FTO- and P-FTO-based PSCs.

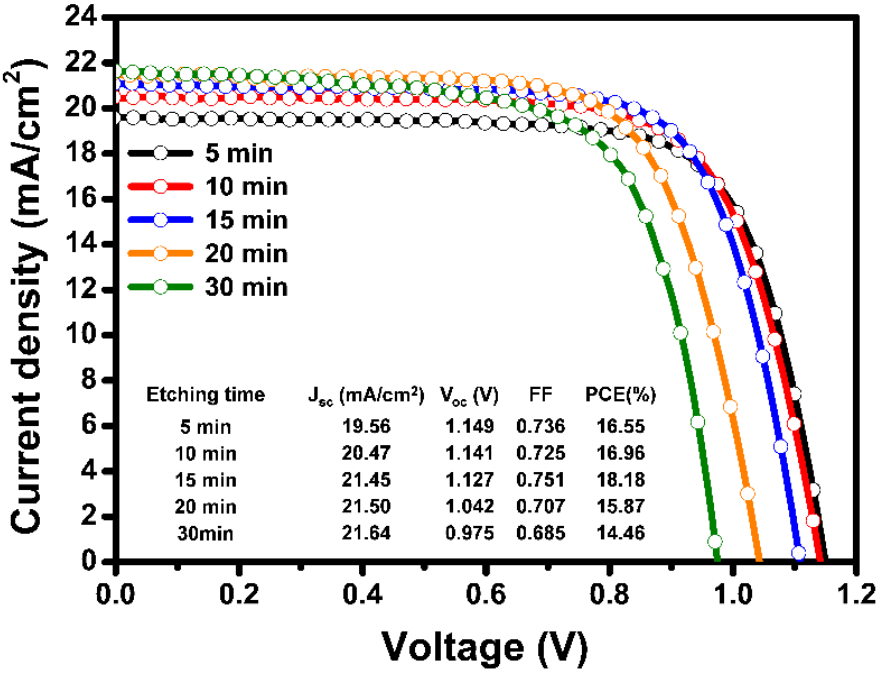

Figure 79. *J–V* curves of E-FTO-based PSCs as a function of the ECEP time.

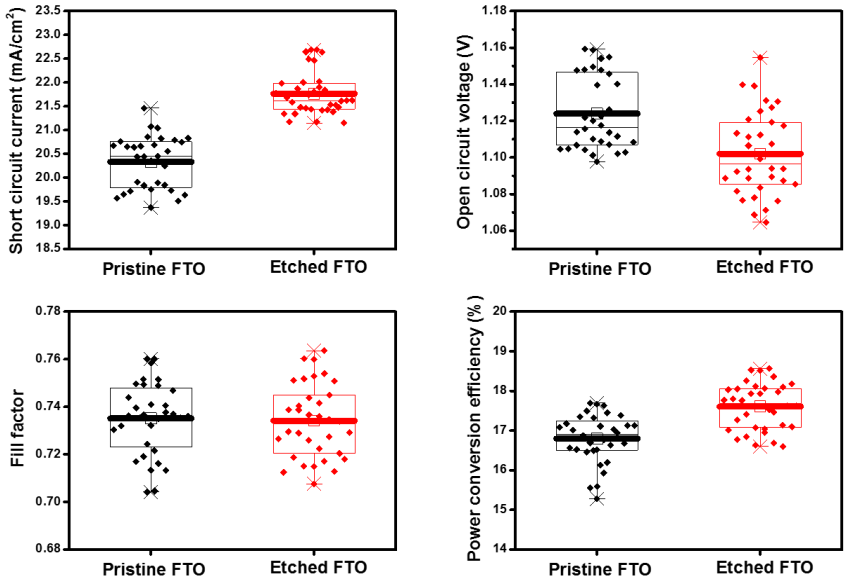

Figure 80. Distribution of the PV performance parameters evaluated from 32 devices based on P-FTO and E-FTO under AM 1.5 radiation and ambient conditions. The E-FTO-based PSCs exhibited a superior photocurrent compared with the P-FTO-based PSCs, while the V_{oc} was slightly higher for the P-FTO-based PSCs. Both types had similar fill factors. E-FTO-based PSCs exhibited better PCE.

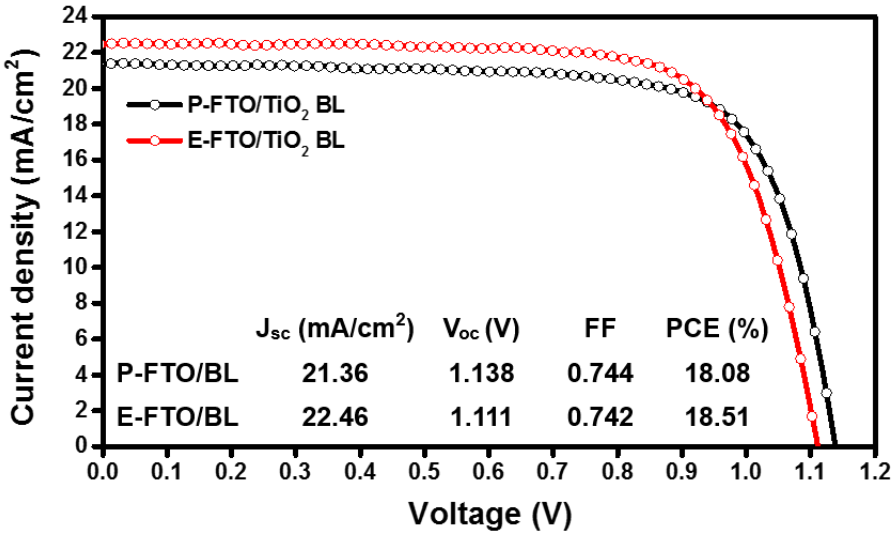

Figure 81. *J-V* curves for P- and E-FTO based PSC including 50 nm-TiO_2 HBL on each FTO.

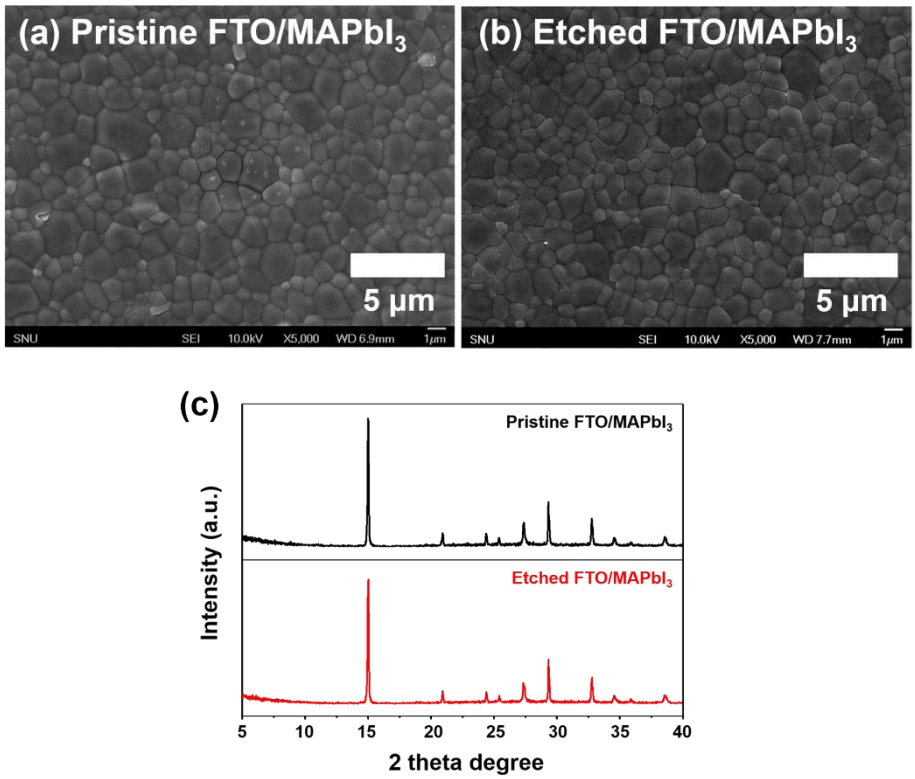

Figure 82. FE-SEM images of $MAPbI_3$ surface-coated on (a) P- and (b) E-FTO. (c) XRD patterns of the $MAPbI_3$ films.

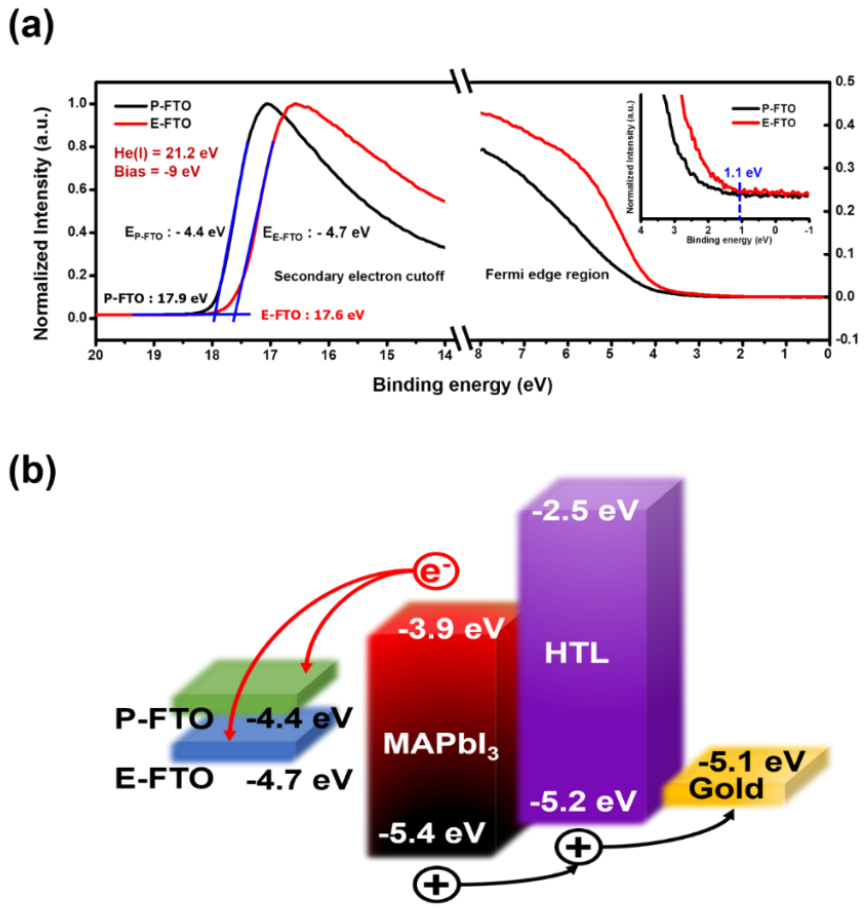

Figure 83. (a) UPS spectra of P- and E-FTO. The secondary electron cutoff and Fermi edge region are shown to the left and right sides of the figure, respectively. (b) Energy-band diagram of the HBL-free PSC with identical HTL and gold electrodes differing only by FTO type. The penetrated photons formed numerous electron–hole pairs that were separated by charge-selective layers such as FTO and the HTL

Table 9. Average PV performance parameters evaluated from 32 HBL-free type devices measured under 100 mW/cm of simulated AM1.5G illumination. The substrate was either P-FTO or E-FTO. P-FTO: pristine fluorine-doped tin oxide; E-FTO: etched FTO.

Type of substrate	J_{sc} **(mA cm^{-2})**	V_{oc} **(V)**	***FF***	η_{avg} **(%)**
P-FTO	20.33 ± 1.04	1.124 ± 0.028	0.735 ± 0.028	16.80 ± 1.07
E-FTO	21.76 ± 0.77	1.102 ± 0.034	0.734 ± 0.027	17.61 ± 0.97

η_{avg}: average power conversion efficiency.

3.3.3. Interface charge carrier dynamics at the E-FTO/perovskite

To unearth the change in charge carrier dynamics at the interface FTO/perovskite, steady-state photoluminescence (SSPL) and TRPL analyses, which have been used to reveal the dynamics of charge transfer [135], were carried out for P- and E-FTO/$MAPbI_3$/PMMA and glass/$MAPbI_3$/PMMA samples **(Figure 84a and 84b)**. For both cases, the inserted electron extraction layer (FTO) quickly quenched the PL signal by decreasing recombination. Also, it was evident from the SSPL and TRPL measurements that the rate of PL quenching was faster after the fabrication with E-FTO. The resulting TRPL curves for each sample were fitted using a bi-exponential decay equation, and related parameters are summarized in **Table 10**. The fast decay part (W_1, τ_1) is involved in non-radiative recombination and electron transport to the FTO in this experiment and the slow decay part (W_2, τ_2) mirrors the radiative recombination in the bulk perovskite [174]. The fast decay part was focused to compare the charge migration efficiency as a function of the surface morphology of the FTO. The PL decay time of 45.55 ns for the glass/$MAPbI_3$/PMMA sample is in reasonable agreement with previous reports [135]. The PL decay time of the P-FTO-based sample with a τ_1 of 4.662 ns and τ_2 of 15.45 ns decreased to a τ_1 of 2.502 ns and τ_2 of 9.931

ns for the E-FTO-based sample. Also, the fast decay weight fraction soared from 33 to 65 % after etching. This finding confirmed that the photo-excited electrons remaining in the perovskite phase were extracted more quickly to E-FTO compared with P-FTO, due to the higher surface area of E-FTO stemming from numerous pores. And it proved that faster PL quenching was predominantly triggered by improved charge transport behavior to the FTO [109, 175, 176].

FS-TA spectroscopy was additionally used to further reinforce the PL measurement results and to better understand the photo-induced free charge carrier dynamics **(Figure 84c)** [158]. This measurement is frequently used in PSC research to monitor the conductivity of free-electron injection into a charge-accepting layer [61, 137]. In our experiment, the time-dependent FS-TA measurement was probed using only the 745 nm photobleaching band to clarify the excellent electron evulsion ability of the E-FTO. The normalized transient decay curves were well-fitted to a single exponential decay equation with a time constant of 171.9 and 146.2 ps for the P-FTO- and the E-FTO-based samples, respectively. The decreased decay time constant after FTO surface etching is consistent with the TRPL findings shown in **Figure 84b** [137].

Moreover, the smaller water contact angle for the E-FTO than P-FTO **(Figure 85)** suggested that charge collection may improve as a result of better surface wettability of the perovskite precursor on the E-FTO and the good adhesion between the perovskite and the FTO [104, 177]. The more efficient spreadability on the E-FTO over P-FTO was induced from the decreased surface tension of the FTO surface after etching, rather than an influence of surface functional groups **(Figure 86)**. The small fluorine-doped SnO_2 (SnO_2:F) nanoparticles that decomposed from large SnO_2:F crystals during the etching process had low surface tension and high surface free energy compared with the large SnO_2:F crystals; thus, the affinity of the perovskite with the E-FTO surface should be enhanced [178-180].

Figure 87 indicates the EIS result recorded under the illumination condition that compares the R_{ct} at each interface in the PSC [181, 182]. The difference of the resistance shown in Nyquist plots of P- and E-FTO-based devices was rooted in the FTO/perovskite interface. The extent of R_{ct} at the FTO/perovskite interface is determined by the main arc size. The E-FTO-based PSC gave a smaller arc than the P-FTO-based PSC, which signified that the unbound charges in the perovskite could shift more easily to E-FTO due to lower interface resistance.

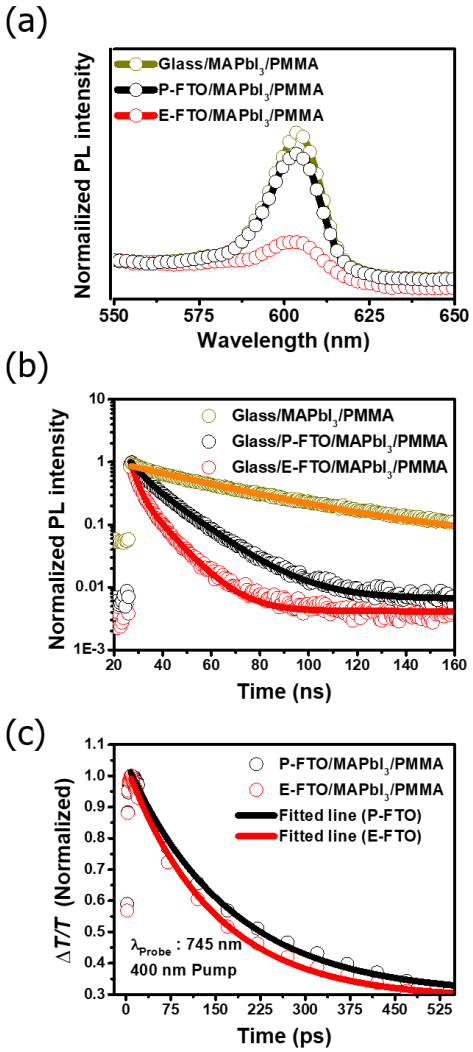

Figure 84. (a) SSPL and (b) TRPL decay curves for $MAPbI_3$ deposited on the P- and E-FTO. The excitation wavelength was 405 nm, and fluorescence after 750 nm was detected using 750 nm long pass filter. (c) FS-TA profile recorded following 400 nm excitation of $MAPbI_3$ prepared on the P- and E-FTO substrates.

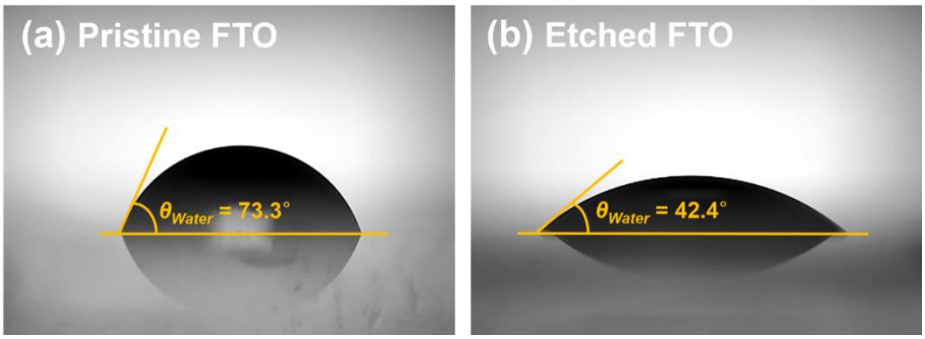

Figure 85. Water contact angle test of (a) P- and (b) E-FTO was conducted after cleaning the FTO substrates consecutively with DI-water, acetone, and 2-propanol.

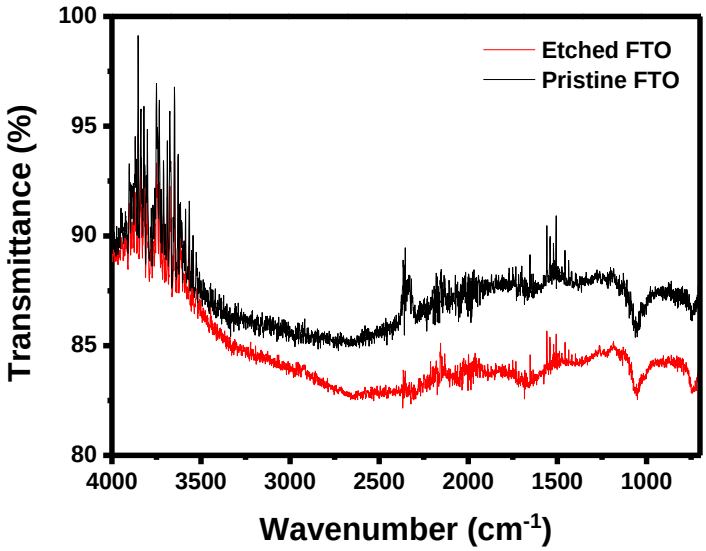

Figure 86. Fourier transform-infrared spectra of the P- and E-FTO.

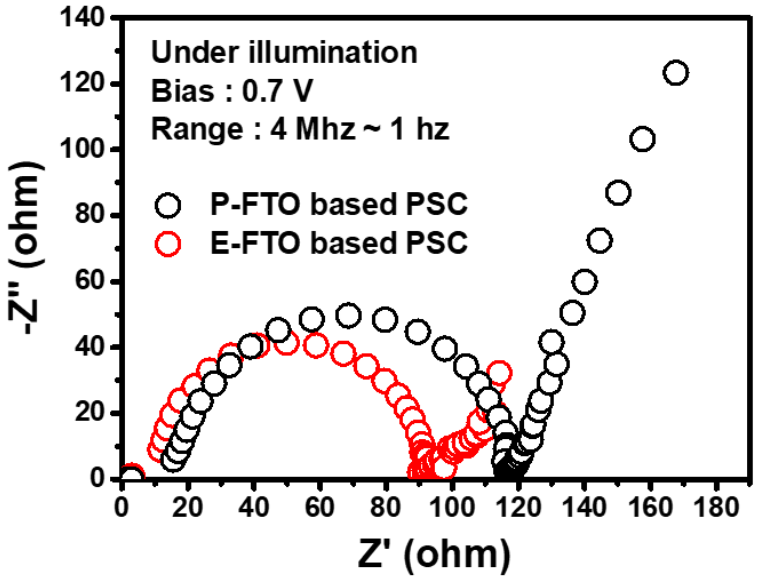

Figure 87. Nyquist plots measured under illumination of the PSCs fabricated using the P- and E-FTO substrates.

Table 10. TRPL decay parameters for P- and E-FTO- /$MAPbI_3$/PMMA samples determined by fitting the curves using the bi-exponential equation. The glass/$MAPbI_3$/PMMA sample was fitted by a single exponential decay equation. P-FTO: pristine fluorine-doped tin oxide; E-FTO: etched FTO;

	W_1	W_2	τ_1	τ_2	$W_1/(W_1+W_2)$	τ_{avg}[a]
Glass	0.9077	-	45.6	-	-	-
Pristine FTO	0.3338	0.6638	4.7	15.5	0.3346	14.0
Etched FTO	0.7006	0.3681	2.5	9.9	0.6555	7.5

a) $\tau_{avg} = \sum_i W_i \tau_i^2 / \sum_i W_i \tau_i$

3.3.4. Device hysteresis and long-term stability

Figure 88a and **Table 11** compare the extent of the hysteresis for P- and E-FTO-based PSCs. The P-FTO-based PSC showed a large degree of hysteresis, in which the PCE of 17.18 % dropped sharply to 12.77 % with a major decrease in V_{oc} and FF when the scan direction was reversed. The absence of HBL meant that electron accumulation in the perovskite was severe and led to an unbalanced charge flux between FTO/perovskite and perovskite/HTL interfaces, engendering serious hysteresis [115, 183]. However, in the case of the E-FTO-based PSC, the PCE of 18.15 % decreased to 15.51 % with changing scan direction due to a smaller decline in V_{oc} and FF than occurred with the P-FTO-based PSC. This indisputable mitigation of hysteresis of the E-FTO-based PSC was attributed to fast electron injection into E-FTO. The porous structure of the E-FTO increased the contact area between the perovskite and the E-FTO, which diminished the accumulated charge and hysteresis. The stabilized PCE of 16.33 % was yielded with steady-state photocurrent of 17.85 mA/cm^2 at a maximum power point (V_{max}) of 0.915 V **(Figure 88b)**, which is in good agreement with the hysteresis result. It implies that the hysteretic behavior could be relieved significantly by introducing the E-FTO.

Figure 89a exhibits that the best PCE of 19.22 % of E-FTO-based HBL-free PSCs, achieved under optimal conditions, had the J_{sc} of 22.81 mA/cm^2, V_{oc} of 1.123 V, and FF of 0.750. Also, the SPO and stabilized photocurrent density were 17.16 % and 18.51 mA/cm^2 respectively at V_{max} of 0.927 V **(Figure 89b)**. The performance of this PSC was continually maintained to 300 h with minimal degeneration in an ambient environment (25 °C, 30 % RH) without encapsulation, which indicated the great air stability of the device **(Figure 90a)**. Furthermore, the photostability test between P- and E-FTO based PSC was conducted under constant AM 1.5G illumination and 35% RH **(Figure 90b)**. The PCE of P-FTO based PSC significantly deteriorated to *ca* 10 % of its original value after 210 min of light exposure. However, the PCE of E-FTO-based PSC remained *ca* 85% even after 240 min. The PCE was sharply degraded to 30 % of initial value after 270 min of light exposure. Photostability is affected by the density of carrier trap sites inside perovskite and light-activated meta-stable trap states produced by photo-generation of polaronic states, which was demonstrated by Tsi. and Nie. et al [184, 185]. In addition, the local electric field generated by trapped charges adjacent to HBL/perovskite interface drives injurious photostability of PSC [62]. The meta-stable trap states and charges

accumulation would be particularly concentrated close to FTO/perovskite interface [186]. In our case, the charge extraction rate at E-FTO/perovskite was faster than P-FTO/perovskite without severe accumulation, the density of trapped charge shrunk at E-FTO/perovskite interface, which might prevent irreversible degradation of perovskite. Additionally, it was found that the assembled PSCs could be re-used at the end of their lifetimes by simply rinsing the cells with DMF, water, acetone, and 2-propanol, with sonication for 20 min **(Figure 91)**. The performance of the recycled PSCs was excellent irrespective of the number of recycles, although it slightly varied depending on the environmental conditions used for the fabrication process. The excellent recyclability will help to reduce industrial waste and production costs.

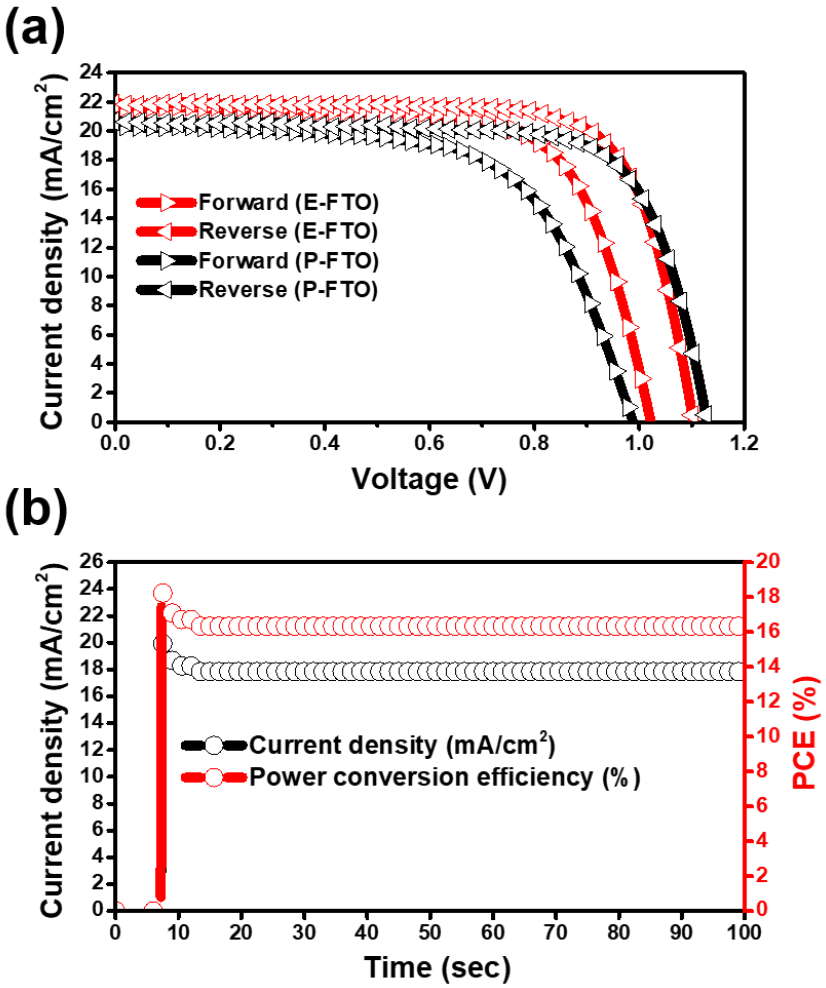

Figure 88. (a) Comparison of the *J-V* hysteresis of the E-FTO-based PSC with that of the P-FTO-based PSC. (b) Stabilized photocurrent and PCE of E-FTO based PSC, obtained from a maximum power point of 0.915 V.

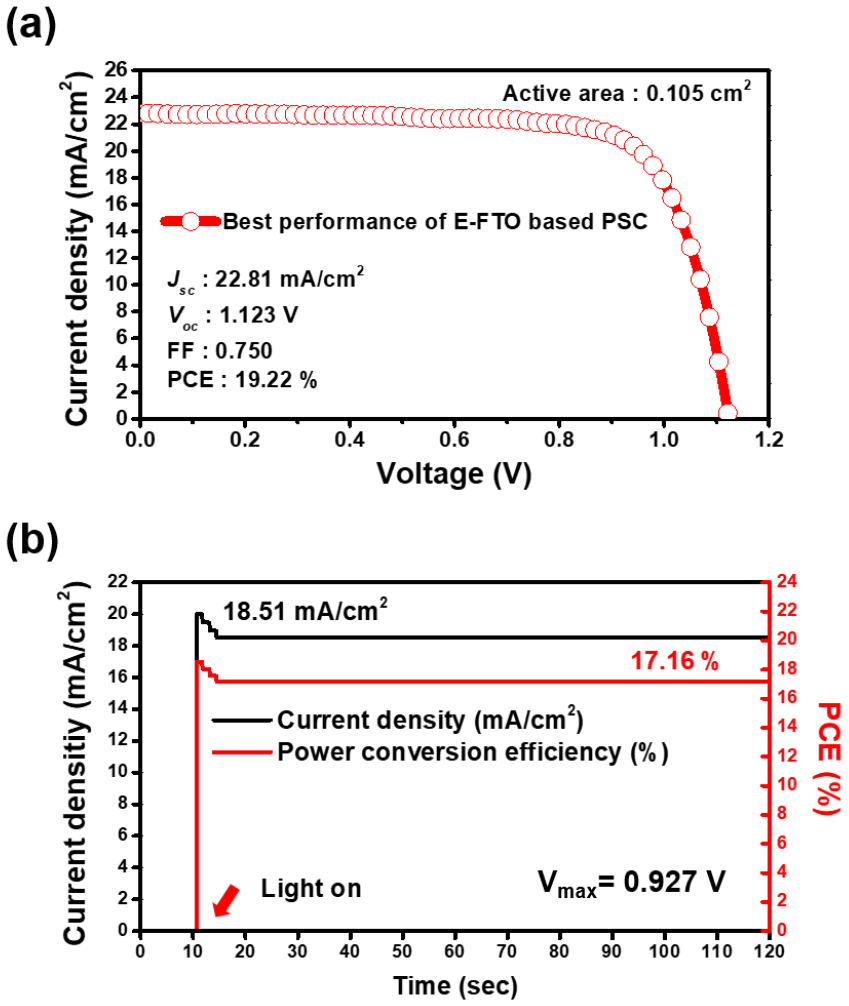

Figure 89. (a) The E-FTO-based PSC with the highest PCE when measured in ambient air. (b) Stabilized photocurrent and PCE of champion cell measured at a maximum power point of 0.927 V.

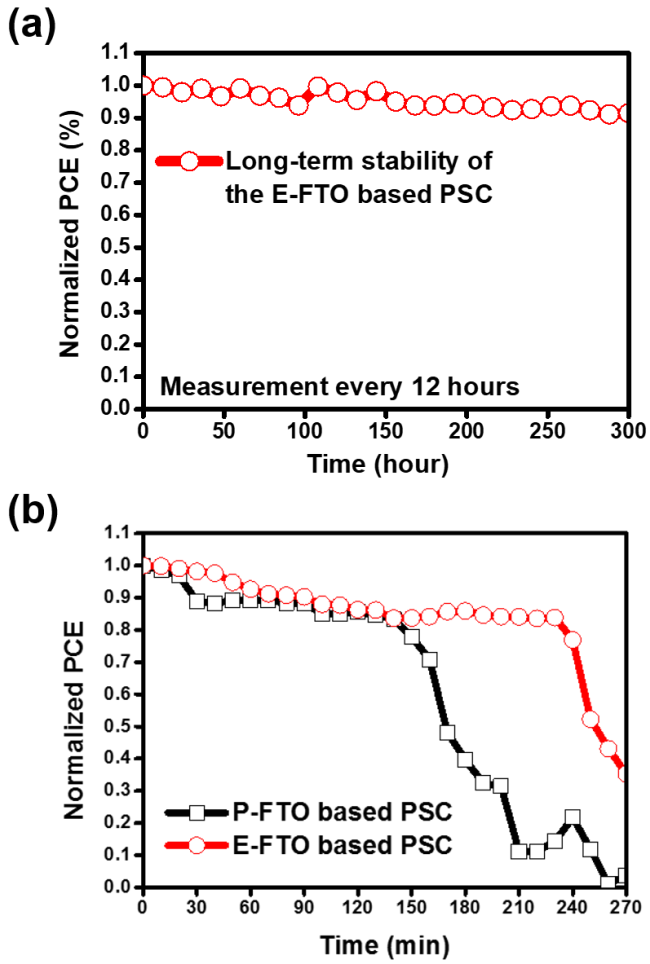

Figure 90. (a) Long-term stability in ambient air (25°C, 30 % RH). (b) Recyclablity testing of the E-FTO-based PSC. No samples were encapsulated, and the performance was measured without a UV-blocking filter. Photostability test results obtained from P- and E-FTO based PSCs, which was measured under constant AM 1.5G illumination and 35 % RH for 270 min.

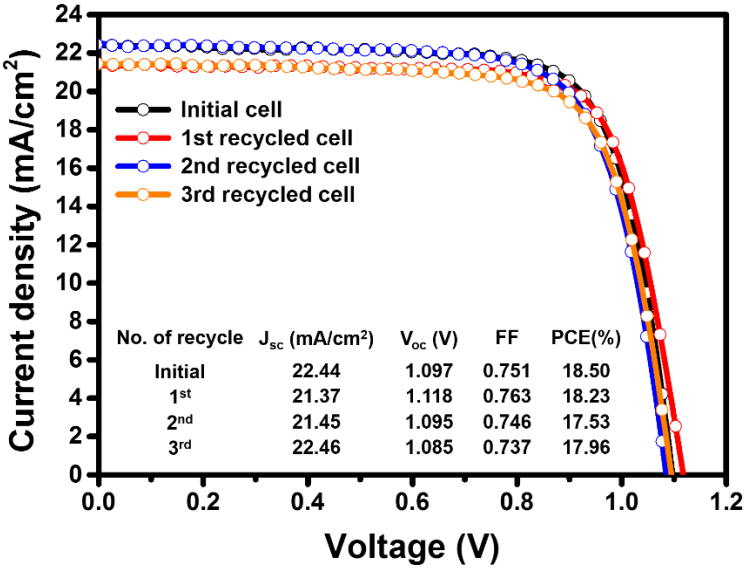

Figure 91. Recyclability of E-FTO-based HBL-free PSCs. The initial cell was re-used through rinsing the cell using DMF, distilled water, acetone, and 2-propanol with sonication for 20 min.

Table 11. The PV performance of P-FTO and E-FTO-based PSCs comparing their hysteretic behaviors. The values correspond to the J–V curves shown in **Figure 88a**.

Substrate	J_{sc} (mA cm^{-2})	V_{oc} (V)	*FF*	η (%)
(P-FTO) Forward	20.37	0.988	0.634	12.77
(P-FTO) Reverse	20.67	1.129	0.736	17.18
(E-FTO) Forward	21.70	1.022	0.699	15.51
(E-FTO) Reverse	21.86	1.103	0.752	18.15

η: power conversion efficiency.

4. Conclusion

Process- and structure-simplified PSCs were fabricated to enhance the economical issues related commercialization, and successfully yielded a remarkable efficiency comparable with conventional PSCs. Atmospheric Ar/O_2 plasma was introduced to superfast form the HBL of PSCs under the authentic LT condition, and the electrical quality was systemically evaluated. Moreover, the fabrication process was further simplified through entirely removing the HBL in planar PSCs, and the efficiency deterioration caused by the absence of HBL was recovered through increasing grain size of perovskite and modifying the surface morphology of FTO. The subtopics are concluded in the viewpoint of each subtopic as follows:

1. Atmospheric Ar/O_2 plasma energy was exploited for the formulation of SnO_2 HBLs instead of conventional thermal-energy, to realize ultra-fast HBL fabrication within 5 min. This PA approach generated a dense oxide lattice compared with thermally-oxidized TFs, resulting in excellent electrical conductivity with lower trap density. As a result, the PV performance was enhanced from 17.46 to 18.64 % (a champion PCE

of 19.58 %) when introducing the plasma-derived SnO_2 HBLs into the PSCs due to effective electron extraction and mitigated non-radiative recombination at the P-SnO_2 HBL/perovskite interface. In addition, the extent of charge carrier accumulation at the SnO_2/perovskite interface was reduced in the plasma approach, which relaxed the hysteresis and improved the resistance to sunlight of PSCs.

2. A simple and efficient PSC was fabricated in spite of eliminating a HBL. The $MAPbI_3$ film was directly deposited on a blank FTO glass, and it was demonstrated that the formation of large grain and thick film were material to outstanding performance of the HBL-free PSCs. The grain size of $MAPbI_3$ grew up to *ca.* 1 μm by using 58 wt% stock solution while maintaining the high crystallinity. A large grain based- $MAPbI_3$ film hindered HTM permeation effectively, enabling a reduction in exciton recombination. Accordingly, the top-performing HBL-free PSC had a PCE of 18.20 %. Furthermore, the HBL-free PSCs had strong resistance to sunlight or moisture compared with the TiO_2 HBL-inserted type. In case of recyclability, the performance of TiO_2 HBL-inserted cell was dramatically reduced after just one recycle, whereas, the HBL-free cell maintained the original performance after four recycles.

Consequently, these highly simple, robust and efficient HBL-free PSCs are very suitable to a commercial solar cell model in terms of economic and environmental values.

3. A hierachically porous FTO was fabricated *via* ECEP and applied it to the HBL-free PSC as a transparent electrode. The effect of FTO surface engineering on the PV performance was systemically estimated, which demonstrated that free electrons were more quickly injected from perovskite to E-FTO than to P-FTO due to the large interfacial area of the perovskite/E-FTO interface. The quick extraction behavior is analogous with the process occurring in the MPL of MS-PSCs. Concurrently, the performance was also enhanced *via* increased light-capturing achieved by the scattering effect and tight interfacial contact obtained through better surface wettability. Employing the E-FTO resulted in higher J_{sc} and PCE than those of the P-FTO-based HBL-free PSC. Serious hysteresis, which is not readily resolved for P-FTO-based HBL-free PSCs, was alleviated by harmonizing the unbalanced electron and hole flux *via* enlarging the perovskite/FTO interfacial area. Therefore, the best PCE of 19.22 % was recorded for E-FTO-based HBL-free PSCs, the highest efficiency among this type of PSC. Finally, our

simplified PSC design has good commercialization potential arising from its good reproducibility, recyclability, long-term stability, and lower production cost.

References

[1] K. Yoshikawa, H. Kawasaki, W. Yoshida, T. Irie, K. Konishi, K. Nakano, T. Uto, D. Adachi, M. Kanematsu, H. Uzu, K. Yamamoto, *Nat. Energy*, **2017**, 2, 17032.

[2] A. Chirilă, S. Buecheler, F. Pianezzi, P. Bloesch, C. Gretener, A. R. Uhl, C. Fella, L. Kranz, J. Perrenoud, S. Seyrling, R. Verma, S. Nishiwaki, Y. E. Romanyuk, G. Bilger, A. N. Tiwari, *Nat. Mater.*, **2011**, 10, 857.

[3] T. Kim, J.-H. Kim, T. E. Kang, C. Lee, H. Kang, M. Shin, C. Wang, B. Ma, U. Jeong, T.-S. Kim, B. J. Kim, *Nat. Commun.*, **2015**, 6, 8547.

[4] B. O'Regan, M. Grätzel, *Nature*, **1991**, 353, 737.

[5] A. Kojima, K. Teshima, Y. Shirai, T. Miyasaka, *J. Am. Chem. Soc.*, **2009**, 131, 6050.

[6] M. A. Green, A. Ho-Baillie, H. J. Snaith, *Nat. Photon.*, **2014**, 8, 506.

[7] G. E. Eperon, S. D. Stranks, C. Menelaou, M. B. Johnston, L. M. Herz, H. J. Snaith, *Energy Environ. Sci.*, **2014**, 7, 982.

[8] G. Kakavelakis, T. Maksudov, D. Konios, I. Paradisanos, G. Kioseoglou, E. Stratakis, E. Kymakis, *Adv. Energy Mater.*, **2016**, n/a.

[9] S. D. Stranks, G. E. Eperon, G. Grancini, C. Menelaou, M. J. P. Alcocer, T. Leijtens, L. M. Herz, A. Petrozza, H. J. Snaith, *Science*, **2013**, 342, 341.

[10] C. R. Kagan, D. B. Mitzi, C. D. Dimitrakopoulos, *Science*, **1999**, 286, 945.

[11] K. T. Cho, S. Paek, G. Grancini, C. Roldan-Carmona, P. Gao, Y. Lee, M. K. Nazeeruddin, *Energy Environ. Sci.*, **2017**, 10, 621.

[12] N. J. Jeon, J. H. Noh, W. S. Yang, Y. C. Kim, S. Ryu, J. Seo, S. I. Seok, *Nature*, **2015**, 517, 476.

[13] D. P. McMeekin, G. Sadoughi, W. Rehman, G. E. Eperon, M. Saliba,

M. T. Hörantner, A. Haghighirad, N. Sakai, L. Korte, B. Rech, M. B. Johnston, L. M. Herz, H. J. Snaith, *Science*, **2016**, 351, 151.
[14] H. Chen, F. Ye, W. Tang, J. He, M. Yin, Y. Wang, F. Xie, E. Bi, X. Yang, M. Grätzel, L. Han, *Nature*, **2017**, 550, 92.
[15] M. Yang, Z. Li, M. O. Reese, O. G. Reid, D. H. Kim, S. Siol, T. R. Klein, Y. Yan, J. J. Berry, M. F. A. M. van Hest, K. Zhu, *Nat. Energy*, **2017**, 2, 17038.
[16] G. Abdelmageed, H. R. Sully, S. Bonabi Naghadeh, A. El-Hag Ali, S. A. Carter, J. Z. Zhang, *ACS Appl. Energy Mater.*, **2018**, 1, 387.
[17] S. S. Shin, E. J. Yeom, W. S. Yang, S. Hur, M. G. Kim, J. Im, J. Seo, J. H. Noh, S. I. Seok, *Science*, **2017**, 356, 167.
[18] I. Mesquita, L. Andrade, A. Mendes, *Renew. Sust. Energ. Rev.*, **2018**, 82, 2471.
[19] M. Saliba, T. Matsui, J.-Y. Seo, K. Domanski, J.-P. Correa-Baena, M. K. Nazeeruddin, S. M. Zakeeruddin, W. Tress, A. Abate, A. Hagfeldt, M. Grätzel, *Energy Environ. Sci.*, **2016**, 9, 1989.
[20] S. Agarwala, M. Kevin, A. S. W. Wong, C. K. N. Peh, V. Thavasi, G. W. Ho, *ACS Appl. Mater. Interfaces*, **2010**, 2, 1844.
[21] J. M. Ball, M. M. Lee, A. Hey, H. J. Snaith, *Energy Environ. Sci.*, **2013**, 6, 1739.
[22] H. Zhou, Q. Chen, G. Li, S. Luo, T.-b. Song, H.-S. Duan, Z. Hong, J. You, Y. Liu, Y. Yang, *Science*, **2014**, 345, 542.
[23] J. P. Correa Baena, L. Steier, W. Tress, M. Saliba, S. Neutzner, T. Matsui, F. Giordano, T. J. Jacobsson, A. R. Srimath Kandada, S. M. Zakeeruddin, A. Petrozza, A. Abate, M. K. Nazeeruddin, M. Grätzel, A. Hagfeldt, *Energy Environ. Sci.*, **2015**, 8, 2928.
[24] J. Wang, M. Qin, H. Tao, W. Ke, Z. Chen, J. Wan, P. Qin, L. Xiong, H. Lei, H. Yu, G. Fang, *Appl. Phys. Lett.*, **2015**, 106, 121104.
[25] L. Zuo, Z. Gu, T. Ye, W. Fu, G. Wu, H. Li, H. Chen, *J. Am. Chem. Soc.*, **2015**, 137, 2674.

[26] Z. Liu, B. Sun, X. Liu, J. Han, H. Ye, Y. Tu, C. Chen, T. Shi, Z. Tang, G. Liao, *J. Mater. Chem. A*, **2018**, 6, 7409.
[27] Y. Chen, L. Zhang, Y. Zhang, H. Gao, H. Yan, *RSC Adv.*, **2018**, 8, 10489.
[28] W. Ke, D. Zhao, A. J. Cimaroli, C. R. Grice, P. Qin, Q. Liu, L. Xiong, Y. Yan, G. Fang, *J. Mater. Chem. A*, **2015**, 3, 24163.
[29] W. Ke, G. Fang, Q. Liu, L. Xiong, P. Qin, H. Tao, J. Wang, H. Lei, B. Li, J. Wan, G. Yang, Y. Yan, *J. Am. Chem. Soc.*, **2015**, 137, 6730.
[30] Q. Jiang, L. Zhang, H. Wang, X. Yang, J. Meng, H. Liu, Z. Yin, J. Wu, X. Zhang, J. You, *Nat. Energy*, **2016**, 2, 16177.
[31] S. Jeong, S. Seo, H. Park, H. Shin, *Chem. Commun.*, **2019**, 55, 2433.
[32] K.-H. Jung, J.-Y. Seo, S. Lee, H. Shin, N.-G. Park, *J. Mater. Chem. A*, **2017**, 5, 24790.
[33] M. F. Mohamad Noh, N. A. Arzaee, J. Safaei, N. A. Mohamed, H. P. Kim, A. R. Mohd Yusoff, J. Jang, M. A. Mat Teridi, *J. Alloys Comp.*, **2019**, 773, 997.
[34] J. Barbé, M. L. Tietze, M. Neophytou, B. Murali, E. Alarousu, A. E. Labban, M. Abulikemu, W. Yue, O. F. Mohammed, I. McCulloch, A. Amassian, S. Del Gobbo, *ACS Appl. Mater. Interfaces*, **2017**, 9, 11828.
[35] M. Abulikemu, M. Neophytou, J. M. Barbé, M. L. Tietze, A. El Labban, D. H. Anjum, A. Amassian, I. McCulloch, S. Del Gobbo, *J. Mater. Chem. A*, **2017**, 5, 7759.
[36] L. Huang, X. Sun, C. Li, J. Xu, R. Xu, Y. Du, J. Ni, H. Cai, J. Li, Z. Hu, J. Zhang, *ACS Appl. Mater. Interfaces*, **2017**, 9, 21909.
[37] Y. Li, O. R. Musaev, J. M. Wrobel, M. B. Kruger, *Appl. Phys. A*, **2018**, 124, 499.
[38] M. Zhu, W. Liu, W. Ke, S. Clark, E. B. Secor, T.-B. Song, M. G. Kanatzidis, X. Li, M. C. Hersam, *J. Mater. Chem. A*, **2017**, 5, 24110.
[39] D. A. Hook, J. A. Olhausen, J. Krim, M. T. Dugger, *J. Microelectromech. Syst.*, **2010**, 19, 1292.

[40] J. Johnson, R. Robinson, D. Allred, R. Sandberg, R. S. Turley, K. Adamson, A. Jackson, *Soc. Vac. Coater,* **2004**, 368.
[41] Y. Hashimoto, M. Hamagaki, *Elect. Eng. JPN.*, **2006**, 154, 1.
[42] Y. S. Park, E. Kim, B. Hong, J. Lee, *Mater. Res. Bull.*, **2013**, 48, 5115.
[43] Y. Nishihara, M. Chikamatsu, S. Kazaoui, T. Miyadera, Y. Yoshida, *JPN. J. Appl. Phys.*, **2018**, 57, 04FS07.
[44] J. Singh Meena, M.-C. Chu, S.-W. Kuo, F.-C. Chang, F.-H. Ko, *Phys. Chem. Chem. Phys.*, **2010**, 12, 2582.
[45] M. Maeng, J.-H. Kim, J.-A. Hong, Y. Park, *J. Kor. Phys. Soc.*, **2016**, 68, 692.
[46] T. Berthold, J. Rombach, T. Stauden, V. Polyakov, V. Cimalla, S. Krischok, O. Bierwagen, M. Himmerlich, *J. Appl. Phys.*, **2016**, 120, 245301.
[47] D. Mariotti, *Appl. Phys. Lett.*, **2008**, 92, 151505.
[48] Z. Strýhal, Pavlı, x, J. k, S. Novák, A. Macková, V. Peřina, K. Veltruská, *Vacuum*, **2002**, 67, 665.
[49] D.-K. Kim, M.-H. Cho, *Appl. Sci. Converg. Tech.,* **2017**, 26, 133.
[50] J. A. Baier-Saip, J. I. Avila, G. Tarrach, A. L. Cabrera, V. Fuenzalida, R. A. Zarate, I. K. Schuller, *Surf. Coat. Tech.*, **2005**, 195, 168.
[51] J.-S. Lee, S.-M. Song, Y.-H. Kim, J.-Y. Kwon, M.-K. Han, *Phys. Status Solidi A.* **2013**, 210, 1745.
[52] Y. Xue, H. He, Y. Jin, B. Lu, H. Cao, J. Jiang, S. Bai, Z. Ye, *Appl. Phys. A*, **2014**, 114, 509.
[53] Y. Li, J. K. Cooper, W. Liu, C. M. Sutter-Fella, M. Amani, J. W. Beeman, A. Javey, J. W. Ager, Y. Liu, F. M. Toma, I. D. Sharp, *Nat. Commun.,* **2016**, 7, 12446.
[54] J. Zhou, X. Meng, X. Zhang, X. Tao, Z. Zhang, J. Hu, C. Wang, Y. Li, S. Yang, *Mater. Chem. Front.*, **2017**, 1, 802.
[55] K. Wang, Y. Shi, Q. Dong, Y. Li, S. Wang, X. Yu, M. Wu, T. Ma, *J.*

Phys. Chem. Lett., **2015**, 6, 755.
[56] S. Yoon, S. J. Kim, H. S. Kim, J.-S. Park, I. K. Han, J. W. Jung, M. Park, *Nanoscale*, **2017**, 9, 16305.
[57] S. L. Fernandes, A. C. Véron, N. F. A. Neto, F. A. Nüesch, J. H. Dias da Silva, M. A. Zaghete, C. F. d. O. Graeff, *Mater. Lett.*, **2016**, 181, 103.
[58] S. S. Shin, W. S. Yang, J. H. Noh, J. H. Suk, N. J. Jeon, J. H. Park, J. S. Kim, W. M. Seong, S. I. Seok, *Nat. Commun.*, **2015**, 6, 7410.
[59] Y. Okamoto, Y. Suzuki, *J. Phys. Chem. C*, **2016**, 120, 13995.
[60] S. Gubbala, V. Chakrapani, V. Kumar, M. K. Sunkara, *Adv. Funct. Mater.*, **2008**, 18, 2411.
[61] T. Leijtens, G. E. Eperon, S. Pathak, A. Abate, M. M. Lee, H. J. Snaith, *Nat. Commun.*, **2013**, 4, 2885.
[62] N. Ahn, K. Kwak, M. S. Jang, H. Yoon, B. Y. Lee, J.-K. Lee, P. V. Pikhitsa, J. Byun, M. Choi, *Nat. Commun.*, **2016**, 7, 13422.
[63] D. Liu, T. L. Kelly, *Nat. Photon.*, **2013**, 8, 133.
[64] Q. Zhang, C. S. Dandeneau, X. Zhou, G. Cao, *Adv. Mater.*, **2009**, 21, 4087.
[65] Y. Cheng, Q.-D. Yang, J. Xiao, Q. Xue, H.-W. Li, Z. Guan, H.-L. Yip, S.-W. Tsang, *ACS Appl. Mater. Interfaces*, **2015**, 7, 19986.
[66] P. Shen, M. Yao, G. Wang, R. Mi, W. Guo, Y. Bai, L. Shen, *J. Mater. Chem. A*, **2018**, 6, 17401.
[67] H. J. Snaith, C. Ducati, *Nano Lett.*, **2010**, 10, 1259.
[68] H. Lei, G. Yang, Y. Guo, L. Xiong, P. Qin, X. Dai, X. Zheng, W. Ke, H. Tao, Z. Chen, B. Li, G. Fang, *Phys. Chem. Chem. Phys.*, **2016**, 18, 16436.
[69] A. J. Nozik, R. Memming, *J. Phys. Chem.*, **1996**, 100, 13061.
[70] Q. Jiang, X. Zhang, J. You, *Small*, **2018**, 14, 1801154.
[71] B. Roose, J.-P. C. Baena, K. C. Gödel, M. Graetzel, A. Hagfeldt, U. Steiner, A. Abate, *Nano Energy*, **2016**, 30, 517.
[72] Y. Li, J. Zhu, Y. Huang, F. Liu, M. Lv, S. Chen, L. Hu, J. Tang, J.

Yao, S. Dai, *RSC Adv.*, **2015**, 5, 28424.
[73] Z. H. Bakr, Q. Wali, A. Fakharuddin, L. Schmidt-Mende, T. M. Brown, R. Jose, *Nano Energy*, **2017**, 34, 271.
[74] J. Song, E. Zheng, J. Bian, X.-F. Wang, W. Tian, Y. Sanehira, T. Miyasaka, *J. Mater. Chem. A*, **2015**, 3, 10837.
[75] M. M. Lee, J. Teuscher, T. Miyasaka, T. N. Murakami, H. J. Snaith, *Science*, **2012**, 338, 643.
[76] D. Liu, J. Yang, T. L. Kelly, *J. Am. Chem. Soc.*, **2014**, 136, 17116.
[77] W. A. Laban, L. Etgar, *Energy Environ. Sci.*, **2013**, 6, 3249.
[78] S. Aharon, S. Gamliel, B. E. Cohen, L. Etgar, *Phys. Chem. Chem. Phys.*, **2014**, 16, 10512.
[79] Z. Zhao, W. Sun, Y. Li, S. Ye, H. Rao, F. Gu, Z. Liu, Z. Bian, C. Huang, *J. Mater. Chem. A*, **2017**, 5, 4756.
[80] L. Huang, X. Sun, C. Li, R. Xu, J. Xu, Y. Du, Y. Wu, J. Ni, H. Cai, J. Li, Z. Hu, J. Zhang, *Sol. Energy Mater. Sol. Cells*, **2016**, 157, 1038.
[81] D. Yang, X. Zhou, R. Yang, Z. Yang, W. Yu, X. Wang, C. Li, S. Liu, R. P. H. Chang, *Energy Environ. Sci.*, **2016**, 9, 3071.
[82] M. Liu, M. B. Johnston, H. J. Snaith, *Nature*, **2013**, 501, 395.
[83] N. J. Jeon, J. H. Noh, Y. C. Kim, W. S. Yang, S. Ryu, S. I. Seok, *Nat. Mater.*, **2014**, 13, 897.
[84] N. Ahn, D.-Y. Son, I.-H. Jang, S. M. Kang, M. Choi, N.-G. Park, *J. Am. Chem. Soc.*, **2015**, 137, 8696.
[85] J.-W. Lee, Z. Dai, C. Lee, H. M. Lee, T.-H. Han, N. De Marco, O. Lin, C. S. Choi, B. Dunn, J. Koh, D. Di Carlo, J. H. Ko, H. D. Maynard, Y. Yang, *J. Am. Chem. Soc.*, **2018**, 140, 6317.
[86] W. Nie, H. Tsai, R. Asadpour, J.-C. Blancon, A. J. Neukirch, G. Gupta, J. J. Crochet, M. Chhowalla, S. Tretiak, M. A. Alam, H.-L. Wang, A. D. Mohite, *Science*, **2015**, 347, 522.
[87] D. Bi, C. Yi, J. Luo, J.-D. Décoppet, F. Zhang, Shaik M. Zakeeruddin, X. Li, A. Hagfeldt, M. Grätzel, *Nat. Energy*, **2016**, 1, 16142.

[88] W. Li, J. Fan, J. Li, Y. Mai, L. Wang, *J. Am. Chem. Soc.*, **2015**, 137, 10399.
[89] C. Bi, Q. Wang, Y. Shao, Y. Yuan, Z. Xiao, J. Huang, *Nat. Commun.*, **2015**, 6, 7747.
[90] Q. Dong, Y. Yuan, Y. Shao, Y. Fang, Q. Wang, J. Huang, *Energy Environ. Sci.*, **2015**, 8, 2464.
[91] Y. Yu, C. Wang, C. R. Grice, N. Shrestha, D. Zhao, W. Liao, L. Guan, R. A. Awni, W. Meng, A. J. Cimaroli, K. Zhu, R. J. Ellingson, Y. Yan, *ACS Energy Lett.,* **2017**, 2, 1177.
[92] C. Fei, B. Li, R. Zhang, H. Fu, J. Tian, G. Cao, *Adv. Energy Mater.*, **2017**, 7, 1602017.
[93] L. Zuo, H. Guo, D. W. deQuilettes, S. Jariwala, N. De Marco, S. Dong, R. DeBlock, D. S. Ginger, B. Dunn, M. Wang, Y. Yang, *Sci. Adv.*, **2017**, 3.
[94] L. Zuo, S. Dong, N. De Marco, Y.-T. Hsieh, S.-H. Bae, P. Sun, Y. Yang, *J. Am. Chem. Soc.*, **2016**, 138, 15710.
[95] S. Sanchez, X. Hua, N. Phung, U. Steiner, A. Abate, *Adv. Energy Mater.*, **2018**, 8, 1702915.
[96] C.-C. Zhang, Z.-K. Wang, M. Li, Z.-Y. Liu, J.-E. Yang, Y.-G. Yang, X.-Y. Gao, H. Ma, *J. Mater. Chem. A*, **2018**, 6, 1161.
[97] Q. Cao, S. Yang, Q. Gao, L. Lei, Y. Yu, J. Shao, Y. Liu, *ACS Appl. Mater. Interfaces*, **2016**, 8, 7854.
[98] M. Yang, T. Zhang, P. Schulz, Z. Li, G. Li, D. H. Kim, N. Guo, J. J. Berry, K. Zhu, Y. Zhao, *Nat. Commun.*, **2016**, 7, 12305.
[99] Z. Xiao, Q. Dong, C. Bi, Y. Shao, Y. Yuan, J. Huang, *Adv. Mater.*, **2014**, 26, 6503.
[100] S. M. Jain, Z. Qiu, L. Häggman, M. Mirmohades, M. B. Johansson, T. Edvinsson, G. Boschloo, *Energy Environ. Sci.*, **2016**, 9, 3770.
[101] T. S. Sherkar, C. Momblona, L. Gil-Escrig, J. Ávila, M. Sessolo, H. J. Bolink, L. J. A. Koster, *ACS Energy Lett.*, **2017**, 2, 1214.

[102] J.-W. Lee, S.-H. Bae, N. De Marco, Y.-T. Hsieh, Z. Dai, Y. Yang, *Mater. Today Energy*, **2018**, 7, 149.
[103] C. Tao, S. Neutzner, L. Colella, S. Marras, A. R. Srimath Kandada, M. Gandini, M. D. Bastiani, G. Pace, L. Manna, M. Caironi, C. Bertarelli, A. Petrozza, *Energy Environ. Sci.,* **2015**, 8, 2365.
[104] W. Ke, G. Fang, J. Wan, H. Tao, Q. Liu, L. Xiong, P. Qin, J. Wang, H. Lei, G. Yang, M. Qin, X. Zhao, Y. Yan, *Nat. Commun.*, **2015**, 6, 6700.
[105] Q. Hu, J. Wu, C. Jiang, T. Liu, X. Que, R. Zhu, Q. Gong, *ACS Nano*, **2014**, 8, 10161.
[106] P. Zhao, M. Han, W. Yin, X. Zhao, S. G. Kim, Y. Yan, M. Kim, Y. J. Song, N. G. Park, H. S. Jung, *ACS Appl. Mater. Interfaces*, **2018**, 10, 10132.
[107] A. Listorti, E. J. Juarez-Perez, C. Frontera, V. Roiati, L. Garcia-Andrade, S. Colella, A. Rizzo, P. Ortiz, I. Mora-Sero, *J. Phys. Chem. Lett.*, **2015**, 6, 1628.
[108] Y. Yu, J. Li, D. Geng, J. Wang, L. Zhang, T. L. Andrew, M. S. Arnold, X. Wang, *ACS Nano*, **2015**, 9, 564.
[109] D. Zhong, B. Cai, X. Wang, Z. Yang, Y. Xing, S. Miao, W.-H. Zhang, C. Li, *Nano Energy*, **2015**, 11, 409.
[110] X. Chen, N. Matsumoto, Y. Hu, G. S. Wilson, *Analyt. Chem.*, **2002**, 74, 368.
[111] J.-Y. Chen, C.-C. Chueh, Z. Zhu, W.-C. Chen, A. K. Y. Jen, *Sol. Energy Mater. Sol. Cells*, **2017**, 164, 47.
[112] O. Lupan, T. Pauporté, B. Viana, I. M. Tiginyanu, V. V. Ursaki, R. Cortès, *ACS Appl. Mater. Interfaces*, **2010**, 2, 2083.
[113] J.-W. Bae, B.-R. Koo, H.-R. An, H.-J. Ahn, *Ceramics Internat.*, **2015**, 41, 14668.
[114] K.-T. Lee, S.-Y. Lu, *J. Mater. Chem.*, **2012**, 22, 16259.
[115] J. H. Heo, H. J. Han, D. Kim, T. K. Ahn, S. H. Im, *Energy Environ. Sci.*, **2015**, 8, 1602.

[116] S. M. Ubnoske, Q. Peng, E. R. Meshot, C. B. Parker, J. T. Glass, *J. Phys. Chem. C*, **2015**, 119, 26119.
[117] O. K. Varghese, C. A. Grimes, *Sol. Energy Mater. Sol. Cells*, **2008**, 92, 374.
[118] Y. Lin, S. Zhou, X. Liu, S. Sheehan, D. Wang, *J. Am. Chem. Soc.*, **2009**, 131, 2772.
[119] M.-G. Kim, M. G. Kanatzidis, A. Facchetti, T. J. Marks, *Nat. Mater.*, **2011**, 10, 382.
[120] H. I. Yeom, J. B. Ko, G. Mun, S. H. K. Park, *J. Mater. Chem. C*, **2016**, 4, 6873.
[121] Y. Zhao, L. Duan, G. Dong, D. Zhang, J. Qiao, L. Wang, Y. Qiu, *Langmuir*, **2013**, 29, 151.
[122] J. You, L. Meng, T.-B. Song, T.-F. Guo, Y. Yang, W.-H. Chang, Z. Hong, H. Chen, H. Zhou, Q. Chen, Y. Liu, N. De Marco, Y. Yang, *Nat. Nanotechnol.*, **2016**, 11, 75.
[123] G. Huang, L. Duan, G. Dong, D. Zhang, Y. Qiu, *ACS Appl. Mater. Interfaces*, **2014**, 6, 20786.
[124] K. K. Banger, Y. Yamashita, K. Mori, R. L. Peterson, T. Leedham, J. Rickard, H. Sirringhaus, *Nat. Mater.*, **2011**, 10, 45.
[125] H. Tan, A. Jain, O. Voznyy, X. Lan, F. P. García de Arquer, J. Z. Fan, R. Quintero-Bermudez, M. Yuan, B. Zhang, Y. Zhao, F. Fan, P. Li, L. N. Quan, Y. Zhao, Z.-H. Lu, Z. Yang, S. Hoogland, E. H. Sargent, *Science*, **2017**, 355, 722.
[126] K. Wang, Y. Shi, B. Li, L. Zhao, W. Wang, X. Wang, X. Bai, S. Wang, C. Hao, T. Ma, *Adv. Mater.*, **2016**, 28, 1891.
[127] S. Mori, K. Sunahara, Y. Fukai, T. Kanzaki, Y. Wada, S. Yanagida, *J. Phys. Chem. C*, **2008**, 112, 20505.
[128] K. Basu, D. Benetti, H. Zhao, L. Jin, F. Vetrone, A. Vomiero, F. Rosei, *Sci. Rep.*, **2016**, 6, 23312.
[129] F. Hao, C. C. Stoumpos, R. P. H. Chang, M. G. Kanatzidis, *J. Am.*

Chem. Soc., **2014**, 136, 8094.
[130] D. Liu, S. Li, P. Zhang, Y. Wang, R. Zhang, H. Sarvari, F. Wang, J. Wu, Z. Wang, Z. D. Chen, *Nano Energy*, **2017**, 31, 462.
[131] X. Ren, D. Yang, Z. Yang, J. Feng, X. Zhu, J. Niu, Y. Liu, W. Zhao, S. F. Liu, *ACS Appl. Mater. Interfaces*, **2017**, 9, 2421.
[132] J. Xu, A. Buin, A. H. Ip, W. Li, O. Voznyy, R. Comin, M. Yuan, S. Jeon, Z. Ning, J. J. McDowell, P. Kanjanaboos, J.-P. Sun, X. Lan, L. N. Quan, D. H. Kim, I. G. Hill, P. Maksymovych, E. H. Sargent, *Nat. Commun.*, **2015**, 6, 7081.
[133] C. Fei, B. Li, R. Zhang, H. Fu, J. Tian, G. Cao, *Adv. Energy Mater.*, **2017**, 7, 1602017.
[134] M. M. Byranvand, T. Kim, S. Song, G. Kang, S. U. Ryu, T. Park, *Adv. Energy Mater.* **2018***,* 8, 1702235.
[135] D. Yang, R. Yang, J. Zhang, Z. Yang, S. Liu, C. Li, *Energy Environ. Sci.*, **2015**, 8, 3208.
[136] Q. Luo, H. Chen, Y. Lin, H. Du, Q. Hou, F. Hao, N. Wang, Z. Guo, J. Huang, *Adv. Funct. Mater.*, **2017**, 27, 1702090.
[137] Z. Zhu, J. Ma, Z. Wang, C. Mu, Z. Fan, L. Du, Y. Bai, L. Fan, H. Yan, D. L. Phillips, S. Yang, *J. Am. Chem. Soc.*, **2014**, 136, 3760.
[138] G. A. Sepalage, S. Meyer, A. Pascoe, A. D. Scully, F. Huang, U. Bach, Y.-B. Cheng, L. Spiccia, *Adv. Funct. Mater.*, **2015**, 25, 5650.
[139] Y. Yamada, T. Nakamura, M. Endo, A. Wakamiya, Y. Kanemitsu, *J. Am. Chem. Soc.*, **2014**, 136, 11610.
[140] J. Peng, Y. Wu, W. Ye, D. A. Jacobs, H. Shen, X. Fu, Y. Wan, T. Duong, N. Wu, C. Barugkin, H. T. Nguyen, D. Zhong, J. Li, T. Lu, Y. Liu, M. N. Lockrey, K. J. Weber, K. R. Catchpole, T. P. White, *Energy Environ. Sci.*, **2017**, 10, 1792.
[141] R. Gottesman, E. Haltzi, L. Gouda, S. Tirosh, Y. Bouhadana, A. Zaban, E. Mosconi, F. De Angelis, *J. Phys. Chem. Lett.*, **2014**, 5, 2662.
[142] N. Mohammadian, A. Moshaii, A. Alizadeh, S. Gharibzadeh, R.

Mohammadpour, *J. Phys. Chem. Lett.*, **2016**, 7, 4614.
[143] J. Peng, Y. Wu, W. Ye, D. A. Jacobs, H. Shen, X. Fu, Y. Wan, T. Duong, N. Wu, C. Barugkin, H. T. Nguyen, D. Zhong, J. Li, T. Lu, Y. Liu, M. N. Lockrey, K. J. Weber, K. R. Catchpole, T. P. White, *Energy Environ. Sci.*, **2017**, 10, 1792.
[144] N. Ahn, K. Kwak, M. S. Jang, H. Yoon, B. Y. Lee, J.-K. Lee, P. V. Pikhitsa, J. Byun, M. Choi, *Nat. Commun.*, **2016**, 7, 13422.
[145] M. R. Leyden, L. K. Ono, S. R. Raga, Y. Kato, S. Wang, Y. Qi, *J. Mater. Chem. A*, **2014**, 2, 18742.
[146] X. Xu, Q. Chen, Z. Hong, H. Zhou, Z. Liu, W.-H. Chang, P. Sun, H. Chen, N. D. Marco, M. Wang, Y. Yang, *Nano Lett.*, **2015**, 15, 6514.
[147] H. D. Kim, H. Ohkita, H. Benten, S. Ito, *Adv. Mater.*, **2016**, 28, 917.
[148] B.-E. Cohen, S. Aharon, A. Dymshits, L. Etgar, *J. Phys. Chem. C*, **2016**, 120, 142.
[149] Z. Liang, S. Zhang, X. Xu, N. Wang, J. Wang, X. Wang, Z. Bi, G. Xu, N. Yuan, J. Ding, *RSC Adv.*, **2015**, 5, 60562.
[150] W. Zhu, T. Yu, F. Li, C. Bao, H. Gao, Y. Yi, J. Yang, G. Fu, X. Zhou, Z. Zou, *Nanoscale*, **2015**, 7, 5427.
[151] S. Ryu, J. H. Noh, N. J. Jeon, Y. Chan Kim, W. S. Yang, J. Seo, S. I. Seok, *Energy Environ. Sci.*, **2014**, 7, 2614.
[152] D. Liu, M. K. Gangishetty, T. L. Kelly, *J. Mater. Chem. A*, **2014**, 2, 19873.
[153] W. Ke, G. Fang, J. Wan, H. Tao, Q. Liu, L. Xiong, P. Qin, J. Wang, H. Lei, G. Yang, M. Qin, X. Zhao, Y. Yan, *Nat. Commun.*, **2015**, 6.
[154] Y. Zhang, M. Liu, G. E. Eperon, T. C. Leijtens, D. McMeekin, M. Saliba, W. Zhang, M. de Bastiani, A. Petrozza, L. M. Herz, M. B. Johnston, H. Lin, H. J. Snaith, *Mater. Horiz.*, **2015**, 2, 315.
[155] Y. Li, J. Zhu, Y. Huang, J. Wei, F. Liu, Z. Shao, L. Hu, S. Chen, S. Yang, J. Tang, J. Yao, S. Dai, *Nanoscale*, **2015**, 7, 9902.
[156] Y. Li, W. Yan, Y. Li, S. Wang, W. Wang, Z. Bian, L. Xiao, Q. Gong,

Sci. Rep., **2015**, 5, 14485.
[157] P.-W. Liang, C.-Y. Liao, C.-C. Chueh, F. Zuo, S. T. Williams, X.-K. Xin, J. Lin, A. K.-Y. Jen, *Adv. Mater.*, **2014**, 26, 3748.
[158] G. Xing, N. Mathews, S. Sun, S. S. Lim, Y. M. Lam, M. Grätzel, S. Mhaisalkar, T. C. Sum, *Science*, **2013**, 342, 344.
[159] Q. Chen, H. Zhou, T.-B. Song, S. Luo, Z. Hong, H.-S. Duan, L. Dou, Y. Liu, Y. Yang, *Nano Lett.*, **2014**, 14, 4158.
[160] H. P. Dong, Y. Li, S. F. Wang, W. Z. Li, N. Li, X. D. Guo, L. D. Wang, *J. Mater. Chem. A*, **2015**, 3, 9999.
[161] J.-W. Lee, H.-S. Kim, N.-G. Park, *Acc. Chem. Res.*, **2016**, 49, 311.
[162] Z. Zhu, X. Zheng, Y. Bai, T. Zhang, Z. Wang, S. Xiao, S. Yang, *Phys. Chem. Chem. Phys.*, **2015**, 17, 18265.
[163] T. Leijtens, G. E. Eperon, S. Pathak, A. Abate, M. M. Lee, H. J. Snaith, *Nat. Commun.*, **2013**, 4, 2885.
[164] H.-S. Kim, I.-H. Jang, N. Ahn, M. Choi, A. Guerrero, J. Bisquert, N.-G. Park, *J. Phys. Chem. Lett.*, **2015**, 6, 4633.
[165] B. Roose, S. Pathak, U. Steiner, *Chem. Soc. Rev.*, **2015**, 44, 8326.
[166] B. J. Kim, D. H. Kim, S. L. Kwon, S. Y. Park, Z. Li, K. Zhu, H. S. Jung, *Nat. Commun.*, **2016**, 7, 11735.
[167] S. Wu, S. Yuan, L. Shi, Y. Zhao, J. Fang, *J. Colloid Interf. Sci.*, **2010**, 346, 12.
[168] J. Yun, S. H. Hwang, J. Jang, *ACS Appl. Mater. Interfaces*, **2015**, 7, 2055.
[169] J. Ryu, J. Yun, J. Lee, K. Lee, J. Jang, *Chem. Commun.*, **2016**, 52, 2165.
[170] J. H. Heo, D. H. Song, H. J. Han, S. Y. Kim, J. H. Kim, D. Kim, H. W. Shin, T. K. Ahn, C. Wolf, T.-W. Lee, S. H. Im, *Adv. Mater.*, **2015**, 27, 3424.
[171] J. Xiao, J. Shi, H. Liu, Y. Xu, S. Lv, Y. Luo, D. Li, Q. Meng, Y. Li, *Adv. Energy Mater.*, **2015**, 5, 1401943.

[172] S. H. Hwang, H. Song, J. Lee, J. Jang, *Chem. Eur. J.*, **2014**, 20, 12974.
[173] Y. Li, S. Ye, W. Sun, W. Yan, Y. Li, Z. Bian, Z. Liu, S. Wang, C. Huang, *J. Mater. Chem. A*, **2015**, 3, 18389.
[174] P.-W. Liang, C.-Y. Liao, C.-C. Chueh, F. Zuo, S. T. Williams, X.-K. Xin, J. Lin, A. K. Y. Jen, *Adv. Mater.*, **2014**, 26, 3748.
[175] C. Sun, Z. Wu, H.-L. Yip, H. Zhang, X.-F. Jiang, Q. Xue, Z. Hu, Z. Hu, Y. Shen, M. Wang, F. Huang, Y. Cao, *Adv. Energy Mater.*, **2016**, 6, 1501534.
[176] J. You, Z. Hong, Y. Yang, Q. Chen, M. Cai, T.-B. Song, C.-C. Chen, S. Lu, Y. Liu, H. Zhou, Y. Yang, *ACS Nano*, **2014**, 8, 1674.
[177] Q. Xue, G. Chen, M. Liu, J. Xiao, Z. Chen, Z. Hu, X.-F. Jiang, B. Zhang, F. Huang, W. Yang, H.-L. Yip, Y. Cao, *Adv. Energy Mater.*, **2016**, 6, 1502021.
[178] M. H. U. Bhuiyan, R. Saidur, M. A. Amalina, R. M. Mostafizur, A. Islam, *Procedia Eng.*, **2015**, 105, 431.
[179] Z. Abbas, C. Labbez, S. Nordholm, E. Ahlberg, *J. Phys. Chem. C*, **2008**, 112, 5715.
[180] M. A. Brown, N. Duyckaerts, A. B. Redondo, I. Jordan, F. Nolting, A. Kleibert, M. Ammann, H. J. Wörner, J. A. van Bokhoven, Z. Abbas, *Langmuir*, **2013**, 29, 5023.
[181] W. Li, H. Dong, X. Guo, N. Li, J. Li, G. Niu, L. Wang, *J. Mater. Chem. A*, **2014**, 2, 20105.
[182] Y. Tu, J. Wu, M. Zheng, J. Huo, P. Zhou, Z. Lan, J. Lin, M. Huang, *Nanoscale*, **2015**, 7, 20539.
[183] B. Wu, K. Fu, N. Yantara, G. Xing, S. Sun, T. C. Sum, N. Mathews, *Adv. Energy Mater.*, **2015**, 5, 1500829.
[184] H. Tsai, W. Nie, J.-C. Blancon, C. C. Stoumpos, R. Asadpour, B. Harutyunyan, A. J. Neukirch, R. Verduzco, J. J. Crochet, S. Tretiak, L. Pedesseau, J. Even, M. A. Alam, G. Gupta, J. Lou, P. M. Ajayan, M. J.

Bedzyk, M. G. Kanatzidis, A. D. Mohite, *Nature*, **2016**, 536, 312.
[185] W. Nie, J.-C. Blancon, A. J. Neukirch, K. Appavoo, H. Tsai, M. Chhowalla, M. A. Alam, M. Y. Sfeir, C. Katan, J. Even, S. Tretiak, J. J. Crochet, G. Gupta, A. D. Mohite, *Nat. Commun.*, **2016**, 7, 11574.
[186] S.-W. Lee, S. Kim, S. Bae, K. Cho, T. Chung, L. E. Mundt, S. Lee, S. Park, H. Park, M. C. Schubert, S. W. Glunz, Y. Ko, Y. Jun, Y. Kang, H.-S. Lee, D. Kim, *Sci. Rep.*, **2016**, 6, 38150.

국문초록

페로브스카이트 태양전지는 유-무기 혼성 페로브스카이트 자체의 출중한 광-물리적 성질 때문에 태양 전지 분야에서 엄청난 관심을 받고 있다. 현재 페로브스카이트 태양전지의 연구 동향은 효율 향상뿐만 아니라, 대면적 코팅 기술, 장기 안정성을 위한 봉지화, 독성 평가 등 페로브스카이트 태양전지의 상업화를 이룩하기 위한 실용성 있는 주제로 옮겨 가고 있다. 그러나 단가, 생산성 그리고 재현성에 직접적으로 영향을 미치는 제조 공정 및 구조 개선 연구에 대한 관심은 상대적으로 부족하다. 그러므로 제작 효율 향상과 동시에 고성능을 확보할 수 있는 공정 및 구조 엔지니어링이 요구된다.

평면형 페로브스카이트 태양전지는 N 형 금속 산화물 기반의 정공 차단 층을 필수적으로 포함하며, 산화 방식에 따라 광학 및 전기적 성질이 크게 변화한다. 일반적으로 정공 차단 층 제조를 위해서 섭씨 500 ℃ 이상의 고온 공정과 1 - 3 시간 가량의 긴 어닝링 시간이 요구되는데, 이는 단가 절감 및 대량 생산에 부적합하다. 그러므로 이러한 시간 및 에너지

소모적인 공정을 대체할 수 있는 경제적인 공정을 고안할 필요가 있다. 대안 공정을 찾는 것뿐만 아니라, 저온 및 고속 제작 공정을 위해 정공 차단 층을 완전히 제거하는 것도 한가지 방법이 될 수 있다. 이러한 접근 방식은 정공 차단 층 제조에 필요한 사전 준비 과정 및 산화에 필요한 에너지 모두 생략할 수 있으므로, 제작 비용 절감, 생산성 및 재현성을 향상시킬 수 있는 장점이 있다. 그러나 정공 차단 층의 부재로 인해 전자 전달 속도가 저하되고, 정공 전달 물질과 투명 전극 간 접촉 가능성이 높아져 디바이스의 효율 감소 및 심각한 히스테레시스 현상이 발생하는 단점이 있다.

본 논문에서는 평면형 페로브스카이트 태양전지 제조 공정이나 구조를 단순화 시키는 것을 통해 공정 편의성을 증진시키고, 효율 및 장기 안정성이 확보된 고성능의 평면형 페로브스카이트 태양전지를 제조하는 방법을 제시한다. 자세하게는, 정공 차단 층 제조에 전통적으로 사용되던 에너지 소모적인 열-어닐링 공정을 플라즈마 공정으로 대체하거나, 혹은 정공 차단 층을 완전히 제거하여 구조를 단순시킨 후 최적화 과정을 통해 효율을 극대화하는 것이다. 첫 번째로, 상압 아르곤/산소 플라스마 에너지를 이용하여 상온에 가까운 저온조건에서 5분 이내의 고속으로 이산화주석

박막을 제조하였고, 이를 평면형 페로브스카이트 태양전지의 정공 차단 층으로 도입하였다. 플라스마를 통해 제작된 이산화주석 정공 차단 층은 결함 밀도가 낮고 전하 이동도가 높아 뛰어난 전기 전도성을 나타내었고, 나아가 태양전지의 효율을 향상시킬 수 있었다. 두 번째로, 제작 공정 및 구조를 더욱더 간소화하기 위하여 정공 차단 층을 완전히 제거하였고, 이러한 정공 차단 층이 제거된 페로브스카이트 태양전지의 성능을 극대화시키기 위하여 페로브스카이트 결정 크기와 두께를 조절 하였다. 본 구조에서는 페로브스카이트가 정공 전달 물질의 침투를 차단하는 정공 차단 층 역할을 하는데, 페로브스카이트 결정의 크기 및 필름의 두께가 커질수록 정공 차단 능력 및 효율이 향상되는 것을 관찰할 수 있었다. 셋째로, 상업용 FTO 의 표면을 전기화학적으로 식각하여 기공 크기가 다양한 다공성 FTO 를 제조하였고, 이를 정공 차단 층이 제거된 페로브스카이트의 투명 전극으로 도입하였다. 이러한 표면 변형은 투명전극과 페로브스카이트 간의 전하 이동 속도를 향상시켰고, 이는 태양전지의 전류 밀도 향상 및 히스테레시스 개선에 기여하였다. 뿐만 아니라 정공 차단 층이 제거된 페로브스카이트 태양전지는 정공 차단 층에 의해 유도되는 페로브스카이트 분해로부터 자유롭기

때문에 뛰어난 광안정성을 나타낸다. 따라서, 본 논문은 평면형 페로브스카이트 태양전지의 제조 편의성과 생산성, 경제성을 증대시키는 것뿐만 아니라 효율 및 안정성까지 향상시킬 수 있는 공정 및 구조 단순화 전략을 제시한다.

주요어: 페로브스카이트 태양전지, 공정 및 구조 단순화, 상압 산소/아르곤 플라즈마 산화법, 대형 페로브스카이트 결정, 다공성 투명 전극,

학 번: 2014-22595